To the Graduate Council:

I am submitting herewith a thesis written by Jonathan C. French entitled "Evaluation of a Hypothetical Source Method for Discretization of the Helmholtz Equation". I have examined the final copy of this thesis for form and content and recommend that it be accepted in partial fulfillment of the requirements for the degree of Master of Science, with a major in Mechanical Engineering.

John E. Caruthers

John E. Caruthers, Major Professor

We have read this thesis
and recommend its acceptance:

R. Engel

W C Reddy

Accepted for the Council:

Associate Vice Chancellor
and Dean of The Graduate School

STATEMENT OF PERMISSION TO USE

In presenting this thesis in partial fulfillment of the requirements for a Master's degree at The University of Tennessee, Knoxville, I agree that the Library shall make it available to borrowers under rules of the Library. Brief quotations from this thesis are allowable without special permission, provided that accurate acknowledgement of the source is made.

Permission for extensive quotation from or reproduction of this thesis may be granted by my major professor, or in his absence, by the Head of Interlibrary Services when, in the opinion of either, the proposed use of the material is for scholarly purposes. Any copying or use of the material in this thesis for financial gain shall not be allowed without my written permission.

Signature Jonathan Frund

Date 12/3/93

EVALUATION OF A HYPOTHETICAL SOURCE METHOD FOR DISCRETIZATION OF THE HELMHOLTZ EQUATION

A Thesis

Presented for the

Master of Science

Degree

The University of Tennessee, Knoxville

Jonathan C. French

December 1993

DEDICATION

This thesis is dedicated to
my wife Suzanne,
who makes life worth living,
and is blessing from God.

ACKNOWLEDGMENTS

I would like to thank my major professor,

Dr. John Caruthers,

for his conceptual support and encouragement;

and my parents,

Mr. Charles Tatem French

and

Mrs. Barbara Lorraine French

who have encouraged me in my pursuits.

ABSTRACT

This research examines the accuracy and benefits of a new discretization for linear field equations, with a particular focus on the Helmholtz equation. Instead of the typical Boundary Element Method (BEM) or integral methods, this technique uses local Green's functions to set up a block tri-diagonal system of equations. The Green's functions are computed with respect to local and hypothetical sources to generate an under-determined system of equations. Singular value decomposition (SVD) and pseudo-inversion is then applied to find the least-norm, least-squares local discretization. The local discretizations are then placed in a matrix along with appropriate boundary conditions to solve for the entire field implicitly. The results compare the new discretization with finite difference techniques, showing that the relative accuracy of the new discretization is several orders of magnitude better than the finite difference techniques for reduced frequency approaching the resonant frequency.

TABLE OF CONTENTS

CHAPTER 1. INTRODUCTION 1
1.1 Overview of the Current Study 1
1.2 Background 1

CHAPTER 2. DEVELOPMENT AND METHODOLOGY 4
2.1 Purpose 4
2.2 Discretization of the Field 6
2.3 Determine Appropriate Green's Function 11
2.4 Under-Constrained Field and Use of SVD 11
2.5 Nyquist Limit and Resonant Frequency 13

CHAPTER 3. NUMERICAL EXPERIMENTS, RESULTS AND HYPOTHESES . 17
3.1 Introduction 17
3.1.1 The Standard Case 19
3.1.2 Types of Plots 20
3.1.3 Limitations 23
3.2 Hypothetical Source Studies 27
3.2.1 Number of Hypothetical Sources 27
3.2.2 Distribution of Hypothetical Source Strengths 37
3.2.3 Hypothetical Source Radius 44
3.3 Pseudo-Inverse Calculation Study 48
3.3.1 Singular Value Truncation 48
3.3.2 Number of Singular Values 53
3.4 Robustness 66
3.4.1 One to Four Plane Waves 66
3.4.2 Monopoles and Evanescent Waves 70
3.4.3 Aspect Ratio 73
3.5 Comparison to Existing Methods 79
3.5.1 Comparison Using Single Computed Node Grid 79
3.6 2-D Boundary Value Test Problem 82
3.6.1 Problem Description and Boundary Conditions 82
3.6.2 Results 84

CHAPTER 5. CONCLUSIONS 95

CHAPTER 6. FURTHER WORK 98
6.1 Theoretical Study Options 98
6.2 Application Options 99

LIST OF REFERENCES 100
APPENDICES 103

APPENDIX 1. DERIVATION OF SINGLE LAYER POTENTIAL REPRESENTATION 104

APPENDIX 2. 2-D BOUNDARY VALUE TEST PROBLEM PLOTS . . . 107

APPENDIX 3. FIVE AND NINE POINT FINITE DIFFERENCE SCHEMES 138

APPENDIX 4. HYPOTHETICAL SOURCE STRENGTHS FOR DIFFERENT NUMBERS OF LOCAL NODES 141

APPENDIX 5. COMPARISON OF WEIGHTING FACTORS BETWEEN THE HSM AND THE NINE NODE FD SCHEME 150

VITA 152

LIST OF FIGURES

FIGURE		PAGE
2.2.1.	Arbitrary points to be used as a stencil	8
2.2.2.	Typical local discretization with 50 hypothetical source points	8
2.2.3.	Sample interpolating stencil	10
2.5.1.	Example of a wave passing through the field at the Nyquist limit	14
3.1.1.1.	Standard grid with standard wave approaching	19
3.1.2.1.	Typical hypothetical source distribution plot	22
3.1.3.1	Standard Case: Magnitude Errors vs. Reduced Frequency	24
3.1.3.2.	Demonstration of Nyquist Limit: k_g from 0 to 10π	25
3.2.1.1.	Effect of Number of Sources: # HS = 8, 20, 50, 200	29
3.2.1.2.	Demonstration of Smaller Error for 8 Hypothetical Sources with Wave Approaching from 0°: 50 Hypothetical Sources Included for Comparison	31
3.2.1.3.	Demonstration of Smaller Error for 8 Hypothetical Sources with Wave Approaching from 0°; 50 Hypothetical Sources Included for Comparison; k_g from 0 to 10	33
3.2.1.4.	Effect of Number of Hypothetical Sources: # HS = 8, 9, 12, 13, 15, 20	35
3.2.2.1.	Hypothetical source strength lots for different numbers of hypothetical sources: k = 0.25, plane wave approaches from an angle of 0° from the right	38
3.2.2.2.	Hypothetical source strength plots for different numbers of hypothetical sources: k = 1.0, plane wave approaches from an angle of 0° from the right	39

3.2.2.3. Hypothetical source strength plots for different numbers of hypothetical sources: k = 1.75, plane wave approaches from an angle of 0° from the right 40

3.2.2.4. Hypothetical source strength plots for different numbers of hypothetical sources: k = 0.25, plane wave approaches from an angle of 22.5° from the right 41

3.2.2.5. Hypothetical source strength plots for different numbers of hypothetical sources: k = 1.0, plane wave approaches from an angle of 22.5° from the right 42

3.2.2.6. Hypothetical source strength plots for different numbers of hypothetical sources: k = 1.75, plane wave approaches from an angle of 22.5° from the right 43

3.2.3.1. Hypothetical Source Radii Comparison: Magnitude Error vs. Reduced Frequency 46

3.2.3.2. Hypothetical source strength distributions for varying HS radii. Figure 4.2.3.1d demonstrates the source strength normalized by [# hypothetical sources] / $\sqrt{k\ [HS\ Radius]}$ 47

3.3.1.1. Singular Value Truncation Multipliers: Multipliers are 10, 100, 1000, 10000, 100000 and 10^{17}; Double Precision; Magnitude Errors vs. Reduced Frequency 50

3.3.1.2. Singular Value Truncation Multipliers: Multipliers are 10, 100, 1000, 10000, 100000 and 10^{17}; Single Precision 51

3.3.2.1. Grids that are used for differing numbers of local nodes in computations, and the axes and bisectors waves can be aligned with 56

3.3.2.2. Varying Number of Local Nodes (4-10) 57

3.3.2.3. Varying Plane Wave Angle Relative to Grid for Different No. of Local Nodes 60

3.3.2.4. Varying Number of Local Nodes (4-10) Using Worst Case Angle . . . 63

3.4.1.1. Multiple Plane Wave Comparison 67

3.4.1.2. Hypothetical source strength distributions for varying numbers of incoming plane waves 69

3.4.2.1. Comparison of Plane, Monopole and Evanescent Wave Computational Accuracy 71

3.4.3.1. Grids used in Aspect Ratio study 73

3.4.3.2. Grids with Different Aspect Ratios: Wave approaching from 15°, Magnitude Errors vs. Reduced Frequency 75

3.4.3.3. Grids with Different Aspect Ratios: Wave approaching from 105°, Magnitude Errors vs. Reduced Frequency 76

3.4.3.4. Hypothetical source strength distributions for different aspect ratios, with a plane wave approaching from 15° 77

3.4.3.5. Hypothetical source strength distributions for different aspect ratios, with a plane wave approaching from 105° 78

3.5.1.1. Comparison of hypothetical source method with 5 and 9 FD methods

3.6.1.1. Case 1: Boundary conditions and Standard Actual Sources 83

3.6.1.2. Case 2: Boundary conditions and Difficult Actual Sources (for extra "odd" HSM case only) 83

3.6.2.1. Comparison Between Methods: Large Test Grid Average Errors 85

3.6.2.2. Comparison Between Methods: Large Test Grid Maximum Errors . . 87

3.6.2.3. Comparison Between Methods: Large Test Grid Standard Deviation 89

3.6.2.4. Hypothetical Source Method Errors: Case 1 91

3.6.2.5. Hypothetical Source Method Errors: Case 2 93

A1.1 Picture of possible fields in question 104

A2.1 Magnitude plots for Case 1, $k_g = 1$ 108

A2.2 Phase plots for Case 1, $k_g = 1$ 114

A2.3 Magnitude plots for Case 1, $k_g = 2$ 120

A2.4 Phase plots for Case 1, $k_g = 2$ 125

A2.5 Magnitude plots for Case 2, $k_g = 1$ 130

A2.6 Phase plots for Case 2, $k_g = 1$ 132

A2.7 Magnitude plots for Case 2, $k_g = 2$ 134

A2.8 Phase plots for Case 2, $k_g = 2$ 136

A4.1. Hypothetical source strength distributions for plane waves that approach from different angles; 4 circularly distributed local nodes with k = 1.0 142

A4.2. Hypothetical source strength distributions for plane waves that approach from different angles; 5 circularly distributed local nodes with k = 1.0 143

A4.3. Hypothetical source strength distributions for plane waves that approach from different angles; 6 circularly distributed local nodes with k = 1.0 144

A4.4. Hypothetical source strength distributions for plane waves that approach from different angles; 7 circularly distributed local nodes with k = 1.0 145

A4.5. Hypothetical source strength distributions for plane waves that approach from different angles; 8 circularly distributed local nodes with k = 1.0 146

A4.6. Hypothetical source strength distributions for plane waves that approach from different angles; 8 local nodes distributed in a box with k = 1.0 147

A4.7. Hypothetical source strength distributions for plane waves that approach from different angles; 9 circularly distributed local nodes with k = 1.0 148

A4.8. Hypothetical source strength distributions for plane waves that approach from different angles; 8 circularly distributed local nodes with k = 1.0 149

NOMENCLATURE

$\vec{a}$	Denotes a vector
a_i	Denotes ith component of vector $\vec{a}$ (tensor notation)
a_{ij}	Denotes ith row and jth column of matrix A
a_{ij}^{+}	Denotes ith row and jth column of pseudo-inverse matrix A
c	Speed of sound
G	Green's function
$H^{(2)}$	Hankel function of second kind
i	$\sqrt{-1}$
J_0	Bessel function of first kind, order 0
k	Reduced Frequency $\left(\frac{\omega L}{c}\right)$
k_g	Reduced Frequency based on grid spacing $\left(\frac{\omega L_g}{c}\right)$
k_d	Reduced Frequency based on grid diagonal $\left(\frac{\omega L_d}{c}\right)$
L	Length parameter (L_d or L_g)
L_d	Length parameter based on mesh diagonal
L_g	Length parameter based on mesh spacing
M	Mach Number

T	Period (time required for wave to travel one wavelength)
v	Velocity of wave
Y_0	Bessel function of second kind, order 0
λ	Wavelength (length)
ϕ	Acoustic potential
ω	Angular frequency = $2\pi/T$ (radians/time)

LIST OF ABBREVIATIONS

Boundary Element Method	BEM
Finite Difference	FD
Hypothetical Source	HS
Hypothetical Source Method	HSM
Single Value Decomposition	SVD

CHAPTER 1

INTRODUCTION

1.1 Overview of the Current Study

The purpose of this thesis is to report the results of numerical experiments conducted in the field of computational acoustics. This thesis studies a unique method for discretizing an acoustic field and compares it with finite differencing methods, to determine the method's advantages or disadvantages in terms of accuracy and efficiency. The method was derived by Dr. J.E. Caruthers, and has previously been applied by Raviprakash [8] for the express purpose of radiating boundary conditions. This thesis evaluates an extension of this method for discretizing the field equations by Caruthers [13].

First covered in this thesis is the purpose and background for this study. The derivation and development of the methodology are then explained, followed by numerical experiments and results. The thesis concludes with suggestions for further work.

1.2 Background

In acoustics, the progress of sound as it travels from a source, through a medium, and interacts with boundaries is studied. The motion of sound in a medium is governed by the Helmholtz equation, which is derived from the perturbation of fluid equations. One purpose of computing the sound in a region is to assist in the design of better products. By numerically simulating the vibrations in a medium surrounding a device that

generates noise, and determining how the device's shape affects the volume and direction of the noise, the device can be designed to reduce unwanted sounds (ex. jet engine) or to better convey desirable sounds (ex. stereo speaker). In electrodynamics, Maxwell's equations often lead to the Helmholtz equation. In that field, it may be used to determine the strength and coverage of electromagnetic waves from a broadcasting radio or television antenna. Alternately, with the proper reflecting boundary conditions, it may be used to examine the radar and sonar "signatures" of planes and ships. Similar methods are used in geophysics. The solution of these problems all require a discretized field with a particular solution driven by external sources. The current derivation of the method requires that the medium must be homogeneous (without variation in the properties of the substance through which the sound travels).

In the problem at hand, we are given particular sound sources that radiate acoustic energy through a given field, with no reflections. Multiple sources have their effects superimposed throughout the given field, combining both constructively and destructively to form regions of louder and softer sound. The "loudness" or amplitude of the interfering sound waves for a point in the field will be referred to as the sound's magnitude. Furthermore, as sound waves travel away from their sources, contours can be devised to show the directions in which the superimposed waves travel. The contour parameter varies cyclically from 0 to 2π, representing a phase angle for a point in the field, and will be referred to as the phase. For computation purposes, a field point's magnitude and phase information are contained in the acoustic potential, a complex number.

Before a numerical technique is applied, the given field must be discretized, with specific points in the field selected for computation of the acoustic potential. The actual values of the sound are known only at boundaries through which the oncoming sound travels (Dirichlet boundary conditions), and the sound is allowed to exit the field using

radiation boundary conditions (Raviprakash [8]). The goal of this new technique is to compute the acoustic potential for the rest of the points in the field, in the space between the boundaries.

Current methods that are used to compute the acoustic potential include the boundary element, finite element and spectral methods, Finite Difference (FD) including central differencing and implicit finite difference (IFD), and ordinary differential equation (ODE) methods. With these methods, potential difficulties include the presence of full matrices and unrealistic solution times. Furthermore, as with computational fluid dynamics, one cannot model only the near field, but must include the far field in calculations to allow the waves in the solution to dissipate, ensuring that errors due to discretized boundary conditions are not reflected back in, thus contaminating the solution.

To include the far field in computations requires that the field have points computed in regions of little interest. Caruthers [2] and Raviprakash [8] have previously dealt with this problem by formulating a radiation boundary condition that allows acoustic energy to flow out of a near field boundary without any reflections. Therefore, only the near field needs to be computed. The problem of full matrices and long solution times is dealt with by a new field discretization presented by Caruthers [13]. It can be formulated to furnish banded matrix structures and does not need as many points computed in the field as other methods for high reduced frequencies, increasing the computation speed. This thesis applies Caruther's [13] discretization, and presents a compilation of computational experiments to evaluate the new discretization method.

CHAPTER 2

DEVELOPMENT AND METHODOLOGY

2.1 Purpose

A faster and more efficient method is needed to solve large scale Helmholtz-type problems, as current methods are too slow to handle large problems with both reasonable resolution and computation speed. Central differencing has an inherent truncation error that requires denser meshes for higher reduced frequencies, when the reduced frequency is a function of the grid spacing. Acoustics literature is filled with examples of new ways to improve the accuracy of the differencing, but ultimately truncation error still remains. Alternately, Boundary Element Methods (BEM), based on exact solutions of the field equations, convert a volume integral into a surface integral to both solve and reduce the size of the problem. However, these require large fully populated matrices that need to be manipulated, and if a medium is inhomogeneous, the BEM cannot be used.

To avoid truncation error, one must consider the following statement from an article by Pierce that makes recommendations for developing algorithms for inhomogeneous fields: "... there is some historical precedent to believe that any scheme that incorporates more of the basic physical understanding of how waves propagate should have some intrinsic advantages over one based on brute force." [9, p. 64] Most discretization schemes today are based on approximations rather than exact solutions of the differential equations.

To avoid the BEM problem of fully populated matrices, local discretizations are necessary for limiting the problem to simple banded matrices. To set up banded matrices,

each point must be related only to neighboring points. A local discretization also may be used to handle inhomogeneous problems with a small loss of accuracy. The challenge is to find a discretization that does not involve approximations to compute a point in the field. The new method investigated herein may be thought of as a "local" BEM, computed for each node. Each node has a discretized hypothetical "boundary surface". Using Green's theorem, a volume integral may thereby be reduced to a surface integral, which can be utilized to compute any interior point if the boundary is known (see Appendix 1).

The original derivation of this discretization was to provide radiating boundary conditions in an effort to reduce the size of a grid used for the computation of the acoustic field near a particular source (in this case, the turbofan inlet of a jet engine). The computations assumed that there was no noise coming into the grid from the far field, and that the position of the source of the sound was known. Since all of the acoustic waves produced were supposed to be traveling outward (away from the sources), it was greatly desirable to develop a method that would allow acoustic waves to pass out of a grid without having to extend the grid into the far field, requiring only the calculation of the near field.

In an effort to avoid overlooking any potential opportunities, Caruthers asked the author to examine and experiment with a very similar discretization scheme to see if it had any advantages or incentives for using it as a general field discretizing method.

The first attempt at solving the problem used a one dimensional discretization. Caruthers analytically showed that it produces an exact solution to the problem. This provided the impetus to continue the development - if the solution technique provided an exact solution in one dimension, how accurate would the solution be in two dimensions?

2.2 Discretization of the Field

Following the method proposed by Caruthers [13], the field is discretized by setting up two systems of equations for a subject node and its neighboring "local" nodes in terms of the same unknown "hypothetical sources". To discretize the field, a grid of nodes must first be established. This grid does not have to be uniform, and even a random grid with a reasonable distribution of nodes should work. However, Cartesian and skew-Cartesian grids are easily set up in a block tri-diagonal matrix form. The hypothetical sources are placed far from the stencil (a set of points that will be used for the local discretization), so by the time their wave front reaches the point to be computed, the wave is nearly a plane wave. The idea is to re-create any wave approaching from any direction with a superposition of plane waves of different magnitudes and phases.

To simplify the derivation and the computations, it is desirable to define a stencil for a group of discrete points in the field. In this study, only the two dimensional case will be examined. The stencil contains a specific point to be computed (the circle in fig. 2.2.1), and nearby points whose weighted combination provides an approximation to the computed points (the X's in fig. 2.2.1). From here on the computed point (circle) will be referred to as the computed node, and the nearby points used to approximate the computed node will be referred to as local nodes. If the mesh is uniform in spacing and geometry, this stencil can then be shifted over any point in the field and have identical weights; otherwise it will have to be recomputed for each point in the field. Applying the stencils to the interior nodes creates a system of equations that can be solved through matrix inversion. The stencil should not be centered on the boundary, because local nodes need to surround the computed node to provide information concerning waves that approach the stencil from all directions. However, placing the stencil on the boundary

leads to a general radiation boundary condition with an unknown source location, which is beyond the scope of this thesis. The remainder of this chapter deals with a new way to relate the nearby points to the computed point in the stencil.

In figure 2.2.2, the small circles represent possible locations of the hypothetical sources, encircling the stencil. The hypothetical sources are positioned on a local "boundary". This boundary is a discretized single layer potential surface, and is centered about the computed node. Since the stencil can be moved to be centered over any node in the field, each computed node is at the center of its own "boundary".

The following table correlates the terminology, figures, and mathematical symbols:

Term	Representation in figures	Symbol
Computed Node	Circle	ϕ'
jth Local Node	X	ϕ_j
ith Hypothetical Source	Small Circle	σ_i

Green's functions reveal the manner in which a source point in a field affects other points in that field. From fig. 2.2.2, let the Green's function for the first hypothetical source's (σ_1) influence on the computed node (ϕ') be G_1'. The prime indicates that the Green's function in question refers to a computed node. Similarly, let the Green's function for the influence of a second hypothetical source (σ_2) on the first local node (ϕ_1) be G_{12}. Thus, the first index indicates the local node acted upon, while the second index indicates the particular hypothetical source. Note that the earlier prime on G is used to distinguish the computed node Green's function vector from the local nodes' G matrix. Using this notation, two systems of equations can then be set up (using summation notation):

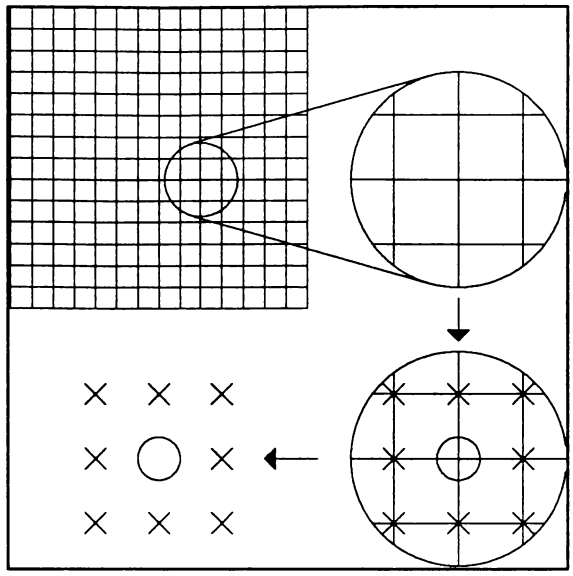

Figure 2.2.1. Arbitrary points to be used as a stencil

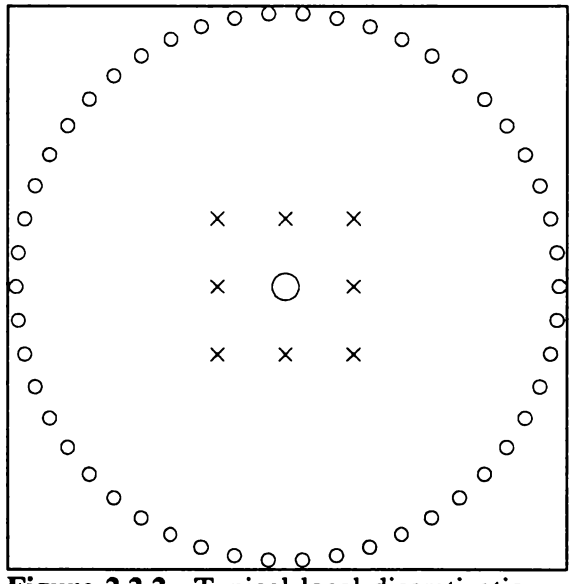

Figure 2.2.2. Typical local discretization with 50 hypothetical source points

For the computed node:

$$\phi' = G_i' \sigma_i \tag{2.1}$$

For the local nodes:

$$\phi_j = G_{ji} \sigma_i \tag{2.2}$$

Here ϕ_j (j = 1, 2, ... # of local nodes) represents a vector of local nodes that surround the computed node. If G_{ji} is a square matrix (i.e. the no. of hypothetical sources = no. of local nodes) then we may invert the solution for the local nodes:

$$[G_{ji}]^{-1} \phi_j = \sigma_i \tag{2.3}$$

Substituting this into the center node equation, we can eliminate the hypothetical source terms to find:

$$\phi' = G_i' [G_{ji}]^{-1} \phi_j \tag{2.4}$$

As a result, we now have an explicit equation for the center node in terms of the surrounding nodes. The information concerning the influence of hypothetical sources is hidden in the Green's functions. This $G_i' [G_{ji}]^{-1}$ vector is the same for every computed point in the field (if the mesh is Cartesian or skew-Cartesian), since the stencil was derived without reference to its position in the field. The position vectors of both the local nodes and the hypothetical sources are measured relative to the computed node, and are the same for each stencil.

Once the field is computed for each of the nodes, a similar method can be used to interpolate the acoustic field between the nodes for plotting at a higher resolution. First, a node that is to be interpolated and is not one of the computed nodes is selected

(called ϕ''). This node uses the previously computed nodes as local nodes (ϕ_j), resulting in a similar equation for ϕ'':

$$\phi'' = G_i''[G_{ji}]^{-1}\phi_j \tag{2.5}$$

The Green's function vector (G_i'') must be recomputed for each new position to be interpolated inside the region surrounded by the local nodes (see figure 2.2.3). Similarly, for Cartesian or skew-Cartesian meshes, a $G_i''[G_{ji}]^{-1}$ vector needs to be computed for each interpolation inside an interpolating stencil. The set of vectors for the interpolated points will also form a set of interpolating stencils that can be moved to center over any computed node.

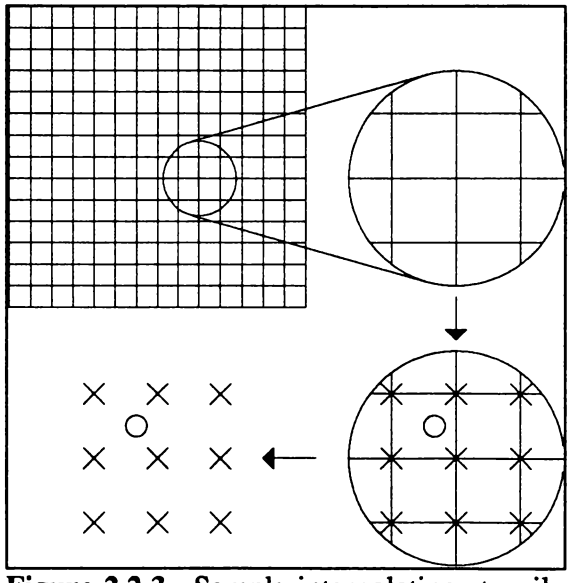

Figure 2.2.3. Sample interpolating stencil

2.3 Determine Appropriate Green's Function

For the Helmholtz equation in potential form $\nabla^2\phi + k^2\phi = 0$, a wave's amplitude and phase values over a distance from the wave's source can be described by free space Green's functions satisfying the equation

$$\nabla^2 G + k^2 G = -\delta(\vec{r} - \vec{r}_0) \qquad \text{(A1.5)}$$

and the outgoing wave condition (Sommerfeld condition). For the Helmholtz equation, harmonic time dependence is assumed and is factored out. There are three different complex Green's functions for one, two, and three dimensions:

1-D: e^{-ikr}

2-D: $H_0^{(2)}(kr) = \frac{2i}{\pi}\int_1^\infty e^{-ikrs}\frac{ds}{(s^2-1)^{1/2}} = J_0(kr) - iY_0(kr)$, [4, pg. 58], [15, eq. 9.1.4]

3-D: $\frac{e^{-ikr}}{4\pi r}$

Note that the Green's function is a function of the distance (r) between the source and the listening point, and the reduced frequency (k). The method presented works in different dimensions by changing the particular Green's function used.

2.4 Under-Constrained Field and Use of SVD

The normal method of solution would have as many hypothetical sources as local nodes, and the number of equations would equal the number of unknowns. By increasing the number of hypothetical sources, the system of equations becomes under-constrained.

In doing so, a smoother artificial boundary is created and the ability of the hypothetical sources to reconstruct incoming waves using superposition of plane waves is increased.

To solve the under-constrained system, Singular Value Decomposition (SVD) from the LINPACK FORTRAN codes is used [3]. The under-constrained system does not have a unique solution, but can have a least-squares solution. The question then lies in determining which least-squares solution is the best. SVD finds the least-norm least-squares fit, a unique solution. (Although other norms might possibly provide better results, they are beyond the scope of this study.)

SVD separates a matrix into two orthogonal matrices Q_1 and Q_2, and a diagonal matrix Σ:

$$G_{ji} = Q_1 \Sigma Q_2^T$$

The Σ diagonal elements are known as the singular values. If the matrix is not invertible, Q_1, Σ and Q_2 will have different dimensions. Using Q_1, Σ and Q_2, the pseudo-inverse G_{ij}^+ of $[G_{ji}]^{-1}$ can be computed:

$$[G_{ji}]^{-1} = G_{ij}^+ = Q_2 \Sigma^+ Q_1^T$$

The pseudo-inverse (G_{ij}^+) will be used in place of $[G_{ji}]^{-1}$, so that

$$\phi' = G_i' G_{ij}^+ \phi_j \qquad (2.3)$$

The singular value diagonal (Σ) that the LINPACK SVD routine returns contains values numerically ordered from highest to lowest. The small singular values become large when Σ is inverted (Σ^+). Singular values which are small and inaccurate (due to computation truncation) can create large errors in the pseudo-inverse. To remedy this

potential problem, if the values become too small, they can be truncated by reducing the rank of the Σ matrix.

2.5 Nyquist Limit and Resonant Frequency

To determine the efficiency of this method, the Nyquist limit may be used to limit the reduced frequency (k). This limit is the theoretical minimum number of samples required to reconstruct a wave, and it determines how coarse a mesh may be used without loss of accuracy. In two dimensions, the Hankel function yields waves that decay by $1/\sqrt{r}$ as they leave the origin. Once at sufficient distance, these waves are similar to plane waves. The Nyquist limit states that to correctly sample a signal, more than two samples must be taken per wavelength to reproduce the wave mathematically. To transfer this limit to the computational field, at least two grid nodes per plane wave are required to properly reconstruct the plane wave. More complicated waves may require more computational nodes or a lower reduced frequency.

Most of the numerical experiments included in this thesis vary the reduced frequency (k) from 0 through the Nyquist limit:

$$k = \frac{\omega L}{c} \tag{2.4}$$

- ω is the angular frequency
- L is a length parameter chosen based on the geometry of the grid. The proper length to be used to determine the limiting reduced frequency for a problem is the longest length within the local discretization.

- c is the speed of sound in the medium. For the current use, the medium must be homogeneous and motionless. This is reflected by the corresponding Green's function used.

For the reduced frequency to reach the Nyquist limit, the value of the reduced frequency must be such that a wave with this reduced frequency could fit an entire wavelength across the discretized region, regardless of the actual direction of incoming waves (see fig. 2.5.1). When the Nyquist limit is reached, a wave can fit within the local discretized region, and erroneous homogeneous solutions overwhelm the particular solution of the differential equation.

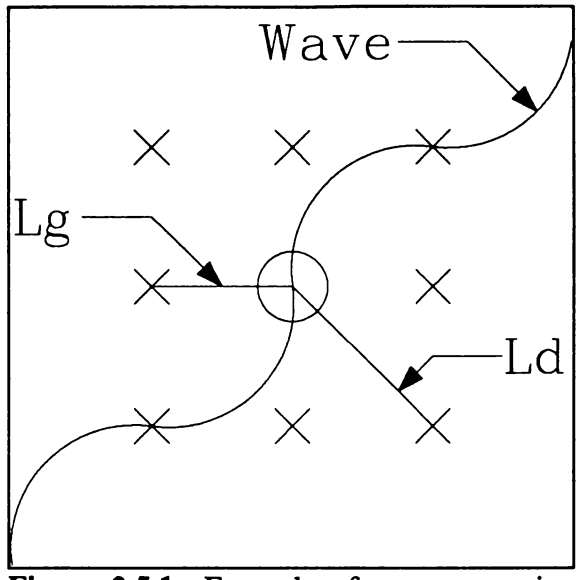

Figure 2.5.1 Example of a wave passing through the field at the Nyquist limit.

The wavelength (λ) that will cause problems at the Nyquist limit is the longest distance across the discretized field. From figure 2.5.1 ($\Delta x = \Delta y$), this $\lambda = 2\sqrt{2}L_g = 2L_d$. By definition, $\lambda = vT$. In this study, $v = c$ and $T = 2\pi/\omega$, so $\lambda = \frac{2\pi c}{\omega}$. Rearranging these terms,

$$\lambda = \frac{2\pi c}{\omega} \rightarrow \frac{c}{\omega} = \frac{\lambda}{2\pi} \rightarrow \frac{\omega}{c} = \frac{2\pi}{\lambda}$$
$$\therefore k = \frac{\omega L}{c} = \frac{2\pi L}{\lambda} \qquad (2.5)$$

Substituting the wavelength at the Nyquist limit yields:

$$k = \frac{2\pi L}{\lambda} = \frac{2\pi L}{2\sqrt{2}L_g} = \frac{\pi L}{\sqrt{2}L_g}$$
$$or\ k = \frac{2\pi L}{2L_d} = \frac{\pi L}{L_d} \tag{2.6}$$

The Nyquist limit is reached for k based on the grid spacing ($L = L_g$) at $\pi/\sqrt{2}$, and for k based on the diagonal ($L = L_d$) at π. The reduced frequency normalized by the diagonal is useful for comparing results from different aspect ratios (i.e. different cartesian grid diagonals), as shown in section 3.4.3.

To simplify the textual notation determining how the reduced frequency has been normalized, let

$$k_g = \frac{\omega L_g}{c} \tag{2.7}$$

and

$$k_d = \frac{\omega L_d}{c} \tag{2.8}$$

A similar, more general limit is found in the resonant frequency of the grid in question. As with the Nyquist limit, the resonant frequency corresponds to an infinite number of homogenous solutions that overwhelm the particular solution. For the 3x3 box, this frequency is $k_{mn} = \pi\sqrt{\left(\frac{m}{2}\right)^2 + \left(\frac{n}{2}\right)^2}$. If each of the mode numbers equals one, this provides $k_{mn} = \pi/\sqrt{2}$ as anticipated.

The resonant frequency can be extended to "n-gon" and three dimensional grids. N-gons are n local nodes placed on a unit circle, and equally spaced around it. Because

there are no sources in the field, the homogenous solution to the 2-D Helmholtz equation for a circle reduces to $J_0(kr)$. The first root of $J_0(kr)$ is k = 2.4048255577 [15, p. 409]. This is the error peak found for n-gons in Chapter 3. Furthermore, for 3-D, Raviprakash has written a 3-d code which verifies that the cube resonant frequency, $k_{lmn} = \pi\sqrt{\left(\frac{l}{2}\right)^2 + \left(\frac{m}{2}\right)^2 + \left(\frac{n}{2}\right)^2}$, l = m = n = 1, $k_{lmn} = \sqrt{3}\pi/2$, providing a consistent theory for the error peak.

CHAPTER 3

NUMERICAL EXPERIMENTS, RESULTS AND HYPOTHESES

3.1 Introduction

The vital questions grappled with herein do not involve the Hypothetical Source Method's derivation or its practical applications, but instead examine its viability and accuracy: Will it work? If so, how well? Under what conditions will it fail? Furthermore, we want to understand why it works.

To answer these questions, two approaches were taken. The reduced frequency is a major factor in determining the accuracy of the solution. By knowing the level of accuracy for a range of reduced frequencies (based on the grid spacing), the number of nodes that will be needed for future computations can be determined. This is done by testing the interpolation properties of the HSM given a single stencil with local nodes set to the exact solution. To understand how the hypothetical source method actually works, it is useful to look at the magnitudes of the hypothetical sources, to glean an understanding of the overall method.

There are many parameters that determine the accuracy of the method, but they act as perturbations to the accuracy for varying values of the reduced frequency. To examine how these other factors affect the accuracy, test cases are constructed in which all but one of the parameters is held constant (see section 3.1.1 for the chosen constants). The parameter not held constant is varied, and is used to determine the accuracy of the

solution for many different values of reduced frequency, to see how it perturbs the accuracy. The parameters that are varied are:

- Reduced frequency (standard for comparison, section 3.1.3)
- Number of hypothetical sources (section 3.2.1)
- Radius of the hypothetical sources (section (3.2.3)
- Number of truncated singular values (section 3.3.1)
- Maximum number of singular values (number of local nodes, section 3.3.2)
- Incoming direction for the plane wave (section 3.3.2)
- Number and kind of sound sources (section 3.4.1, 3.4.2)
- Aspect ratio (section 3.4.3)

To determine how the hypothetical sources function in the discretization, sometimes the parameters need to be varied in combinations to examine the behavior of the sources. These factors include the:

- Reduced frequency (section 3.2.2)
- Number of hypothetical sources (section 3.2.2)
- Incoming direction for the plane wave (section 3.2.2)
- Radius of the hypothetical sources (section 3.2.3)
- Number of plane waves used (section 3.4.1)
- Number of local nodes (Appendix 4)

To compare the HSM with current methods, two different finite difference schemes have also been examined for accuracy (sections 3.5 and 3.6).

3.1.1 The Standard Case

Many combinations of parameters can be chosen, but parameters randomly selected do not reveal any patterns from which hypotheses can be formed. For the sake of simplicity and uniformity, a standard set of parameters are used in the following studies unless otherwise noted. The parameters chosen define a standard for the accuracy (section 3.1.3). When these parameters are varied, computations yield a perturbation of the standard accuracy. The standard parameters are as follows:

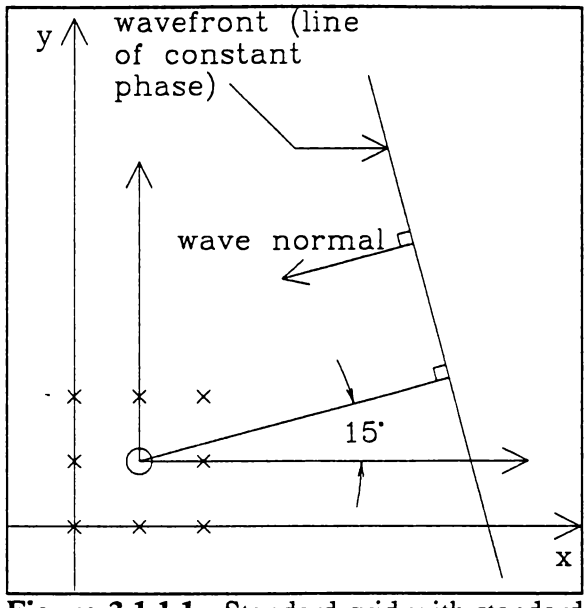

Figure 3.1.1.1. Standard grid with standard wave approaching

- The Grid structure is square
- The grid's center node is the only node computed
- One plane wave is passed though the computational domain
- The plane wave approaches the computed node from an angle of 15° relative to the x-axis (see fig. 3.1.1.1)
- $L_g = 1$
- $L_d = \sqrt{2}$
- All positions are non-dimensionalized by L_g
- Number of Hypothetical Sources = 50
- Hypothetical Source Radius (HS Radius) = 1000.0
- Singular Value Truncation Multiplier = 100000.0
- Aspect Ratio = 1:1

3.1.2 Types of Plots

Three kinds of plots are used to convey the experimental results: error vs. k Cartesian plots, error vs. angle Cartesian plots, and hypothetical source strength polar plots.

Plane waves have been chosen as the standard wave for the computations. The acoustic potential has exact analytical solutions for plane waves, monopoles and evanescent waves. and these exact solutions are used to compute exact values for the 8 local nodes in fig. 3.1.1.1. The computed node of fig. 3.1.1.1 is the only node whose acoustic potential is to be determined. To determine the accuracy of the method, the exact solution is compared with the computed solution. The errors used are magnitude and phase errors of the acoustic potential. The magnitude error is computed relative to the exact solution:

$$\phi = a+ib, \quad |\phi| = \sqrt{a^2+b^2}$$

$$Mag\ Error = \frac{\left|\ |\phi_{exact}| - |\phi_{calc}|\ \right|}{|\phi_{exact}|} = \left| 1 - \frac{|\phi_{calc}|}{|\phi_{exact}|} \right| \qquad (3.1)$$

$$Mag\ Error \geq 0$$

As shown in equation (3.1), the acoustic potential is a complex number, and the absolute value symbols represent the magnitude of a complex number. The phase error is normalized by 2π, and is computed by equation (3.2):

$$0 \leq \tan^{-1}x \leq 2\pi$$

$$Phase\ Error = \frac{1}{2\pi}\left|\tan^{-1}\left(\frac{b_{exact}}{a_{exact}}\right) - \tan^{-1}\left(\frac{b_{calc}}{a_{calc}}\right)\right| \qquad (3.2)$$

$$if\ Phase\ Error > 0.5\ then\ Phase\ Error = 1 - Phase\ Error$$

$$0 \leq Phase\ Error \leq 0.5$$

The error plots' scaling is linear for the x axis, and logarithmic for the y axis. The logarithmic scales reveal details of increasing errors at small values of reduced frequency that cannot be discerned with linear y axis plots. Using the logarithmic y axis, the error vs. k plots are nearly linear for large portions of the ranges covered, implying that the errors increases exponentially for increasing values of the reduced frequency. Note that often for plane wave solutions the phase error is 0. This is because a plane wave's phase at the center of the box is the average of the phases of the local nodes around it.

Both reduced frequency and angle error plots are produced by running the calculations 1000 and 450 times, respectively, each time incrementing the reduced frequency by $\pi/1000$ or the angle by 0.1°. The resulting plots of the errors are remarkably smooth for calculations conducted with double precision. Single precision plots only become smooth once the method's errors become much greater than the significant digit truncation errors, at which point the resonant frequency limit has been surpassed and the solution becomes incorrect regardless. Occasionally a spike appears in these error plots, representing a point at which the SVD routine could not correctly compute all of the singular values. The SVD routine warns the user when such occasions occur.

The hypothetical source strength plots show how the SVD's least-norm, least-squares characteristics distributes "loudness" around the circle of hypothetical sources. In this study, all of the sources are inscribed on a circle at equal intervals (see fig. 2.2.2). The hypothetical source strength plots are polar plots with coordinates r and θ (see figure 3.1.2.1). The radius r is the magnitude of the strength of the hypothetical source (the magnitude of a complex number), and the angle θ is the angle along which the hypothetical source is positioned relative to the computed node and the x axis.)

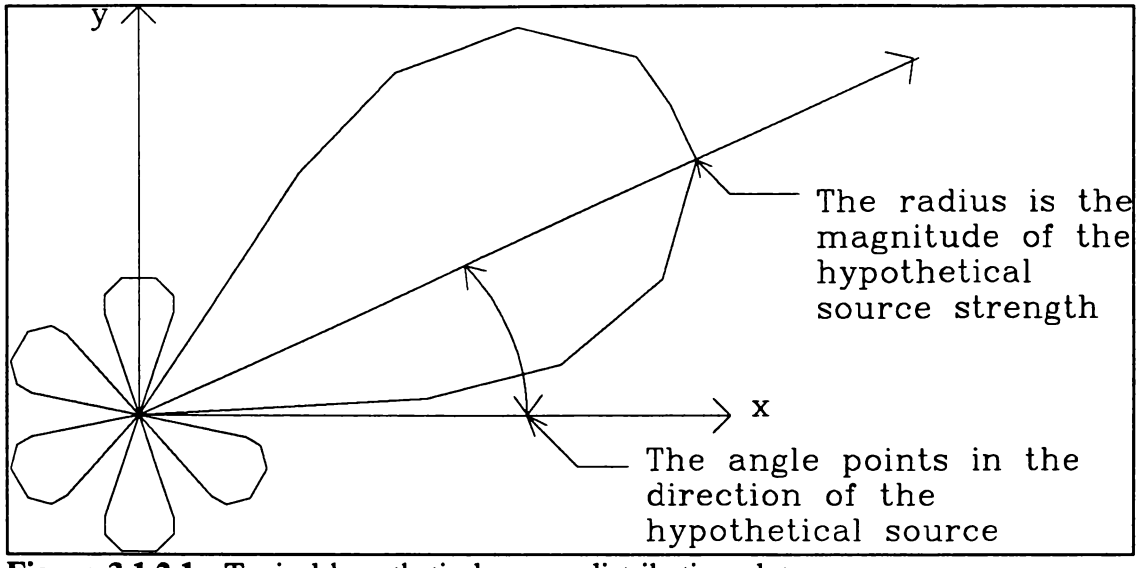

Figure 3.1.2.1. Typical hypothetical source distribution plot

3.1.3 Limitations

This section examines the standard case when only the reduced frequency is varied. The rest of the cases in this chapter can be viewed as perturbations of this case. Observed in figure 3.1.3.1 a sharp discontinuity arises when $k_g = 2.221$ (the discontinuity near $k_g = 0.2$ is due to the elimination of singular values - see section 3.1.2). For this case no phase error is shown, as the phase error is negligible for 50 hypothetical sources (section 3.1.2).

The 2.221 is remarkably close to $\pi/\sqrt{2}$. The $\sqrt{2}$ is the diagonal distance between nodes on the square grid (see fig. 2.5.1). This matches the Nyquist limit computed in section 2.5. The solution method returns poor results after $k_g = 2$, as would be expected. Beyond $k_g = 2.221$, the method returns solutions that, when plotted, follow smooth but erroneous curves, similar to false Fast Fourier Transform results which arise from sampling a signal too slowly (see figs. 3.1.3.2a+b).

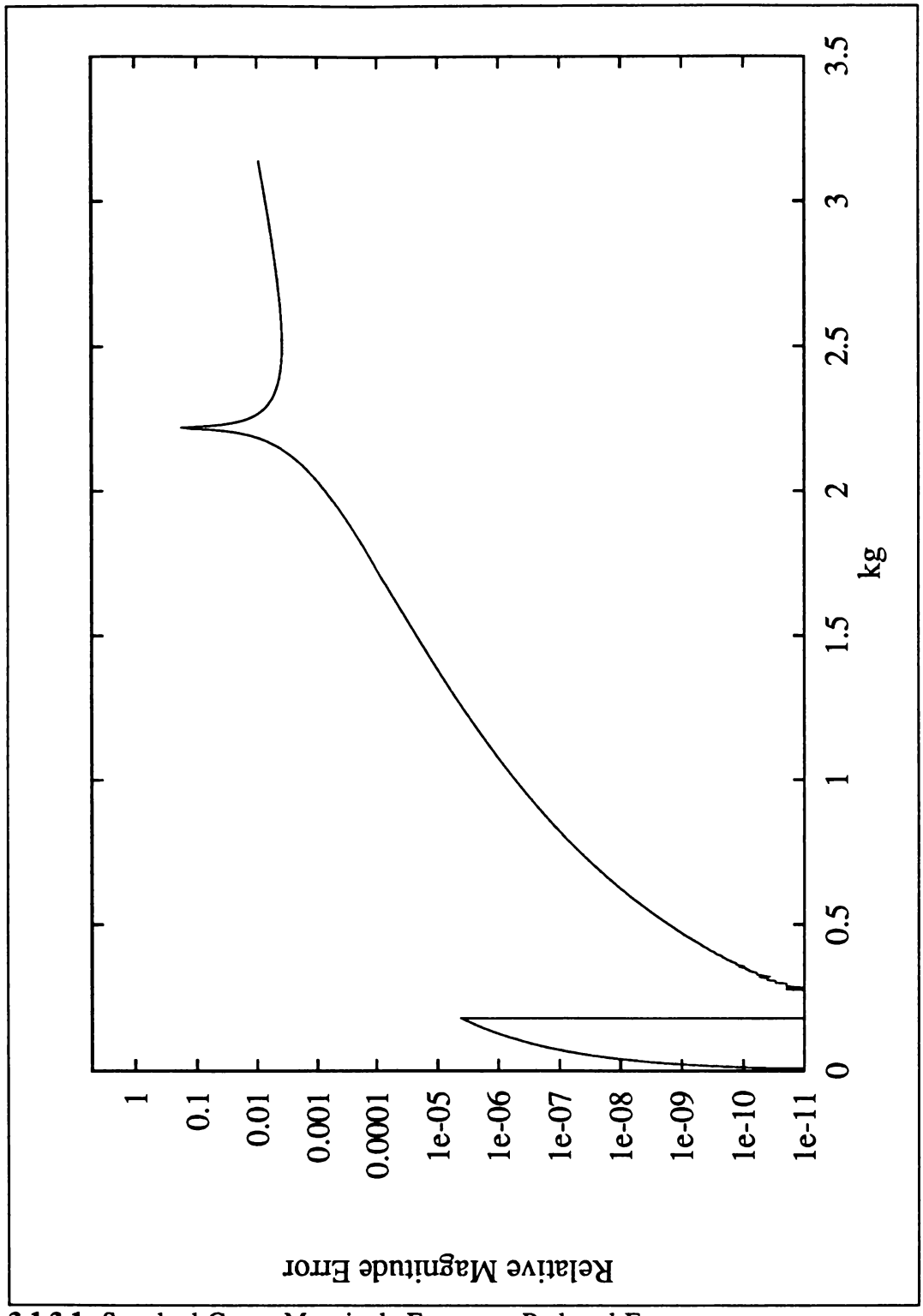

3.1.3.1 Standard Case: Magnitude Errors vs. Reduced Frequency

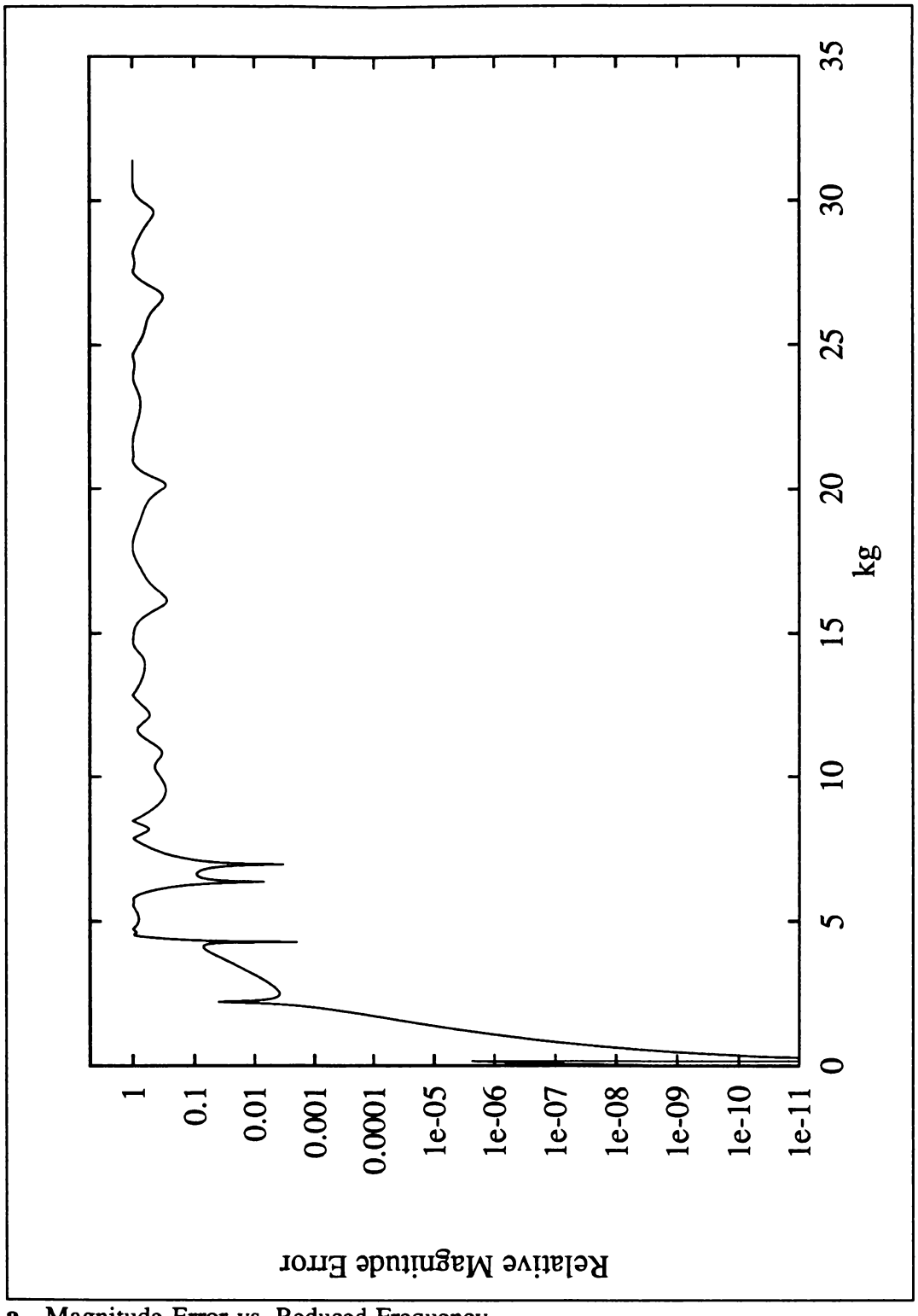

a. Magnitude Error vs. Reduced Frequency

Figure 3.1.3.2. Demonstration of Nyquist Limit: k_g from 0 to 10π

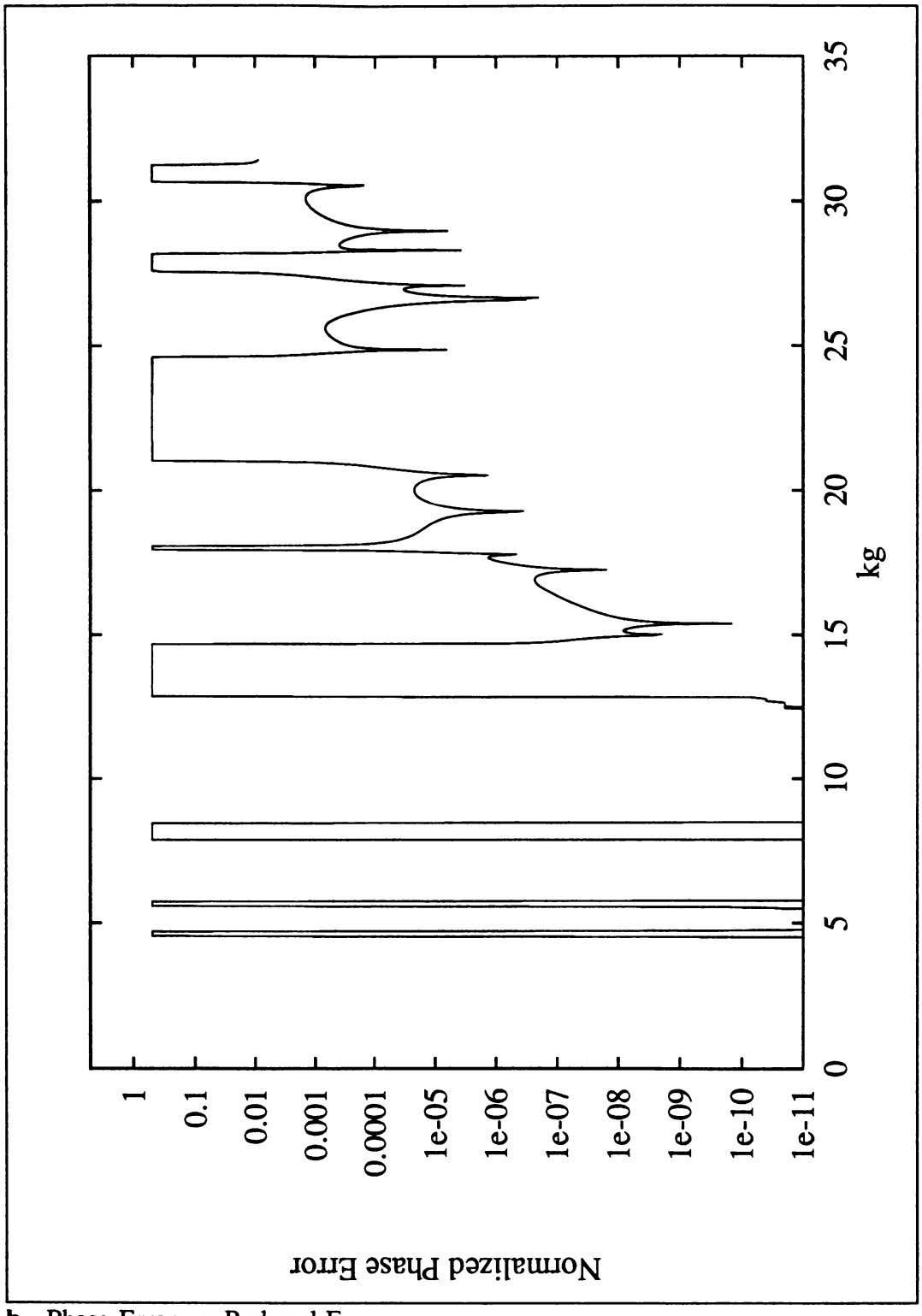

b. Phase Error vs. Reduced Frequency

Figure 3.1.3.2. (continued)

3.2 Hypothetical Source Studies

3.2.1 Number of Hypothetical Sources

This section examines how is the accuracy is affected when the number of hypothetical sources is varied. The first portion of the section focuses on the relative errors as a function of the total number of hypothetical sources. This study uses the standard case (section 3.1.1), except that 8, 20, 50 and 200 hypothetical source nodes are used. The eight hypothetical source case was included as this is the minimum number of possible hypothetical sources which can be around the computed node: any fewer and the number of variables would be fewer than the number of equations. The other values were chosen to encompass a large range.

In figure 3.2.1.1a, a gap may be observed between eight hypothetical sources and the 20, 50 and 200 source cases. The lines representing 20, 50 and 200 hypothetical sources are for the most part superimposed, and the 8 case is above them. The rising number of hypothetical sources does increasingly improve the accuracy of the phase, and, as seen in figure 3.2.1.1b, by the time 50 hypothetical sources are used, the phase error incurred is below the presented minimum.

Notably, with 8 hypothetical sources, if the oncoming plane wave's normal is collinear with a hypothetical source, a calculation node and the computed node (and in this case with a second hypothetical source and a second local node) the solution will have no magnitude error for reduced frequencies less than the resonant frequency. This is similar to the one dimensional case which has an exact solution. The magnitude and phase errors are then examined for large values of the reduced frequency (k_s) to determine how long this characteristic lasts. Figures 3.2.1.2a+b and 3.2.1.3a+b show that while the

magnitude error remains relatively accurate, there is a phase error of the same order. The 50 hypothetical sources case is included for comparison. This technique cannot generally be used, as typical cases do not have waves aligned with the mesh.

In general, the solution derived from using eight sources is less accurate than solutions that used a larger number of sources. By increasing the number of hypothetical sources, more incoming plane waves are available to be superimposed in order to reconstruct the original plane wave. There is a range between 8 and 15 hypothetical sources in which the magnitude accuracy improves with the increasing number of hypothetical sources by about half a magnitude, while the phase error increases dramatically (see figs. 3.2.1.4a+b). After 15 sources, the accuracy in the magnitude is not significantly affected, but the phase error continues to diminish. For more difficult wave forms, more hypothetical sources may be required to maintain a high level of accuracy.

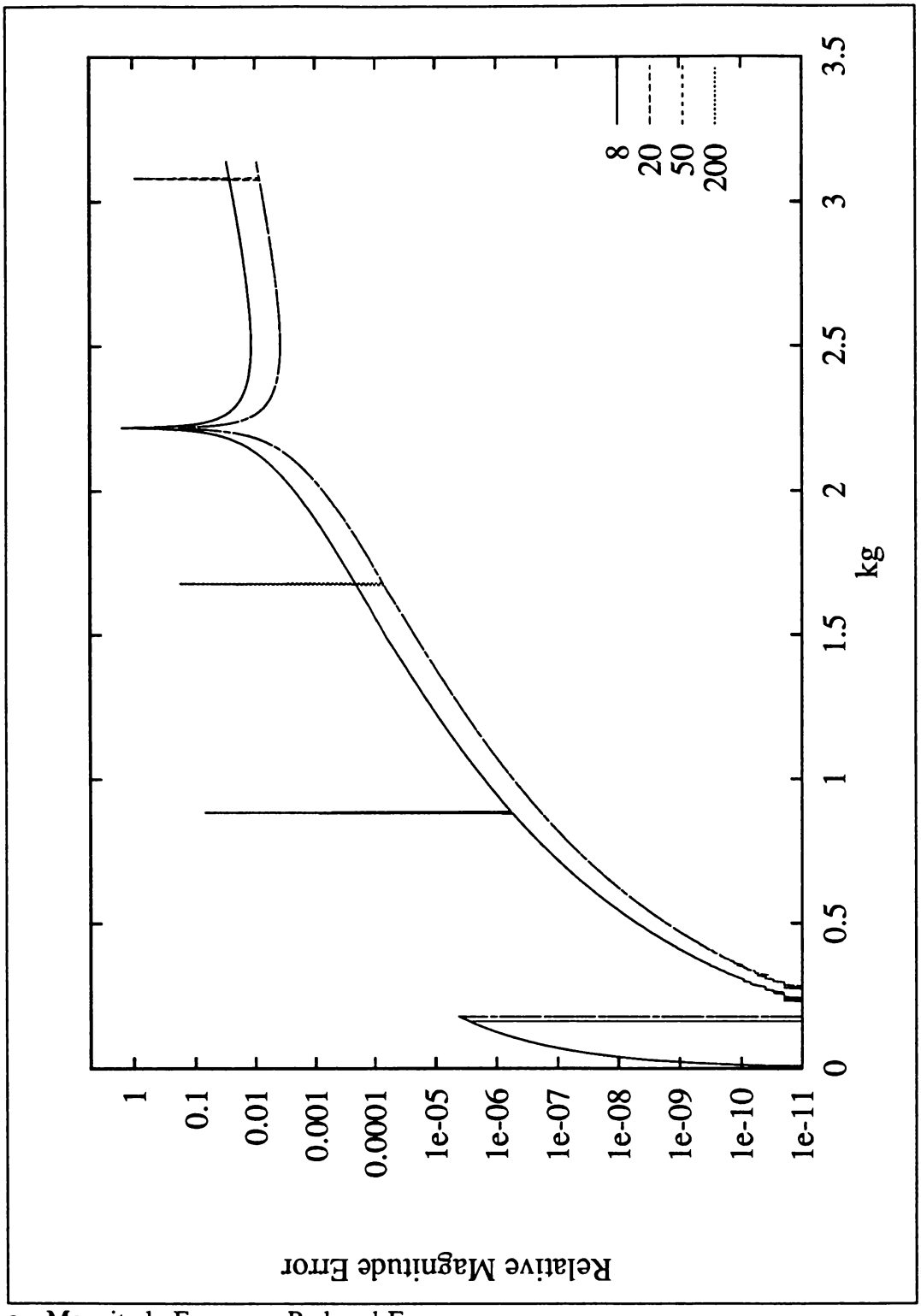

a. Magnitude Errors vs. Reduced Frequency

Figure 3.2.1.1. Effect of Number of Sources: # HS = 8, 20, 50, 200

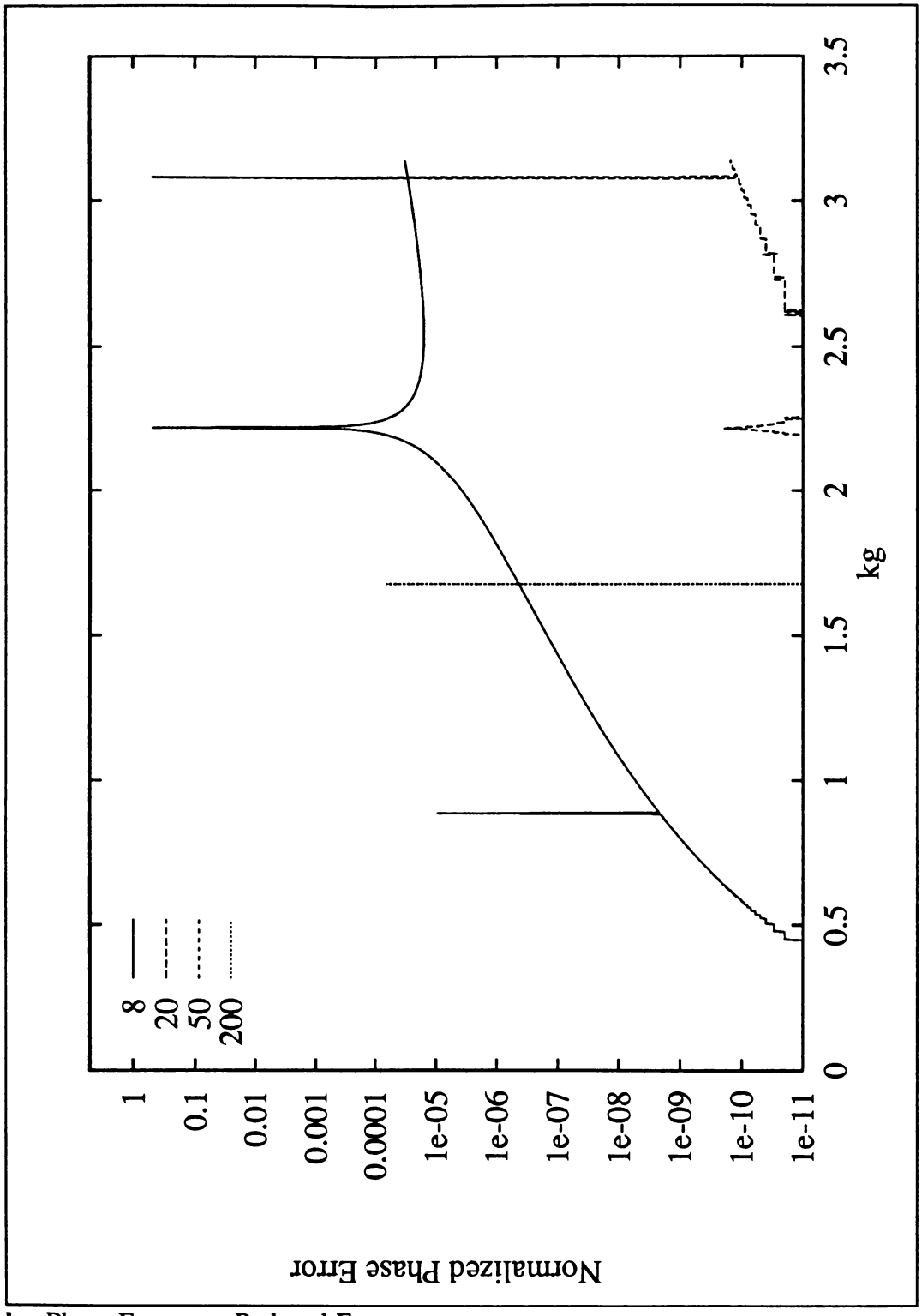

b. Phase Errors vs. Reduced Frequency

Figure 3.2.1.1. (continued)

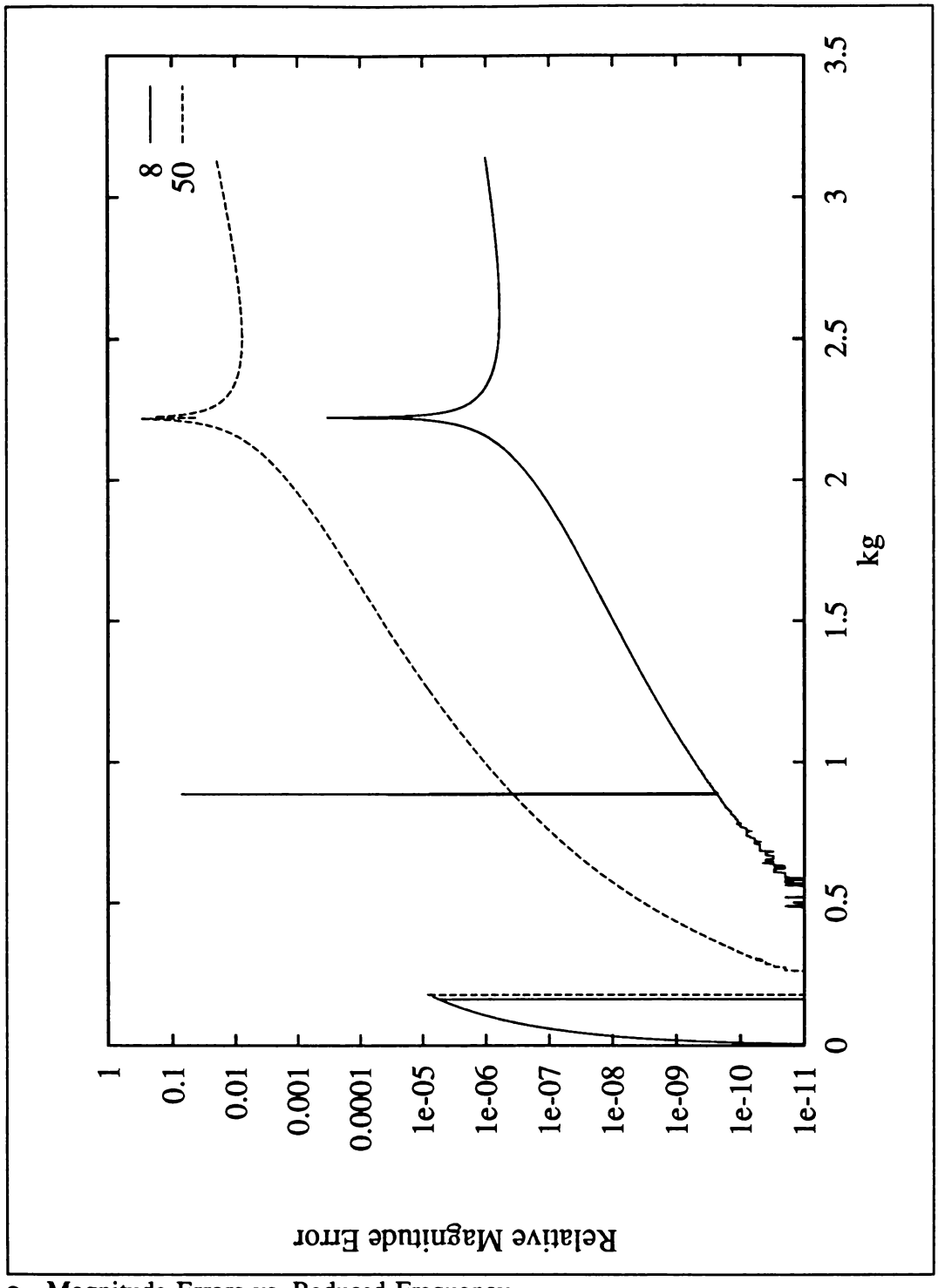

a. Magnitude Errors vs. Reduced Frequency

Figure 3.2.1.2. Demonstration of Smaller Error for 8 Hypothetical Sources with Wave Approaching from 0°: 50 Hypothetical Sources Included for Comparison

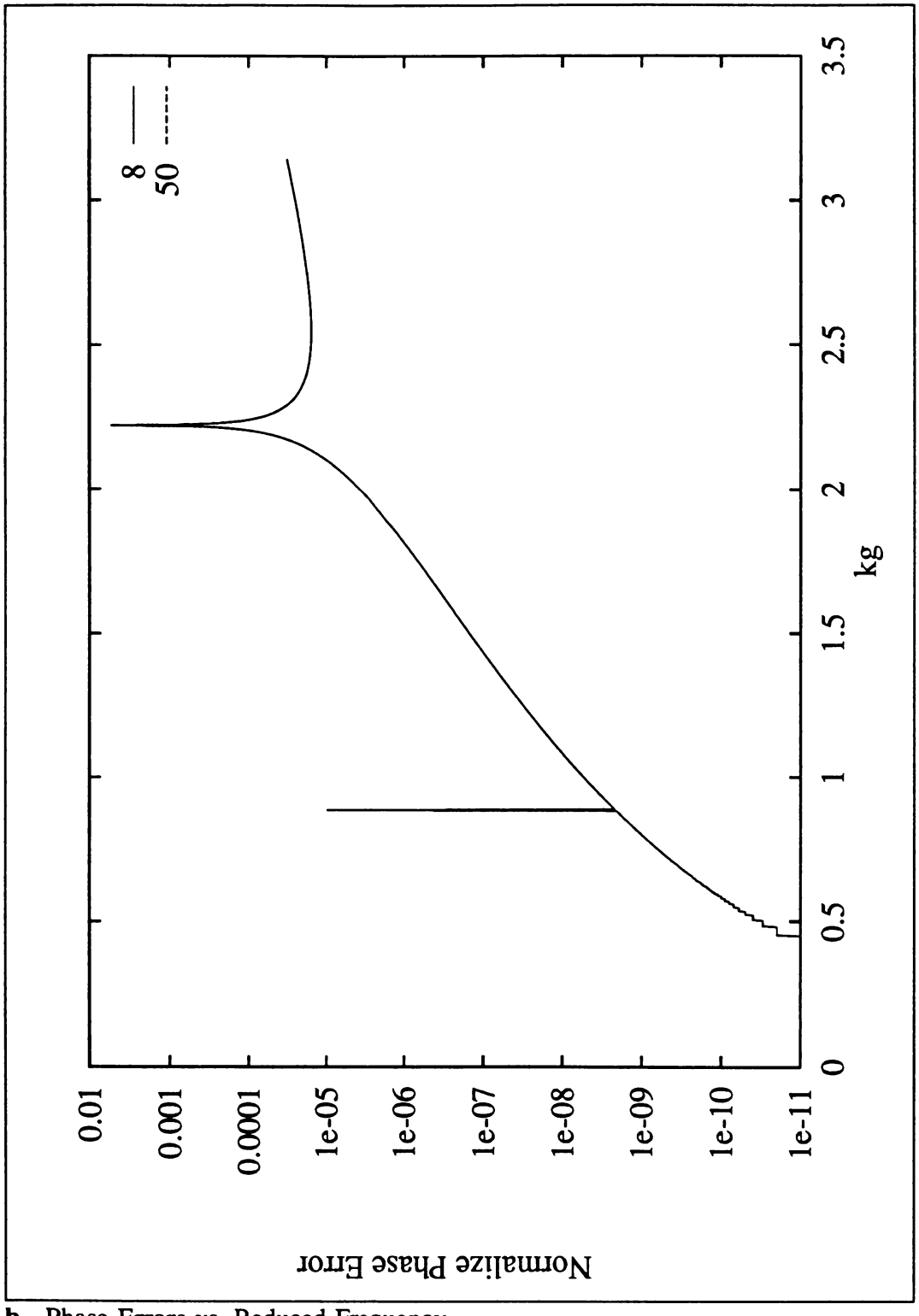

b. Phase Errors vs. Reduced Frequency

Figure 3.2.1.2. (continued)

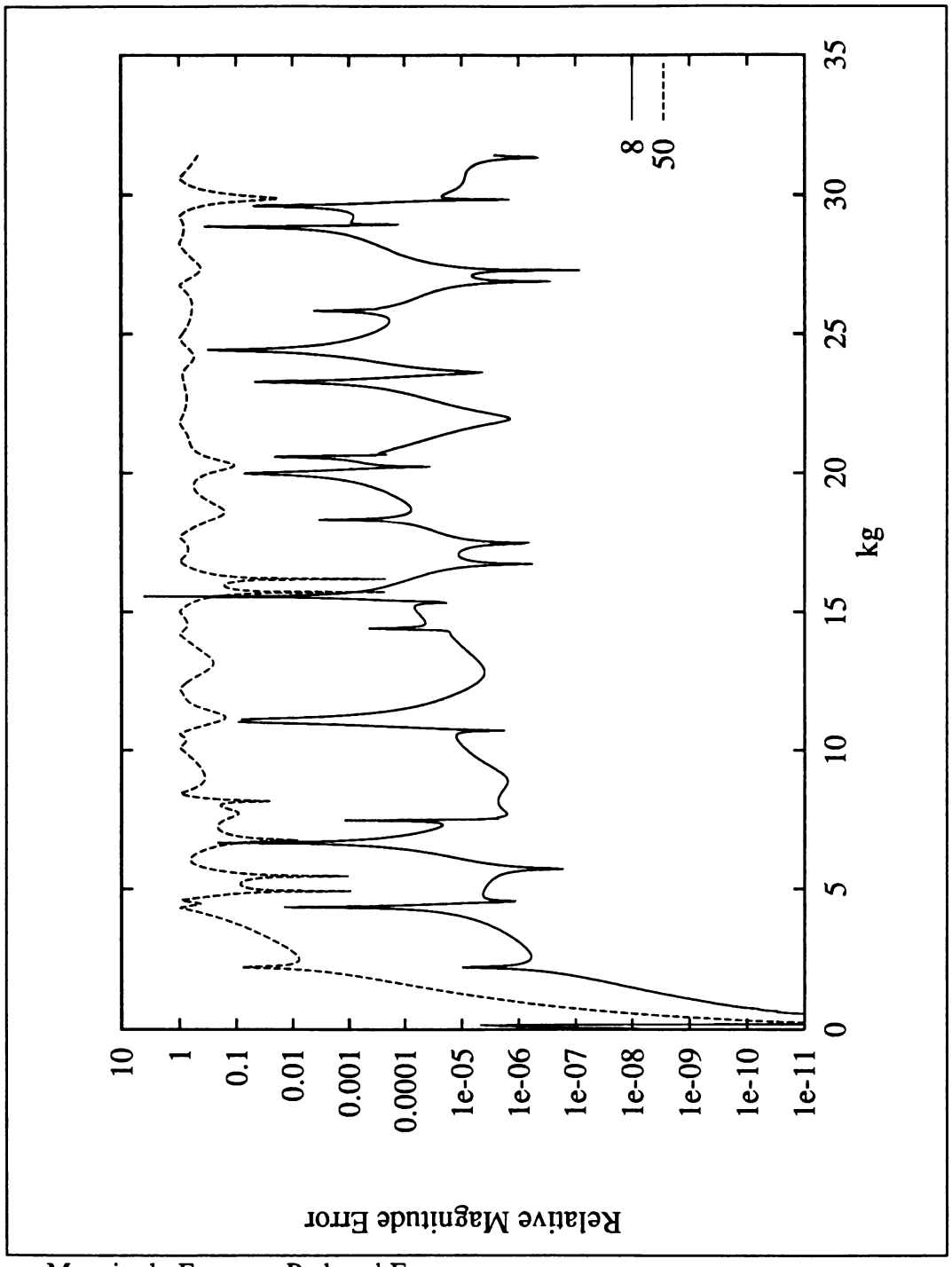

a. Magnitude Error vs. Reduced Freq.

Figure 3.2.1.3. Demonstration of Smaller Error for 8 Hypothetical Sources with Wave Approaching from 0°; 50 Hypothetical Sources Included for Comparison; k_g from 0 to 10

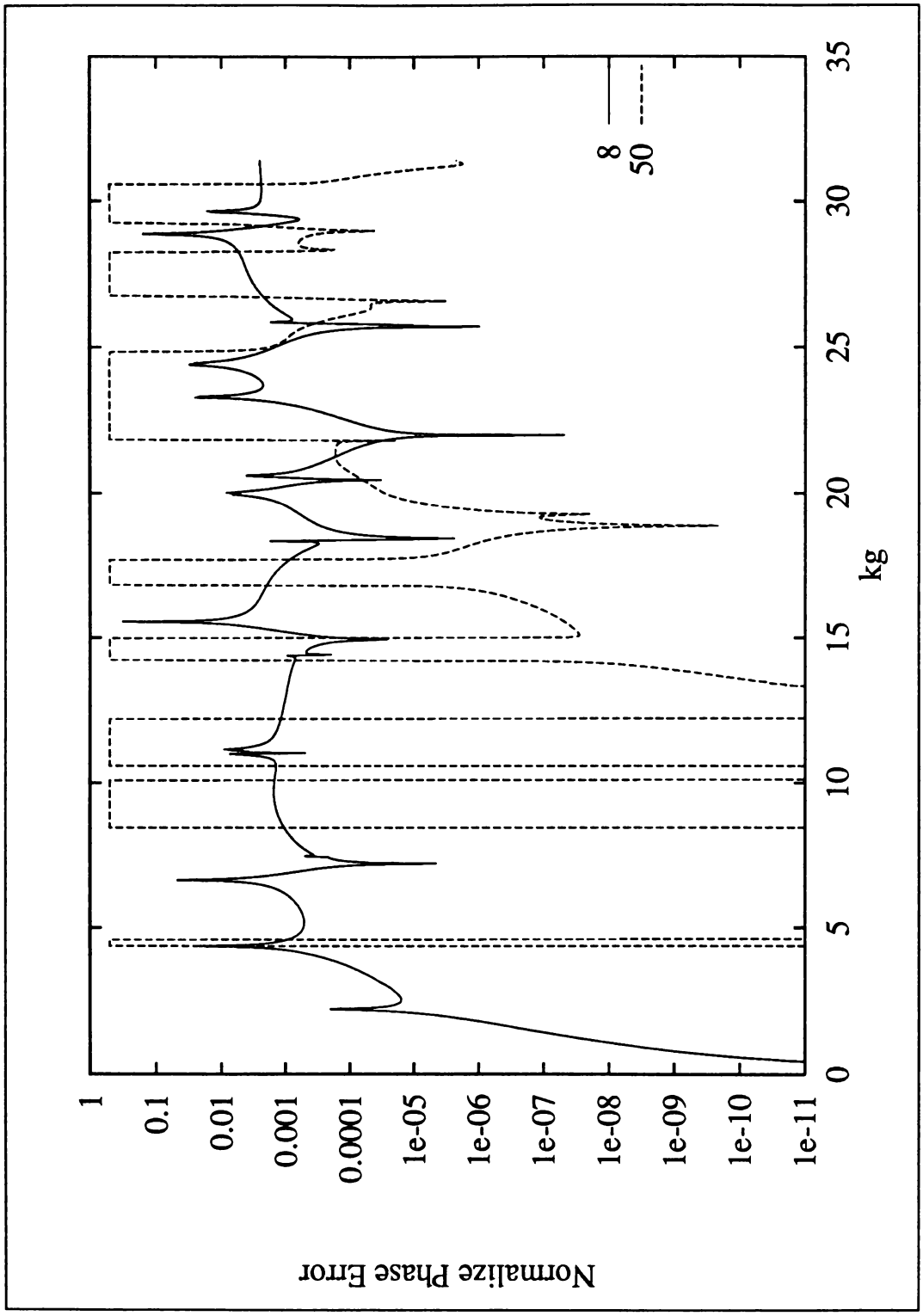

b. Phase Error vs. Reduced Freq.

Figure 3.2.1.3. (continued)

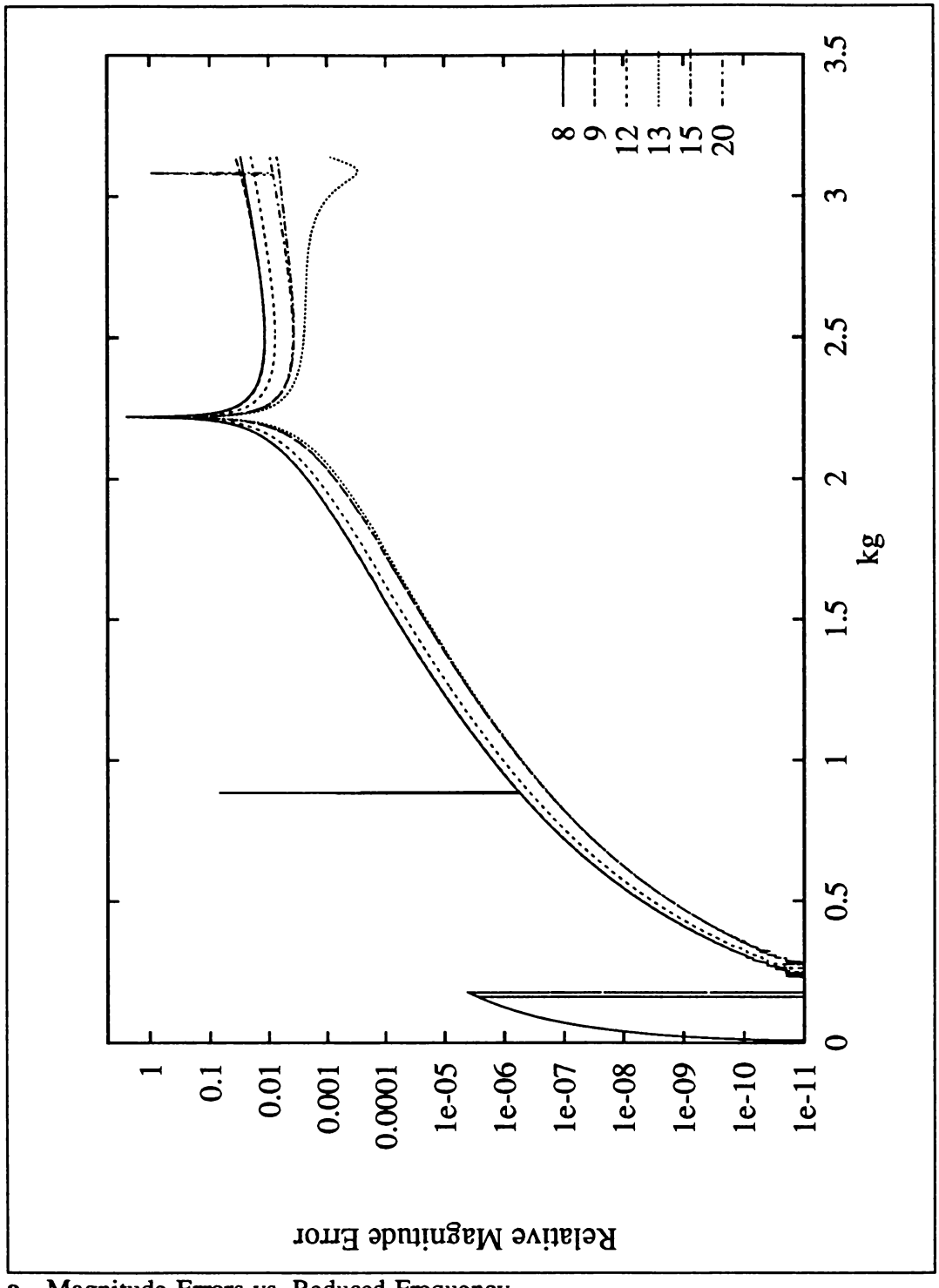

a. Magnitude Errors vs. Reduced Frequency

Figure 3.2.1.4. Effect of Number of Hypothetical Sources: # HS = 8, 9, 12, 13, 15, 20

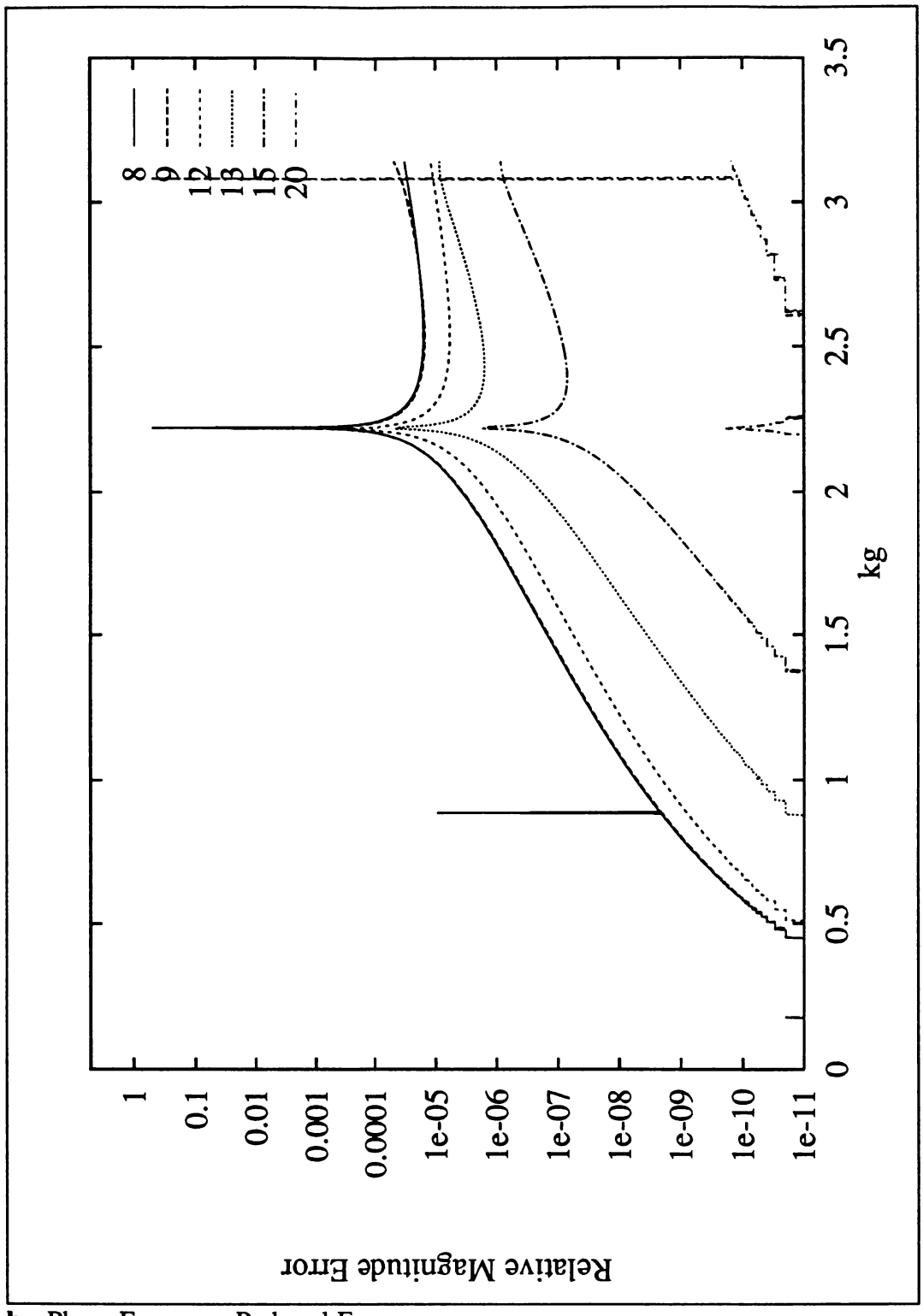

b. Phase Errors vs. Reduced Frequency

Figure 3.2.1.4. (continued)

3.2.2 Distribution of Hypothetical Source Strengths

This section examines how the hypothetical source strengths vary for different numbers of hypothetical points, angles the plane wave approaches from, and reduced frequencies. For this section, the standard case is used (section 3.1.1), except the hypothetical source strength distributions are computed for 8, 20, 50 and 200 sources, with k_s = 0.25, 1, and 1.75. The angles the wave approaches from are 0° and 22.5°.

The hypothetical source strength distributions verify hypotheses and provide some further insight. As we expected, the distribution has a large lobe in the direction of the oncoming wave (see figs. 3.2.2.1-6). However, unexpected smaller lobes appear pointed in different directions, counteracting and seemingly balancing the effects of the larger lobe. This is probably a result of SVD's least-norm behavior.

When the oncoming plane wave's angle is 0°, the number of lobes generated is eight. Note that when the angle is changed to 22.5°, the lobes rotate the same 22.5°, and reduce in number to six. Approaching 45°, the number of lobes once again become eight.

For an angle of 0° with eight sources, a long lobe pointed in the x direction is hidden by the x axis (figs. 3.2.2.1-3a). This is a result of the symmetry of the incoming wave with the position of the computed and local nodes, hypothetical sources and the oncoming wave. However, when the angle is tilted to 22.5°, the source strengths are more dispersed (figs. 3.2.2.4-6a).

To normalize the lobes so they are be relatively similar in size, the magnitudes are multiplied by a scaling factor, $\frac{[\#\ hypothetical\ sources]}{\sqrt{k\ [HS\ Radius]}}$ (see figs. 3.2.2.1-6e).

For further lobe studies involving different numbers of local nodes, see Appendix 4.

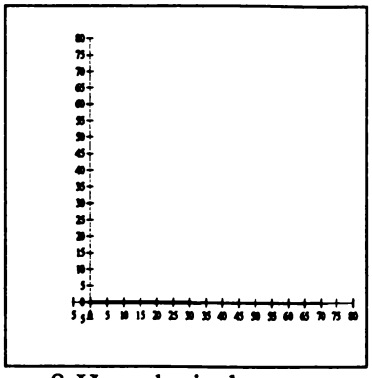

a. 8 Hypothetical sources

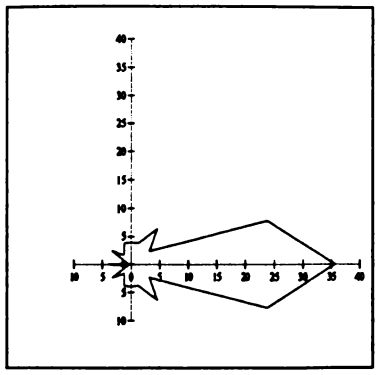

b. 20 Hypothetical sources

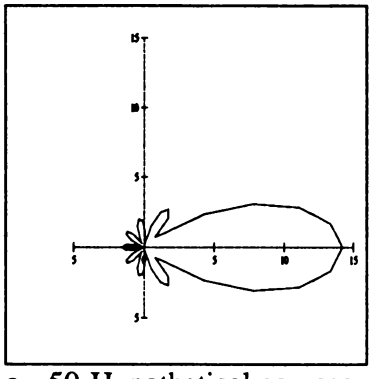

c. 50 Hypothetical sources

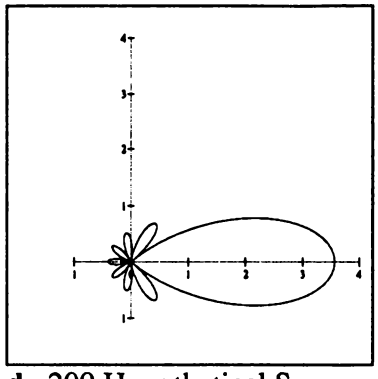

d. 200 Hypothetical Sources

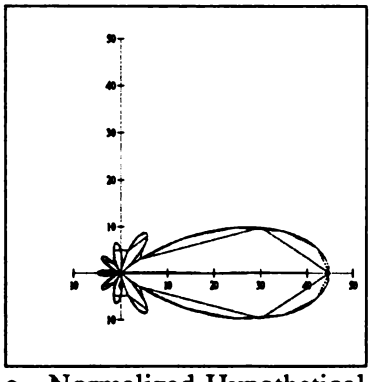

e. Normalized Hypothetical source strength distributions

Figure 3.2.2.1. Hypothetical source strength plots for different numbers of hypothetical sources: k = 0.25, plane wave approaches from an angle of 0° from the right

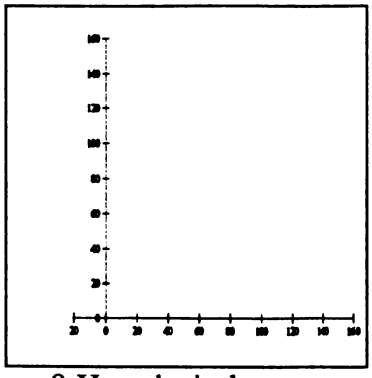

a. 8 Hypothetical sources

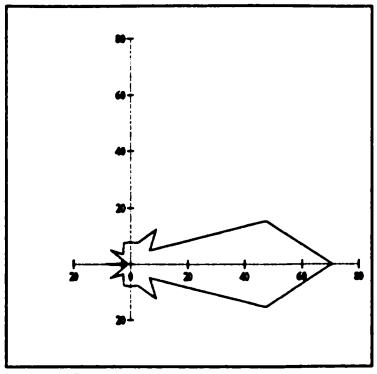

b. 20 Hypothetical sources

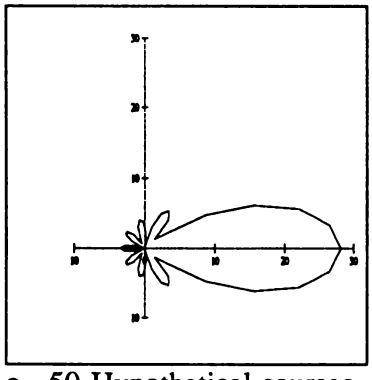

c. 50 Hypothetical sources

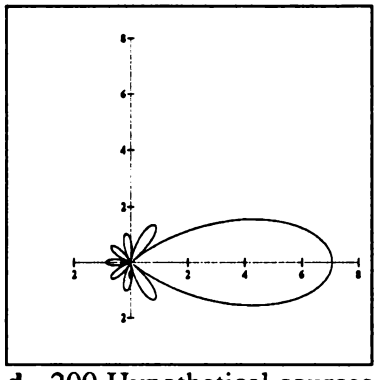

d. 200 Hypothetical sources

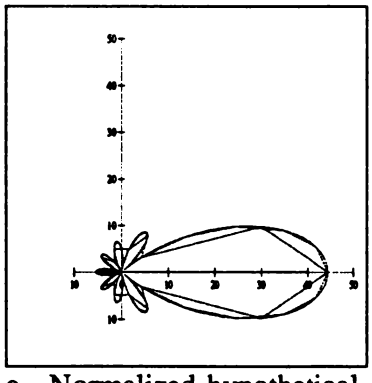

e. Normalized hypothetical source strength distributions

Figure 3.2.2.2. Hypothetical source strength plots for different numbers of hypothetical sources: k = 1.0, plane wave approaches from an angle of 0° from the right

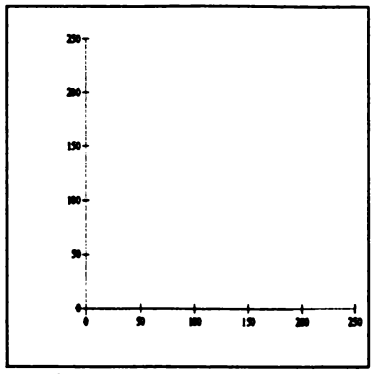

a. 8 Hypothetical sources

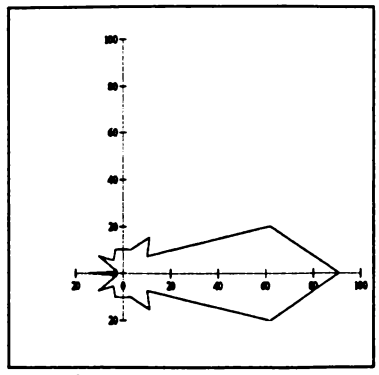

b. 20 Hypothetical sources

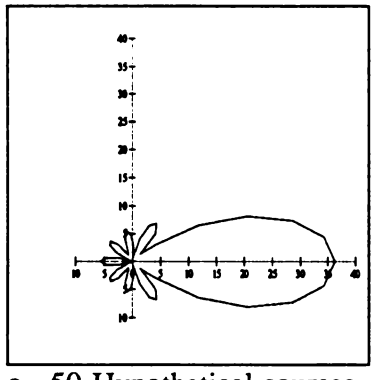

c. 50 Hypothetical sources

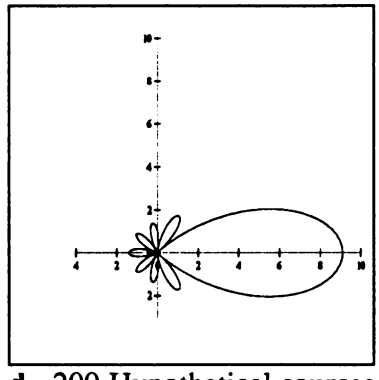

d. 200 Hypothetical sources

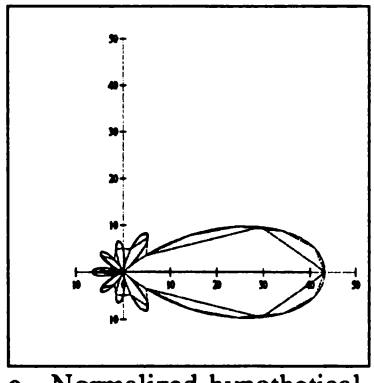

e. Normalized hypothetical source strength distributions

Figure 3.2.2.3. Hypothetical source strength plots for different numbers of hypothetical sources: k = 1.75, plane wave approaches from an angle of 0° from the right

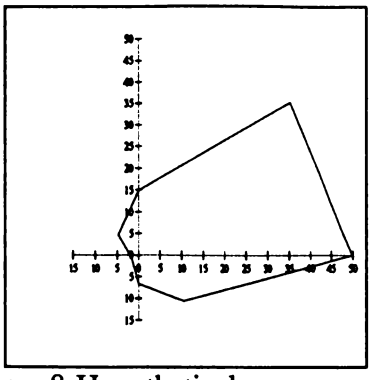

a. 8 Hypothetical sources

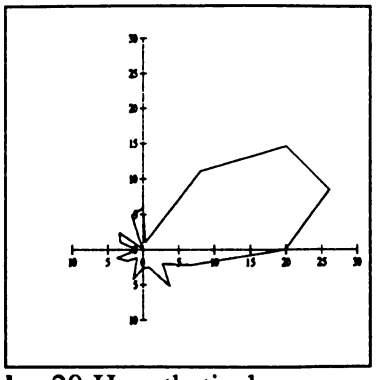

b. 20 Hypothetical sources

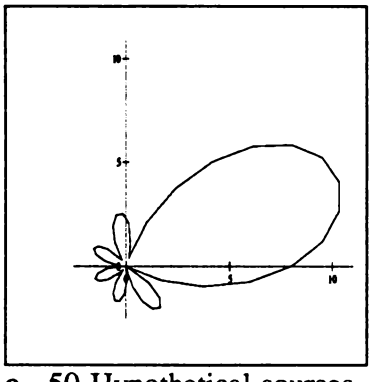

c. 50 Hypothetical sources

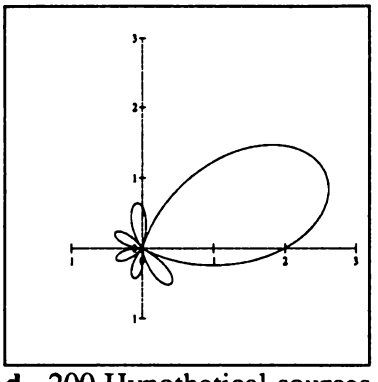

d. 200 Hypothetical sources

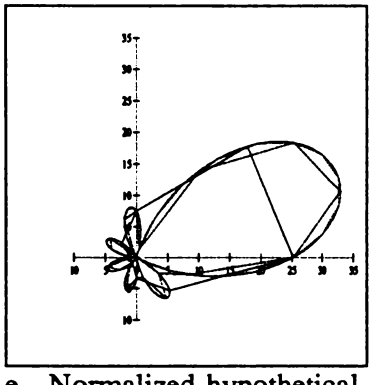

e. Normalized hypothetical source strength distributions

Figure 3.2.2.4. Hypothetical source strength plots for different numbers of hypothetical sources: k = 0.25, plane wave approaches from an angle of 22.5° from the right

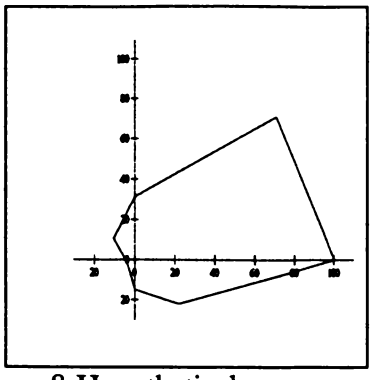

a. 8 Hypothetical sources

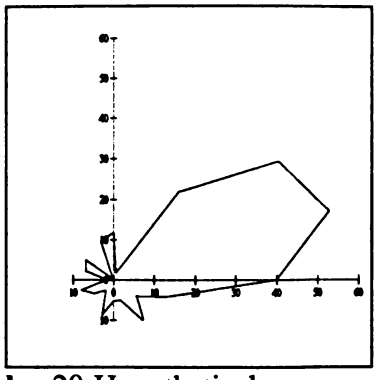

b. 20 Hypothetical sources

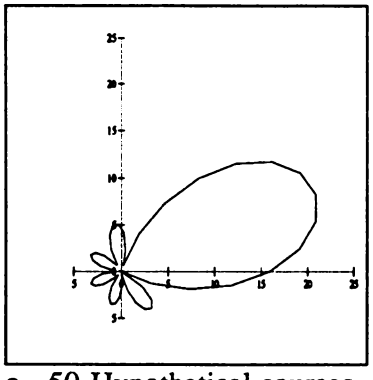

c. 50 Hypothetical sources

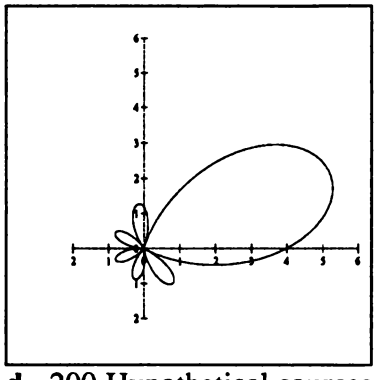

d. 200 Hypothetical sources

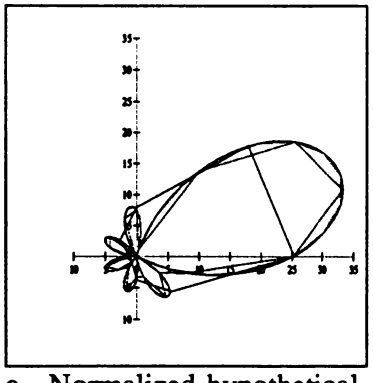

e. Normalized hypothetical source strength distributions

Figure 3.2.2.5. Hypothetical source strength plots for different numbers of hypothetical sources: k = 1.0, plane wave approaches from an angle of 22.5° from the right

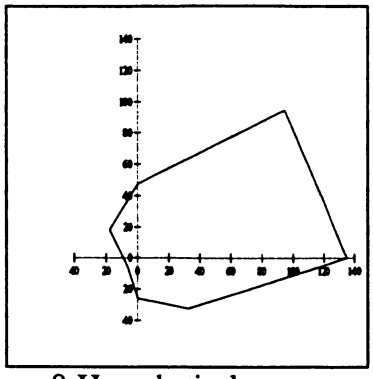

a. 8 Hypothetical sources

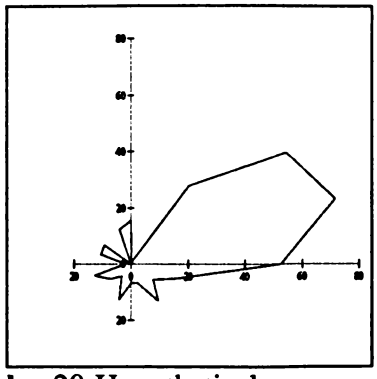

b. 20 Hypothetical sources

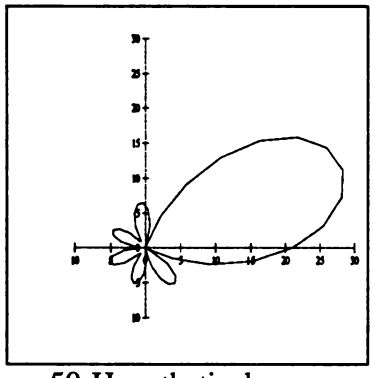

c. 50 Hypothetical sources

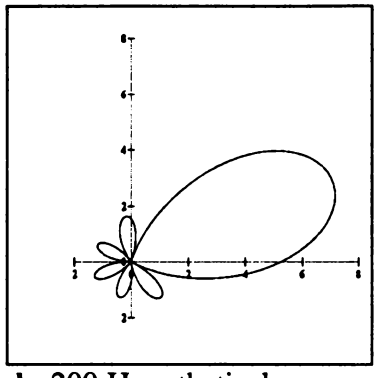

d. 200 Hypothetical sources

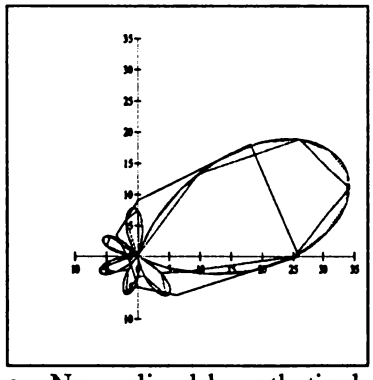

e. Normalized hypothetical source strength distributions

Figure 3.2.2.6. Hypothetical source strength plots for different numbers of hypothetical sources: k = 1.75, plane wave approaches from an angle of 22.5° from the right

3.2.3 Hypothetical Source Radius

This section shows that varying the hypothetical source radius does not affect the accuracy of the solution. For this section, hypothetical source radii of 10, 100 and 1000 are used, normalized by $L_g = 1$. Figure 3.2.3.1 shows that the magnitude errors are the same for the chosen radii (when 50 hypothetical sources are used, the phase error is negligible). However, as the radius increases, random problems with singular values decrease. In figure 3.2.3.1, the cases for HS radii = 100 and 1000 have a discontinuity at $k_g = 0.2$, where the number of singular values increases and the solution improves. The discontinuity at $k_g = 0.2$ is dashed because for HS radius = 10 all of the singular values were used everywhere.

The HS radius does affect the magnitude of the hypothetical sources. As the HS radius increases, the hypothetical sources must be louder to compensate, and the amplitude of the sound increases by $\sqrt{HS\ radius}$ for 2-D (for large r). The hypothetical source strengths (figures 3.2.3.2a-c) are normalized by $\frac{[\#\ hypothetical\ sources]}{\sqrt{k\ [HS\ radius]}}$ in figure 3.2.3.2d, showing the similarity of the strengths. The slightly different shape for the HS radius = 10 case may be due to a change in the "scattering" pattern due to the smaller value of (k_g x HS radius). For plane waves, the source strength patterns can be very different if the product of the reduced frequency and the HS radius (k_g x HS radius) < 50. The patterns are similar to patterns created by acoustic scattering from a cylinder ([12], p. 420).

If (k_g x HS radius) is held constant, and no other parameters are varied, similar (but <u>not</u> identical) hypothetical source strength distributions are generated. This is due to the fact that these different situations have only similar vectors to the hypothetical sources, and when the hypothetical source radius changes, the local nodes' distances to

the hypothetical sources vary non-linearly. Therefore, if a grid is discretized for a particular reduced frequency, the same discretization cannot be used for a different reduced frequency by holding (k_s x HS radius) constant, and changing the HS radius.

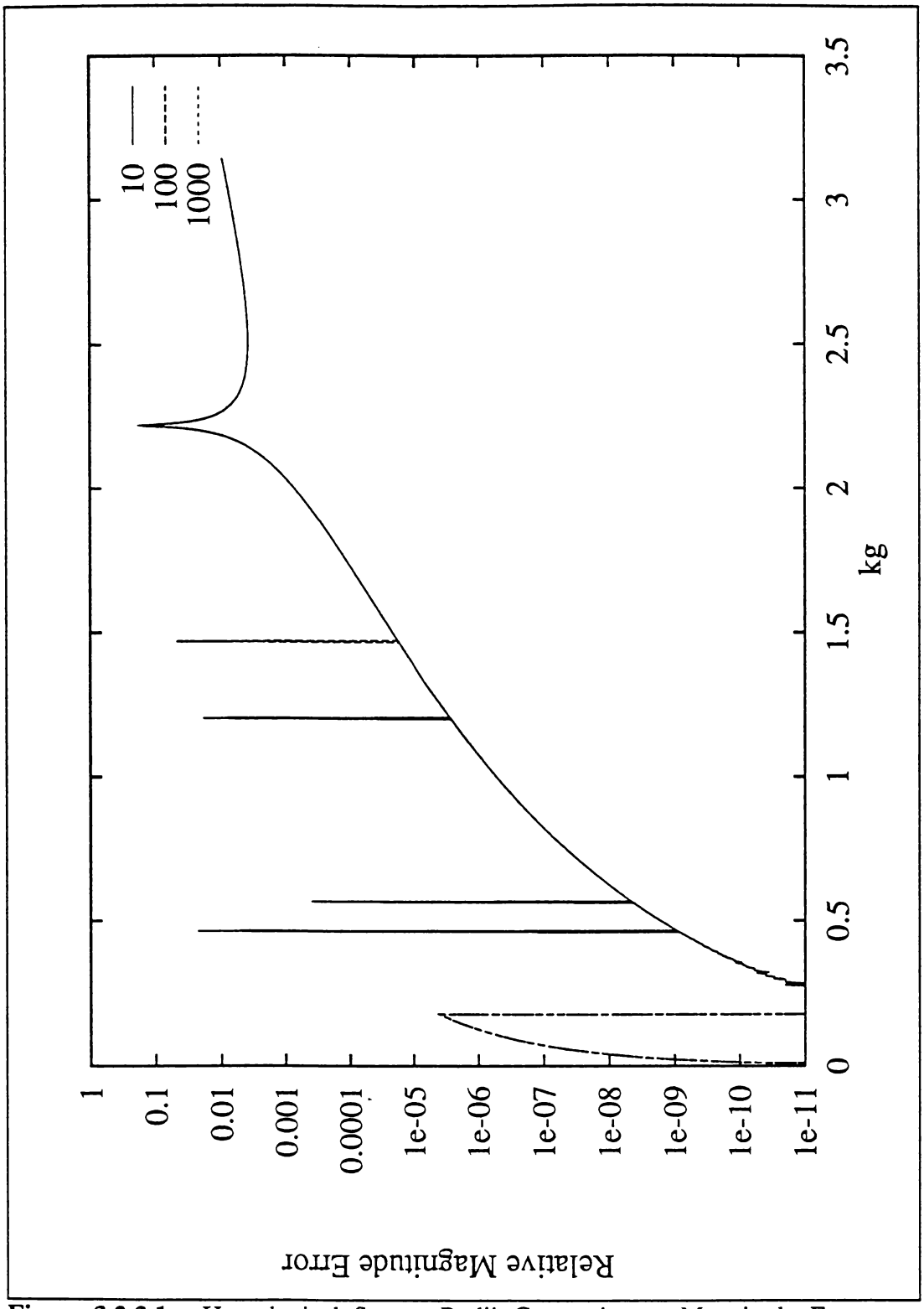

Figure 3.2.3.1. Hypothetical Source Radii Comparison: Magnitude Errors vs. Reduced Frequency

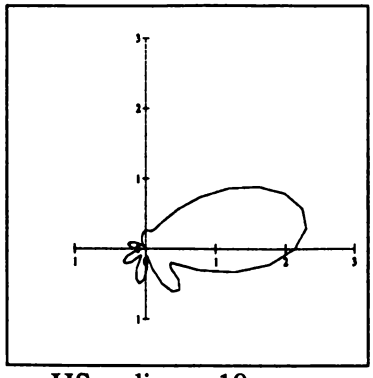

a. HS radius = 10

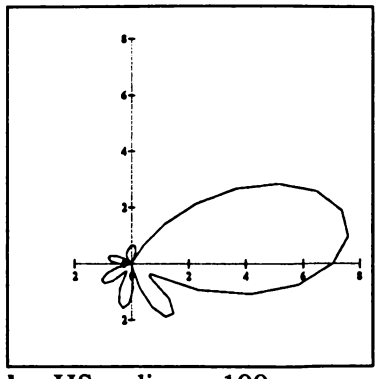

b. HS radius = 100

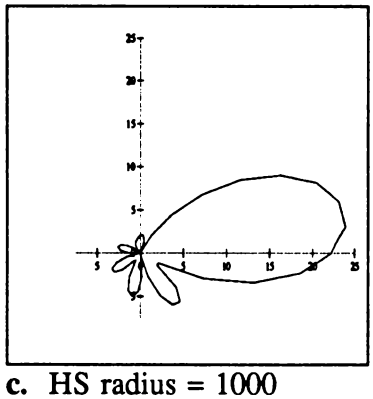

c. HS radius = 1000

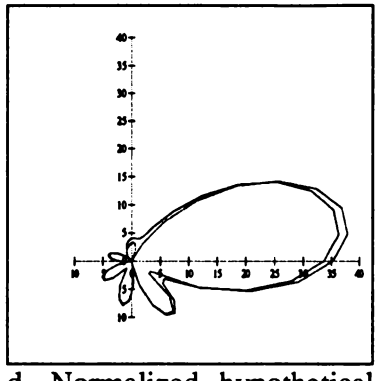

d. Normalized hypothetical source point distributions

Figure 3.2.3.2. Hypothetical source strength distributions for varying HS radii. Figure 4.2.3.1d demonstrates the source strength normalized by [# hypothetical sources] / $\sqrt{k\ [HS\ Radius]}$.

3.3 Pseudo-Inverse Calculation Study

3.3.1 Singular Value Truncation

This pseudo-inverse section shows how the errors in the solution change when different numbers of singular values are truncated (see section 2.4). Solutions are sought for both singular and double precision calculations of magnitude and phase error versus the reduced frequency (k_g), as well as the number of singular values used versus the reduced frequency.

The number of singular values used in each calculation is determined by the comparison of each singular value to the largest singular value. The SVD routine orders the values from highest to lowest in an array. To compare the values, multipliers are implemented. If a singular value multiplied by the multiplier is less than the largest singular value (the value in the first position of the array from the SVD routine), that value and the values following it are not used in the calculations. For example, if the singular value array is [84312, 532, 23, 3], and the multiplier is 1000:

$$532 \times 1000 = 532000 > 84312$$

and 532 is used, but

$$23 \times 1000 = 23000 < 84312$$

so 23 and all of the singular values after it are not used in the computation. Multipliers of 10, 100, 1000, 10000, 100000 and 10^{17} are used (10^{17} results in all of the singular values being used).

The effects of eliminating too many or too few singular values are evident from the graphs. If too many singular values are eliminated (for example, a multiplier of 10), the solution is not accurate. If no singular values are eliminated, errors appear near $k_g = 0$. The inclusion or exclusion of singular values appear as discontinuities along the

magnitude error plot (fig. 3.3.1.1). It is interesting to note that the cusp at $k_g = 2.221$ is "skipped" if enough singular values are dropped. While eliminating singular values reduces the discretization time, loss of accuracy makes doing so undesirable.

For reduced frequencies less than from 0.1, the HSM develops errors unless some singular values are dropped (the relative error was on the order of 10^{-7}, see figs. 3.3.1.1). From figure 3.3.1.1, one can see that even for some very large multipliers, near a reduced frequency (k_g) of 0 some singular values are so small that even when multiplied by 100,000 they are still smaller than the largest singular value. Unless these singular values are eliminated, they can cause problems when the singular value matrix is inverted. The very small singular value takes on a very large value when the singular value matrix is inverted. If a small singular value has few significant digits, the problem is intensified. This may be due to the fact that the current code uses Bessel functions which are built into the compiler, and may not be accurate at low frequencies. Also, the error could be due to the Green's function used: as the reduced frequency approaches zero, the Neumann portion of the Hankel function (Y_0) approaches infinity.

The speed and accuracy of the solution can also be a function of the number of significant digits available on the computer. This can be simulated by using single and double precision. Single precision has six significant digits. Since the matrices used are generally unstable, the solution is sensitive to computational truncation problems, which become pronounced about $k_g = 0$ (see figs. 3.3.1.2a-b). Double precision solutions maintain their stability everywhere except for a smaller region near $k_g = 0$. Since the single and double precision computations are essentially the same computations with different significant values, it is not surprising that the reduced frequencies where the singular values are truncated are identical.

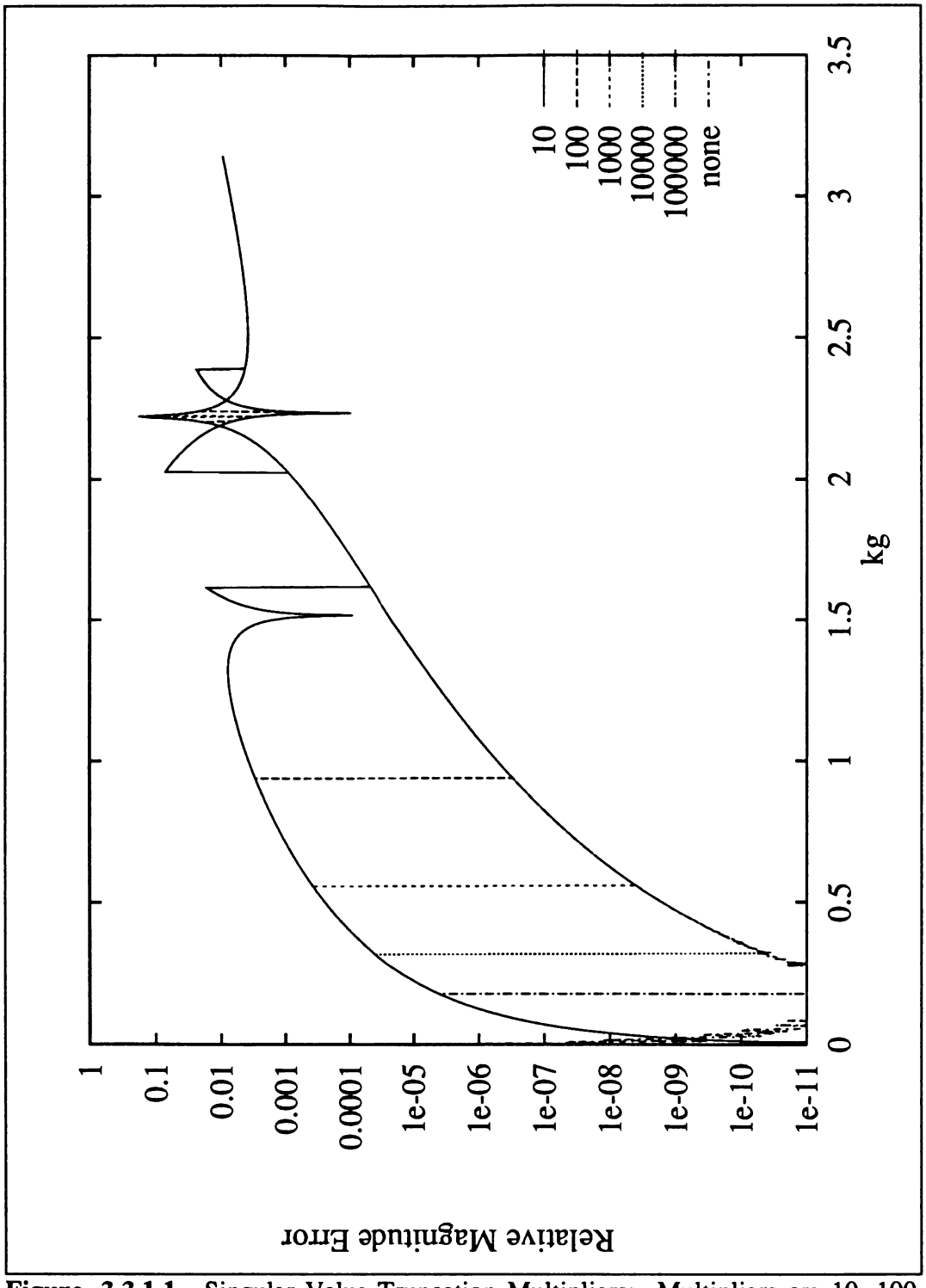

Figure. 3.3.1.1. Singular Value Truncation Multipliers: Multipliers are 10, 100, 1000, 10000, 100000 and 10^{17}; Double Precision; Magnitude Errors vs. Reduced Frequency

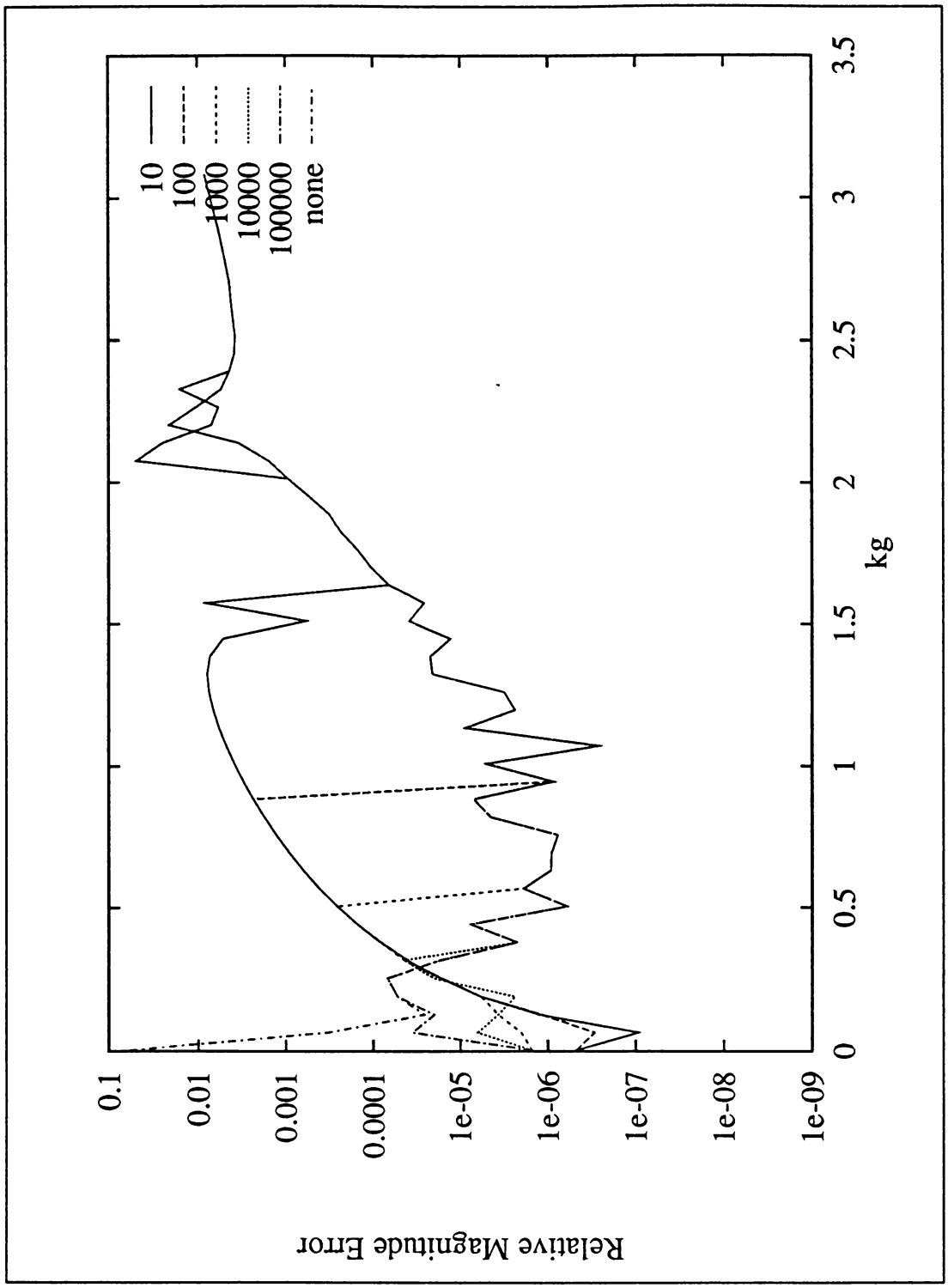

a. Magnitude Errors vs. Reduced Frequency

Figure 3.3.1.2. Singular Value Truncation Multipliers: Multipliers are 10, 100, 1000, 10000, 100000 and 10^{17}; Single Precision

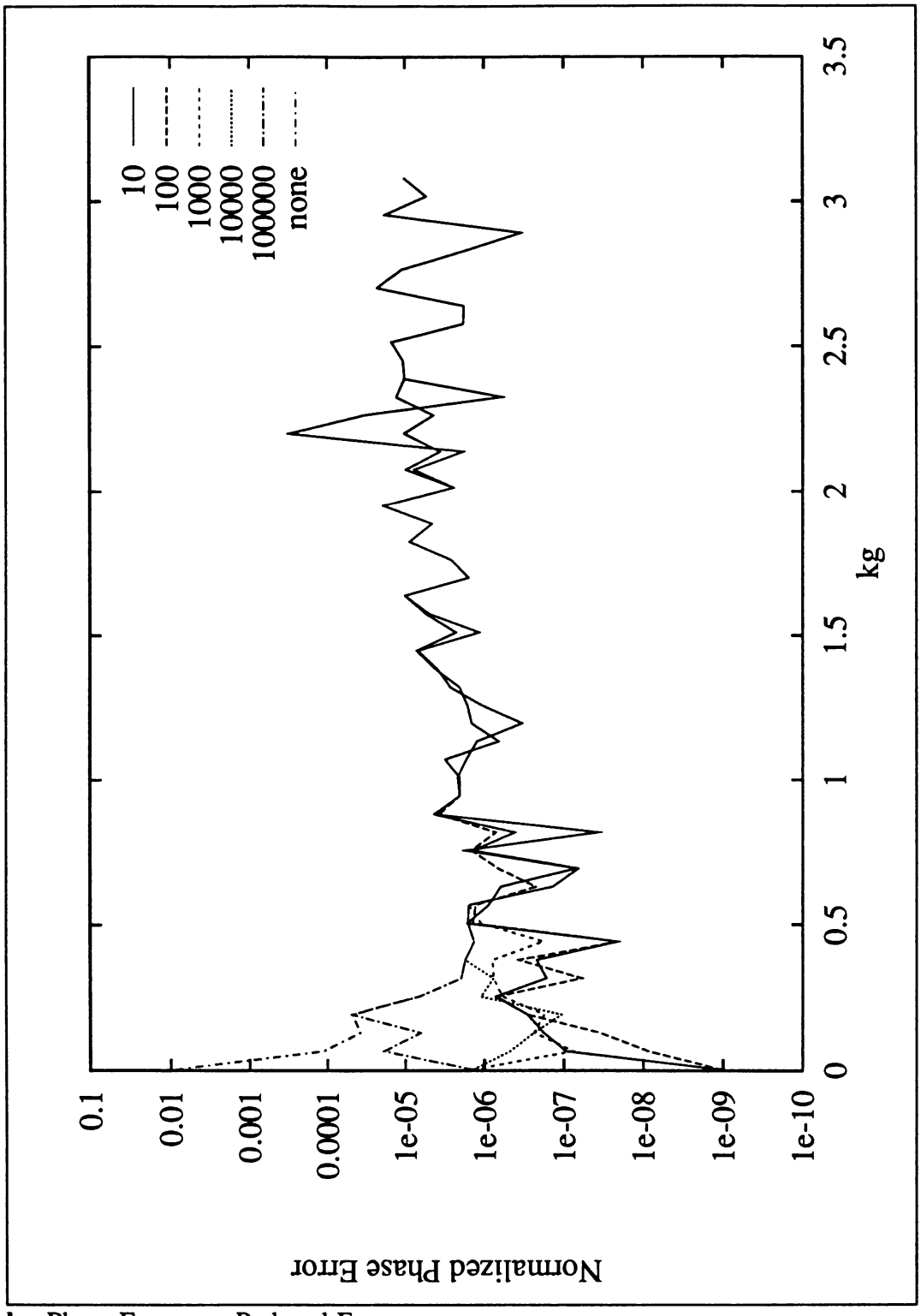

b. Phase Errors vs. Reduced Frequency

Figure 3.3.1.2. (continued)

3.3.2 Number of Singular Values

This section examines how the number of singular values affects the accuracy of the solution. The maximum number of singular values that can be used equals the number of local nodes in the discretization. The actual number of singular values used will be smaller if some are chosen for truncation (section 3.3.1). To vary the number of local nodes, "n-gon" stencils are used, in which the local nodes are placed on a unit circle, with the computed node at the center (fig. 3.3.2.1.a).

The geometries tested are n-gons (n = 4 to 10) and the square (the square has 8 singular values). The quadrilateral has unusual divergence characteristics, having a more accurate magnitude cusp at $k_g = 2.221$. However, with 4 local nodes, by this time this reduced frequency is reached the solution is already poor, so to reduce the number of lines per plot the quadrilateral and square results are plotted together. In summary, n-gons 5 to 10 are included on one set of plots, and the quadrilateral and the square are put together in another set. The n-gons use k_g, with the length parameter $L_g = 1$, the radius of the local nodes to the computed node. The quadrilateral and square use a length parameter k_d.

Figures 3.3.2.2abc show that an asymmetric geometry (odd n-gon) can have smaller magnitude errors than a grid with an extra node and a symmetric geometry. The symmetric (even n-gon) geometries have negligible phase errors, while the non-symmetric grids have errors similar to the magnitude errors.

These grids are then used to compute magnitude and phase error versus angle plots (with the angle varying from 0° to 45°, $k_g = 2$). The errors are periodic in nature (see figs. 3.3.2.3abc) The grids have one node to the right of the computed node, parallel to the x-axis, so the periodic nature is centered about 0°. The errors have broad ranges of angles where the solution is the least accurate, and cusps where the error becomes very small for a small range of angles. The relative magnitude errors for even n-gons have

their highest errors along axis and bisector angles (see fig. 3.3.2.1b). The cusps are located in between the axis and the bisector angles. The odd n-gons have just the opposite results: the cusps are located periodically along the axes and the bisectors, and the large errors are found in between these angles. In general, the odd number of local nodes return more accurate magnitude results. However, when the phase error plots are examined, the even n-gons have exact phase results, while the odd n-gons' phase errors have the same behavior as the even n-gon magnitudes. The quadrilateral and square have the same behavior as the even n-gons.

When these error vs. angle plots are compared with the hypothetical source strength plots in Appendix 4, the regions where the even n-gons have the least magnitude accuracy are where the hypothetical source distribution is symmetric. The odd hypothetical source distributions never lose any lobes nor do they lose their symmetry for any incoming angle; however, they do vary in that the lobes do not all meet at the origin for angles in between axes and bisectors. The least accurate magnitude errors and most accurate phase errors occur when the angle is between the axes and the bisectors. This implies that the shape of the hypothetical source distribution (due to the direction of the incoming wave) does affect the solution accuracy.

This information reveals the angle that produces the largest error for the different geometries. In this manner the error vs. k plots (figs. 3.3.2.4a-c) can represent the least accurate solution for a plane wave as they have the wave approach with the worst possible oncoming angle. One difficulty presented by the standard setup is that an angle of 15° is used. This poses no problem for most of the cases, but it can make the hexagon stencil become two magnitudes better in accuracy because 15° is a more accurate magnitude cusp in this case (as seen in fig. 3.3.2.3a). The odd n-gons are much more accurate than the even n-gons, but the even n-gons still show no phase error for one plane wave.

Again, it is interesting to note that for the n-gons five and higher, the magnitude errors are all grouped about $k_g = k_d = 2.405$ ($L_d = L_g = 1$ for n-gons). This is attributable to the first zero of the Bessel function J_0 (see section 2.5).

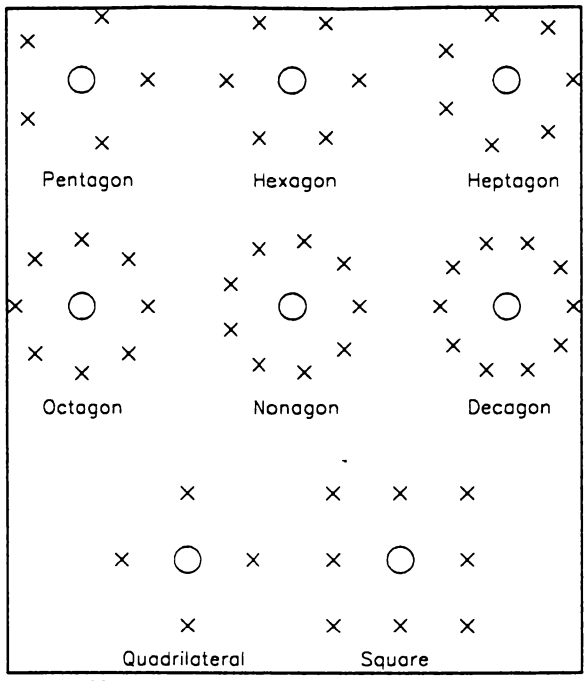

a. Different grids used in computations

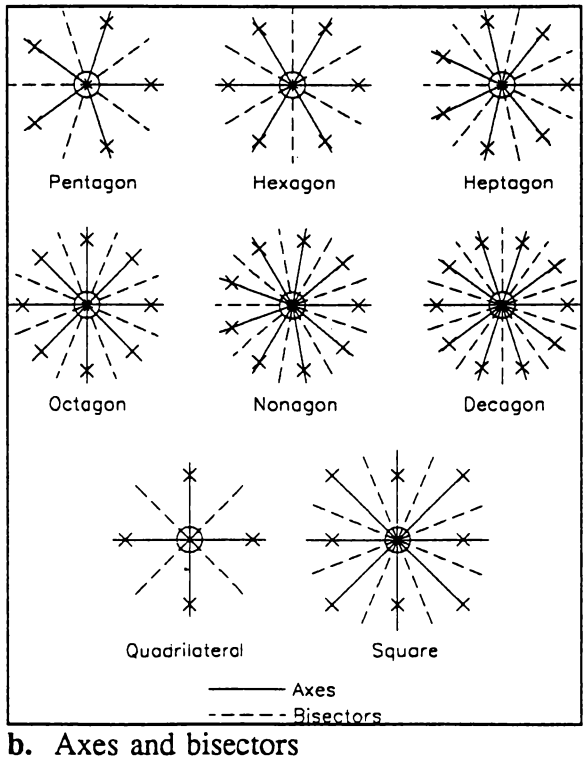

b. Axes and bisectors

Figure 3.3.2.1. Grids that are used for differing numbers of local nodes in computations, and the axes and bisectors waves can be aligned with

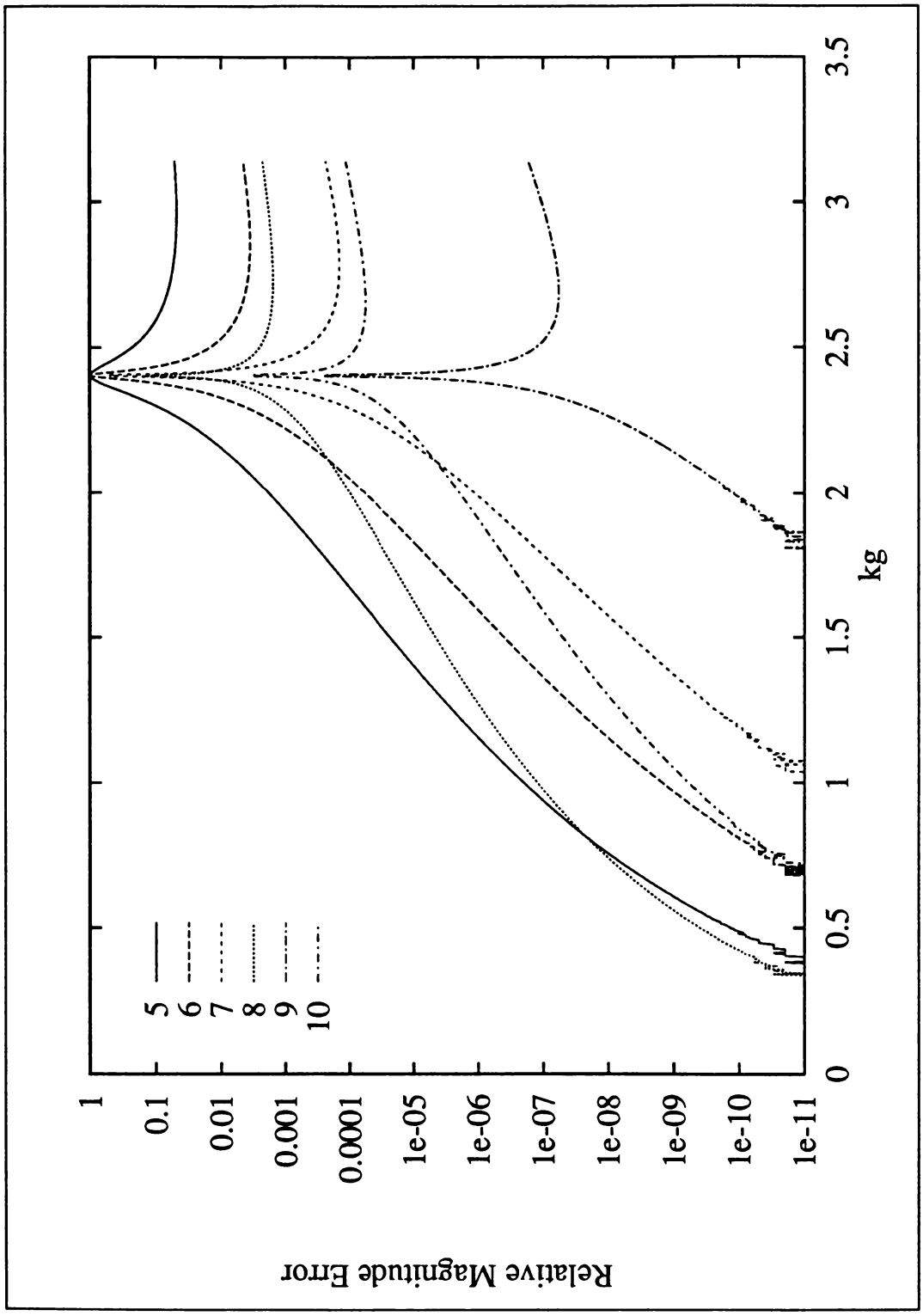

a. 5-10 Local Nodes (n-gon geometry), Magnitude Errors vs. Reduced Frequency

Figure 3.3.2.2. Varying Number of Local Nodes (4-10)

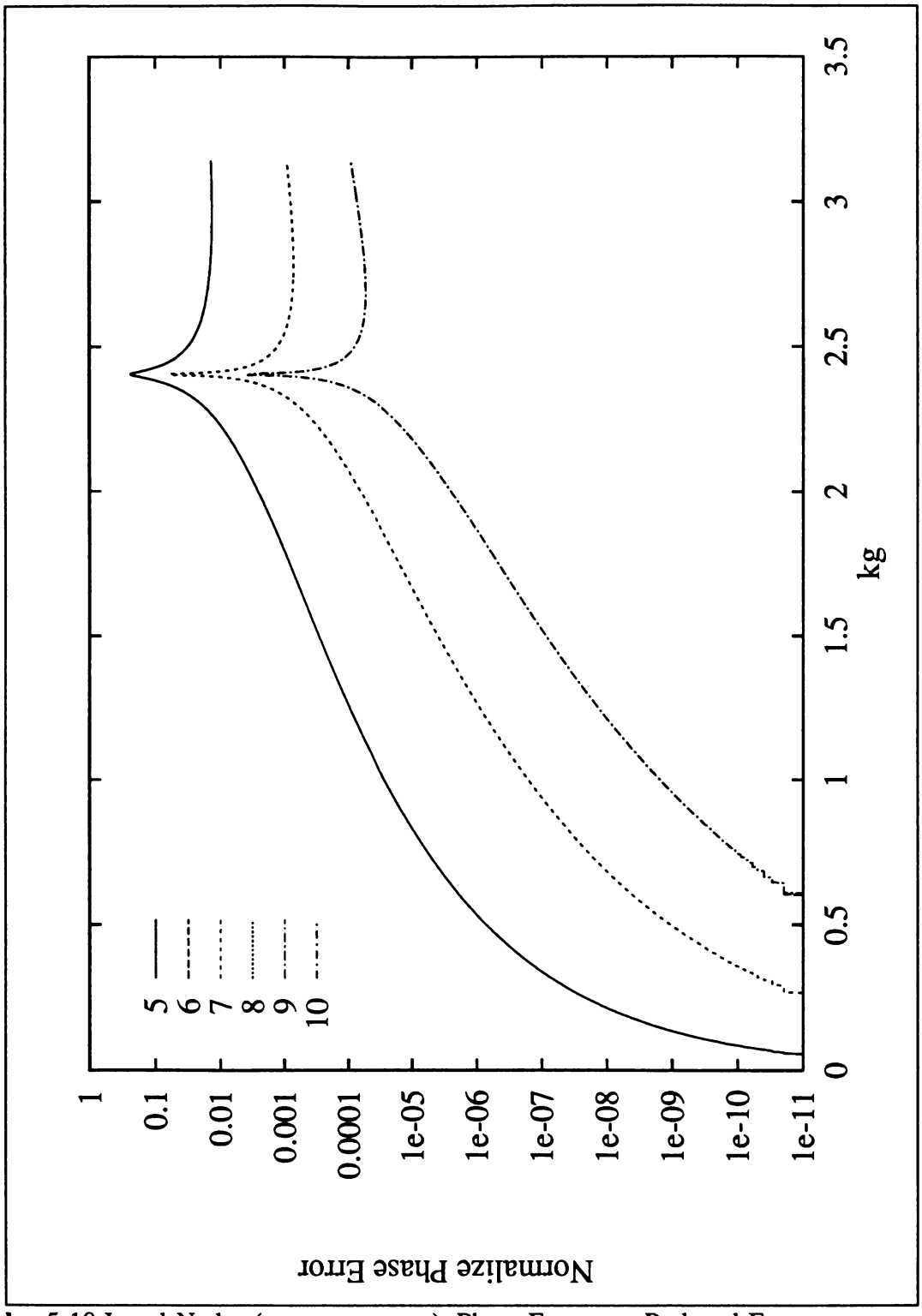

b. 5-10 Local Nodes (n-gon geometry), Phase Errors vs. Reduced Frequency

Figure 3.3.2.2. (continued)

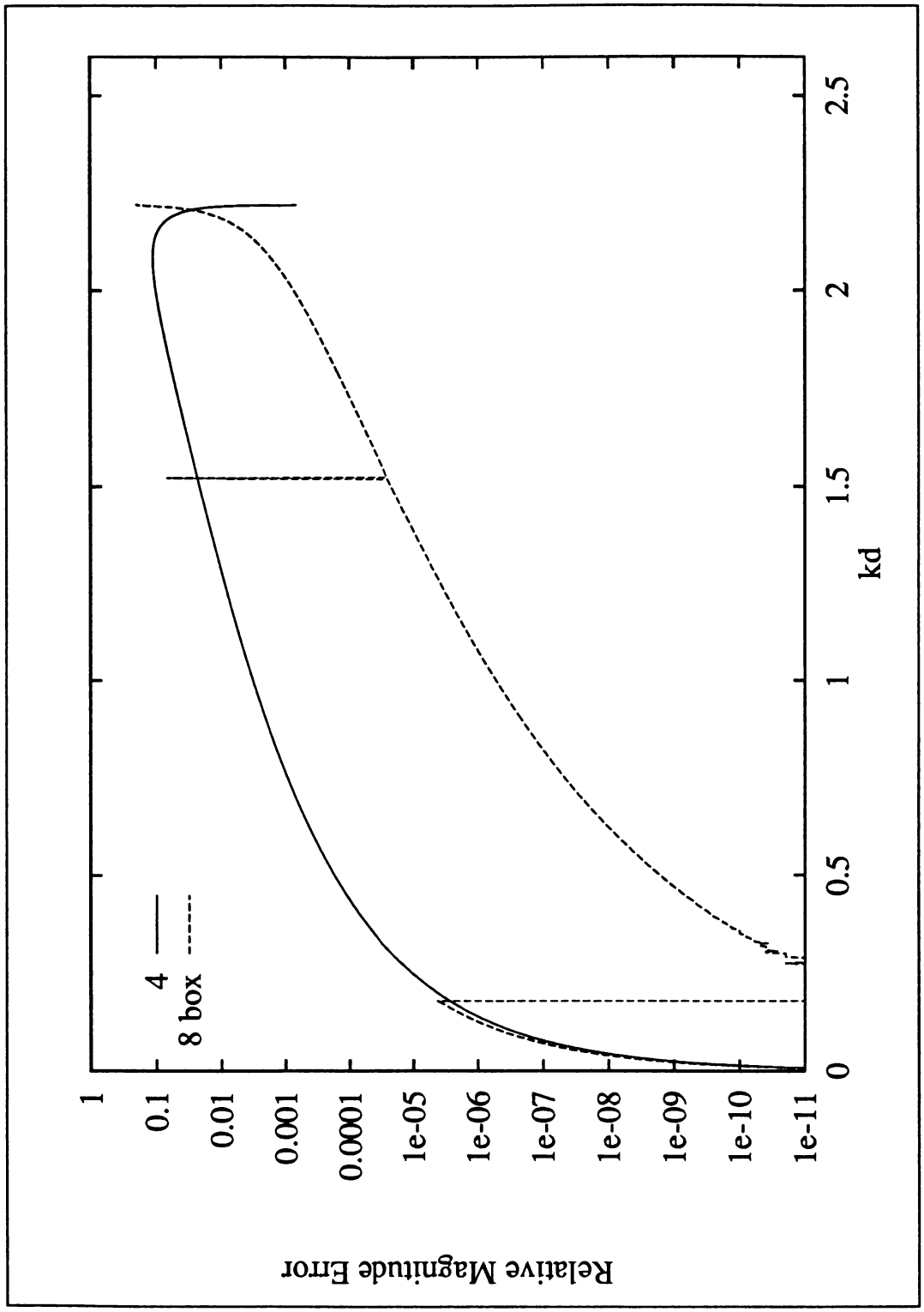

c. Quadrilateral and 3x3 box Local Nodes, Magnitude Error vs. Reduced Frequency

Figure 3.3.2.2. (continued)

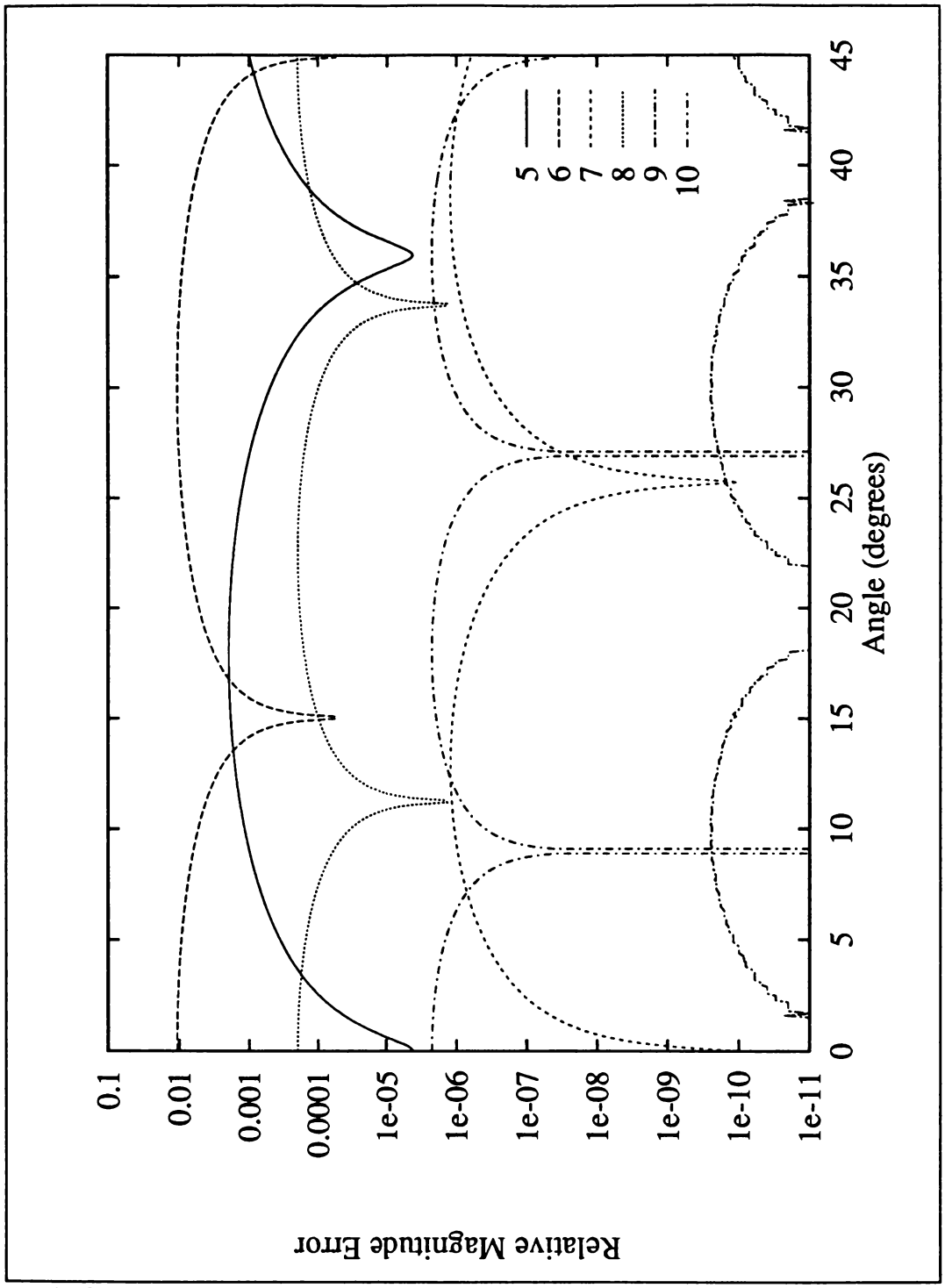

a. 5-10 Local Nodes (n-gon geometry), Magnitude Errors vs. Angles

Figure 3.3.2.3. Varying Plane Wave Angle Relative to Grid for Different No. of Local Nodes

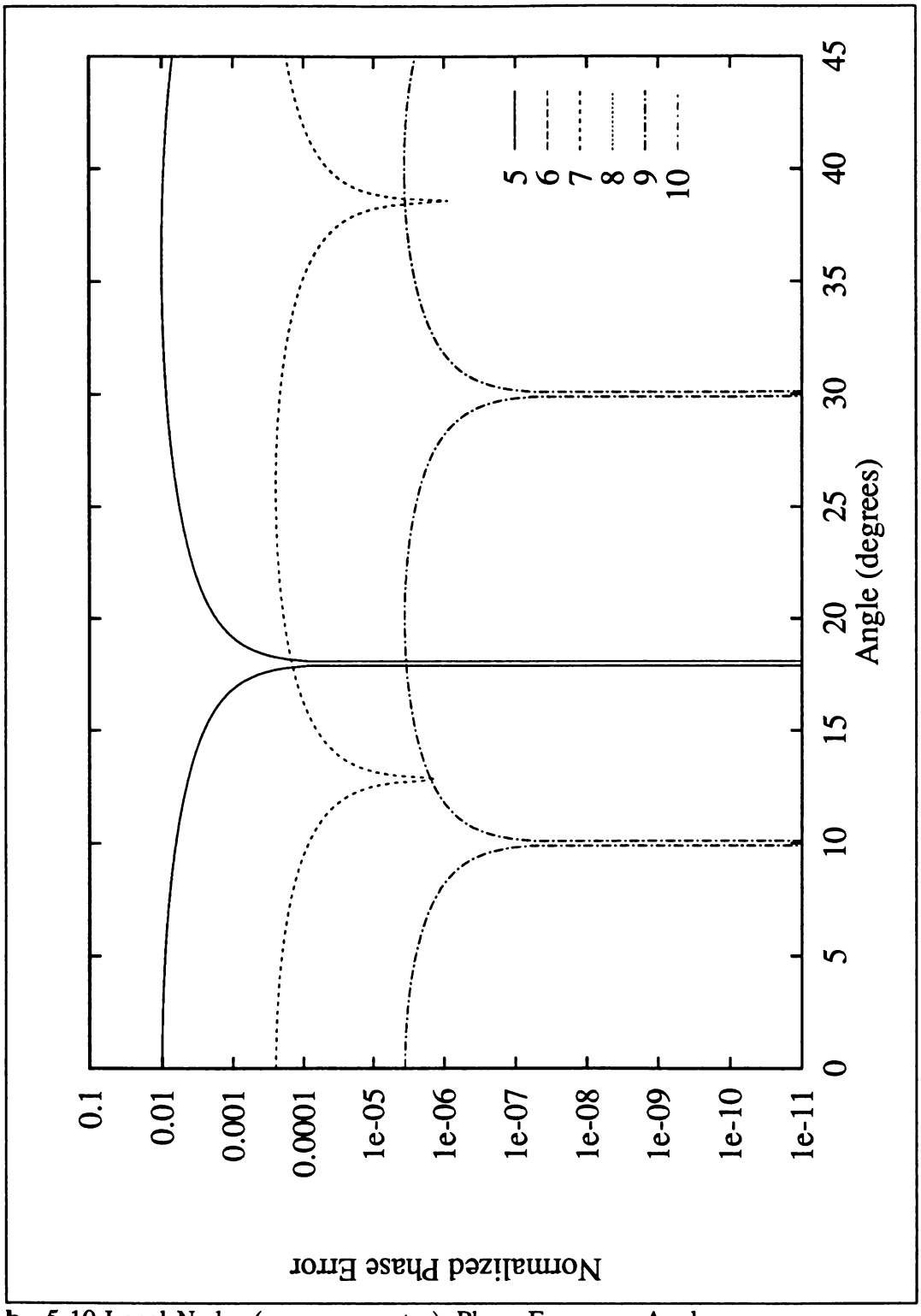

b. 5-10 Local Nodes (n-gon geometry), Phase Errors vs. Angles

Figure 3.3.2.3. (continued)

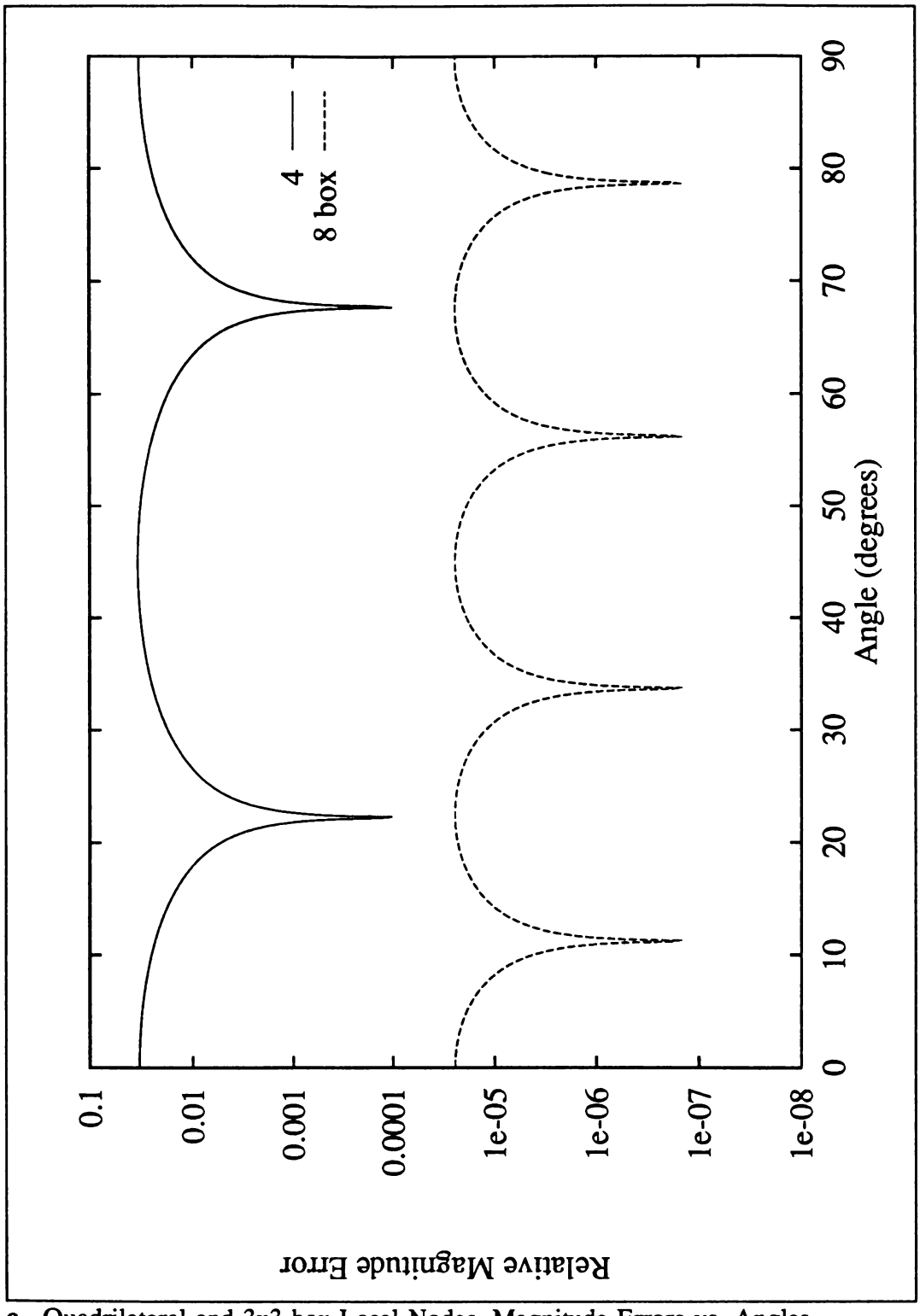

c. Quadrilateral and 3x3 box Local Nodes, Magnitude Errors vs. Angles

Figure 3.3.2.3. (continued)

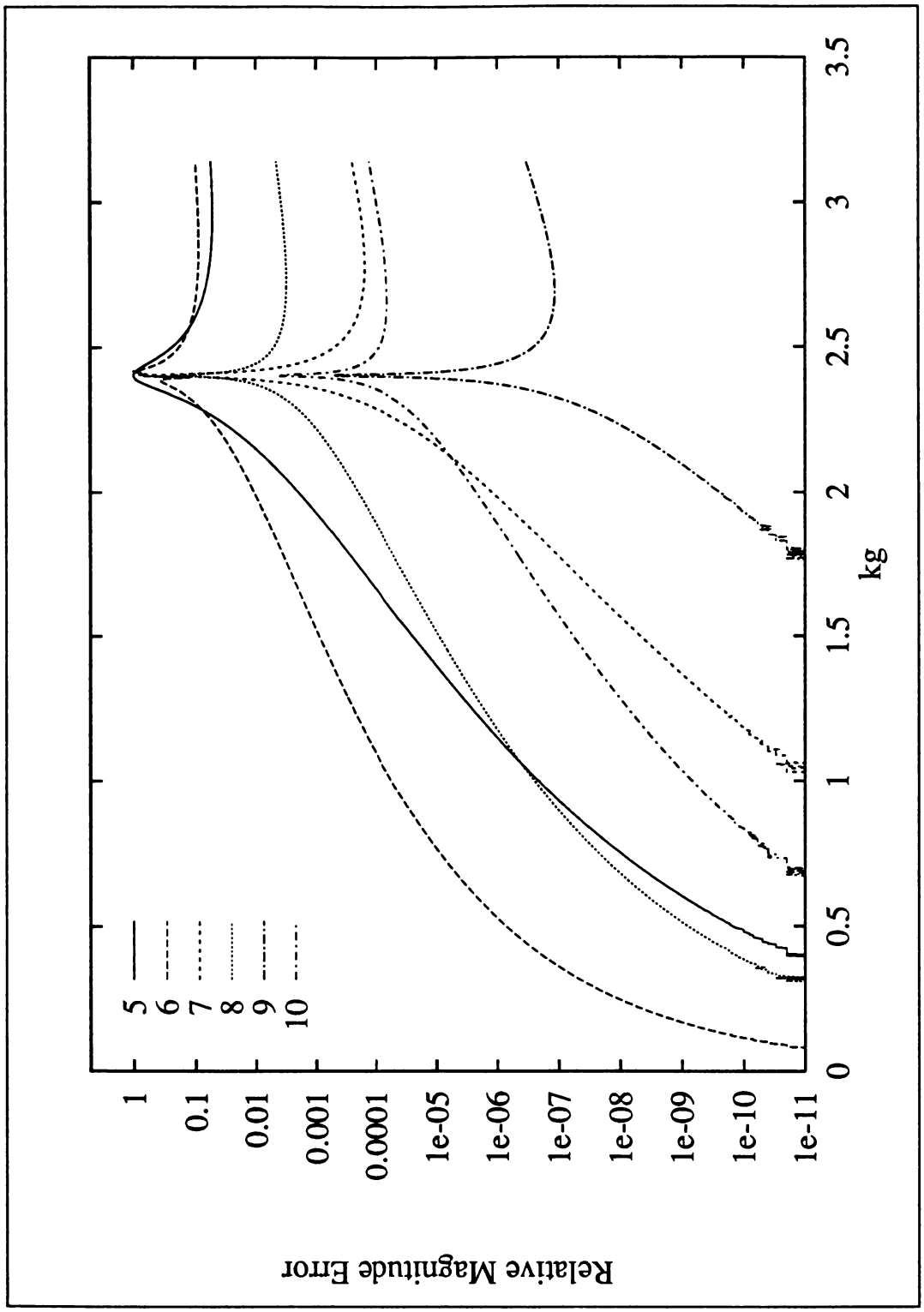

a. 5-10 Local Nodes (n-gon geometry), Magnitude Errors vs. Reduced Frequency

Figure 3.3.2.4. Varying Number of Local Nodes (4-10) Using Worst Case Angle

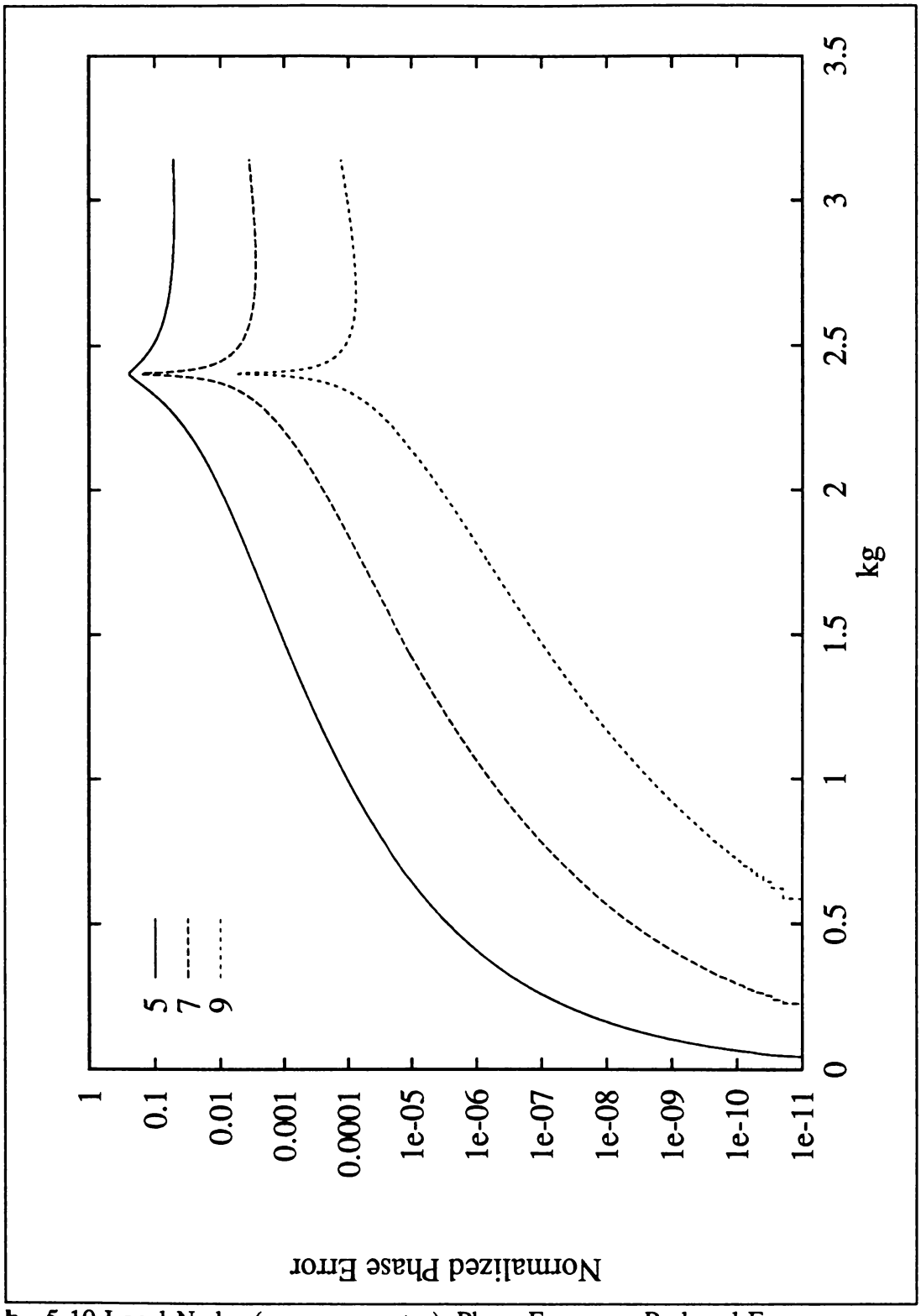

b. 5-10 Local Nodes (n-gon geometry), Phase Errors vs. Reduced Frequency

Figure 3.3.2.4. (continued)

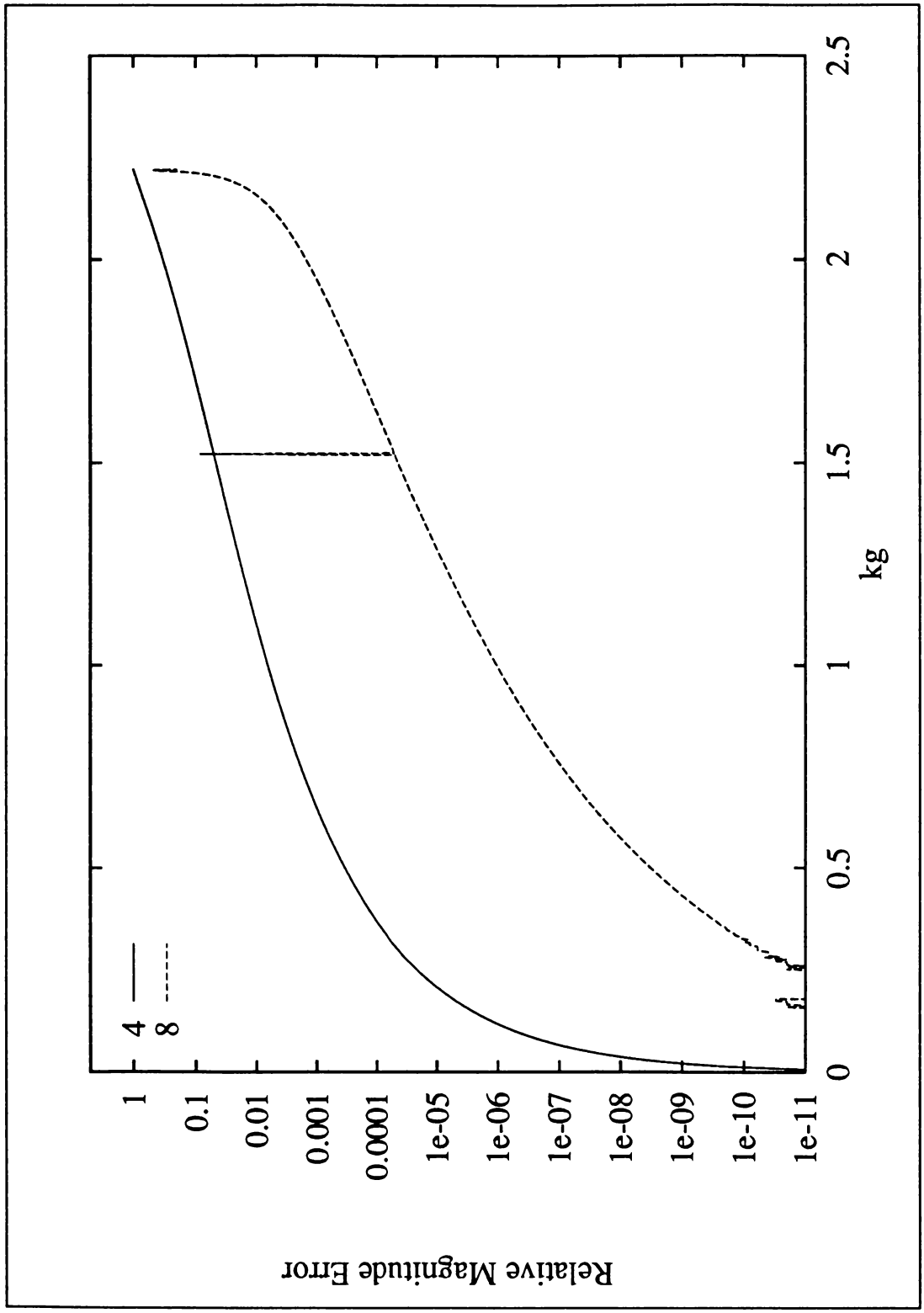

c. Quadrilateral and 3x3 box Local Nodes, Magnitude errors vs. Reduced Frequency

Figure 3.3.2.4. (continued)

3.4 Robustness

3.4.1 One to Four Plane Waves

To examine how well the method handles multiple plane waves, several extra plane wave solutions are superimposed on the local nodes of the standard case (section 3.1.1). In this section, the effects of using one, two, three or four independent plane waves is studied. The error in the magnitude is, for a large portion of reduced frequencies, less than the error for one plane wave. For the phase error, there is no significant error for one plane wave, but when multiple plane waves are superimposed, the corresponding phase error plots are similar to the magnitude error plots. To accurately measure the error incurred by different numbers of plane waves (figs. 3.4.1.1a+b) it is important to place the waves at skew angles, so that the solution process does not use symmetry to mimic the same error (as was discovered when the waves were placed 90° apart).

The hypothetical source strengths form "lobes" about the computed node, with the larger lobes pointing in the direction of the oncoming plane waves (figs. 3.4.1.2a-d). If the magnitudes are varied, the sizes of the lobes vary accordingly. For one and two oncoming waves, a few small lobes extend in directions other than that of the oncoming wave(s) as noted in section 3.2.2. In general, larger lobes extend in the direction of the source of the oncoming plane waves. The total number of lobes present is a function of the positions of the computational nodes relative to the oncoming wave(s) and the number of computational nodes.

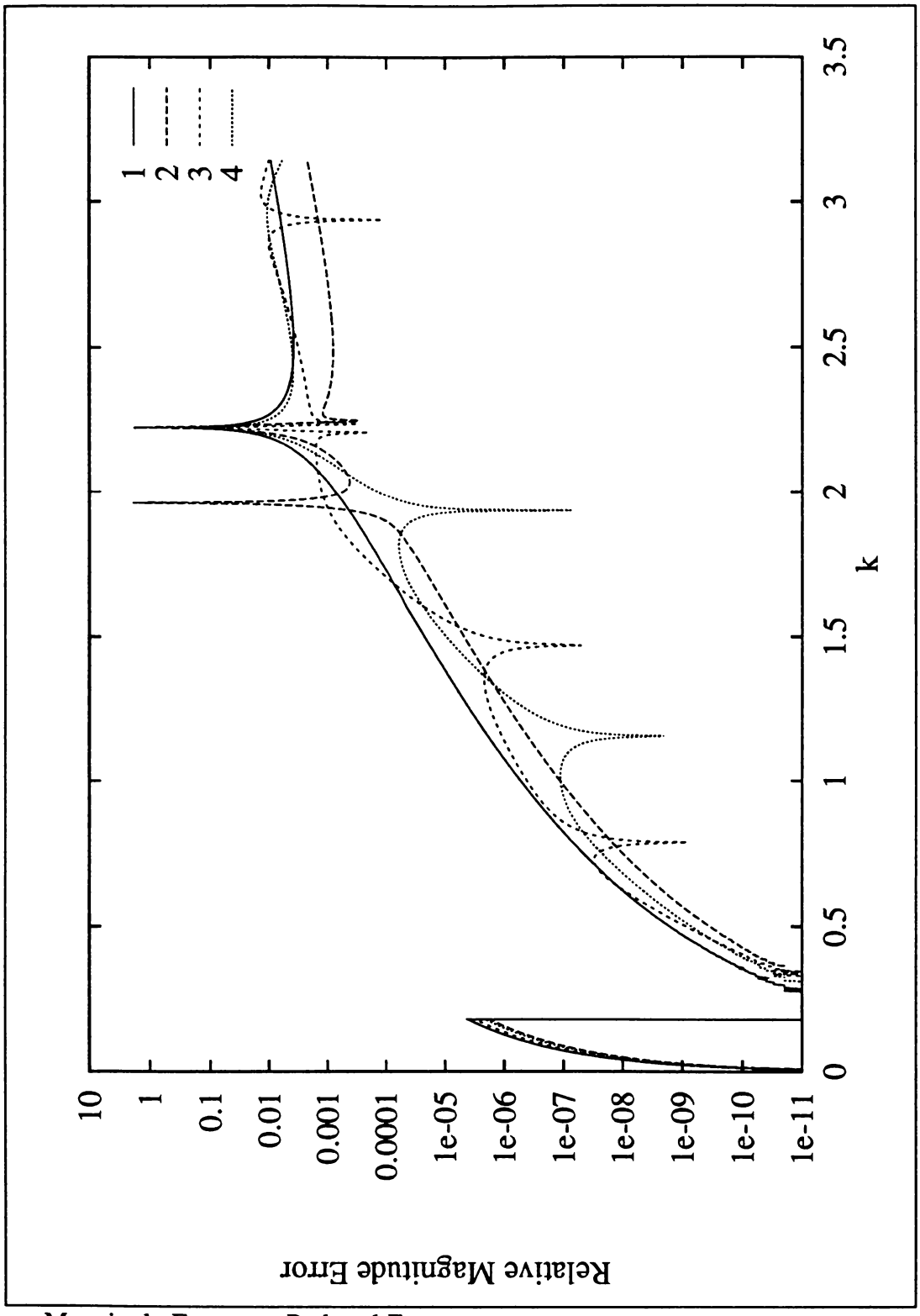

a. Magnitude Errors vs. Reduced Frequency

Figure 3.4.1.1. Multiple Plane Wave Comparison

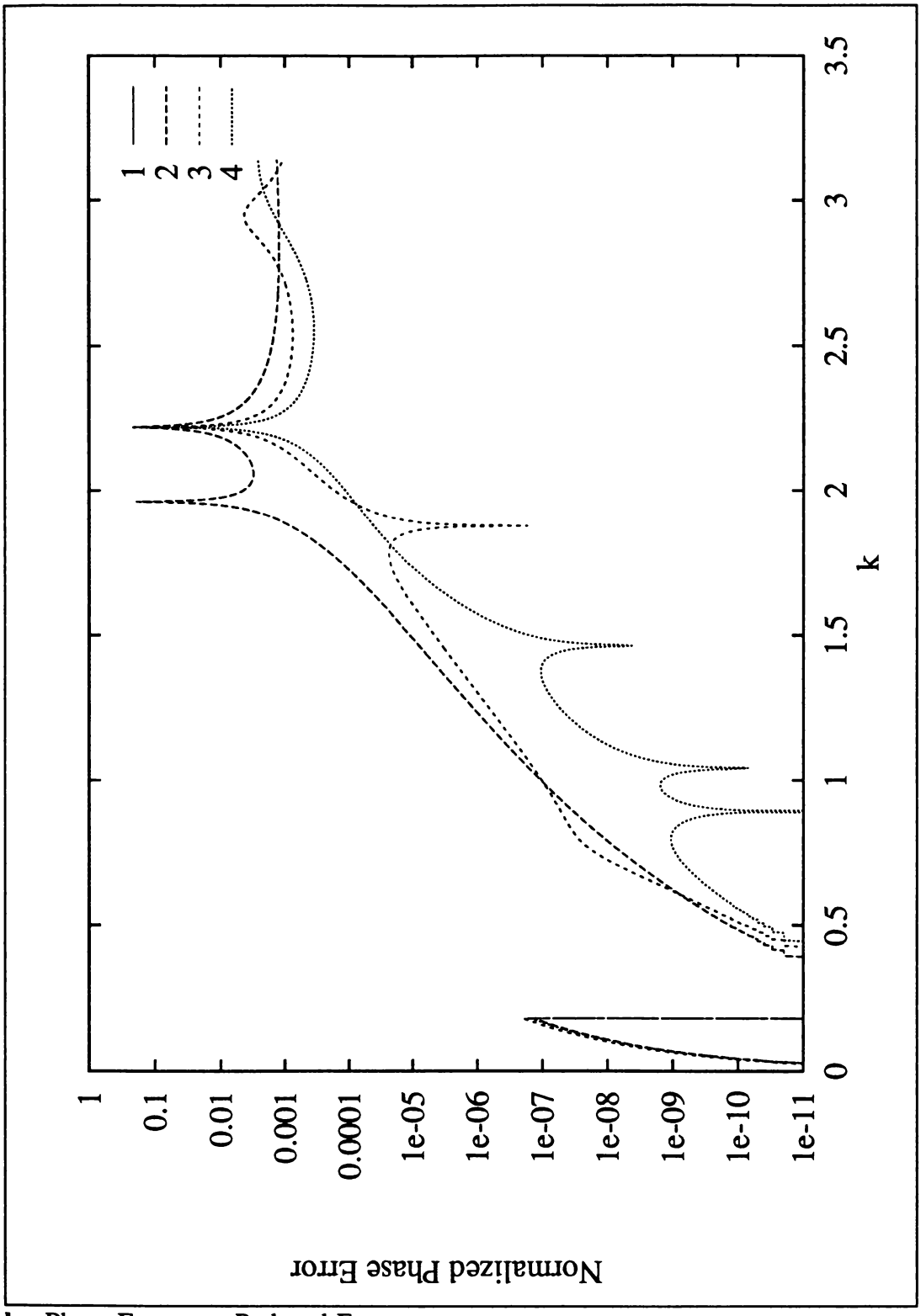

b. Phase Errors vs. Reduced Frequency

Figure 3.4.1.1. (continued)

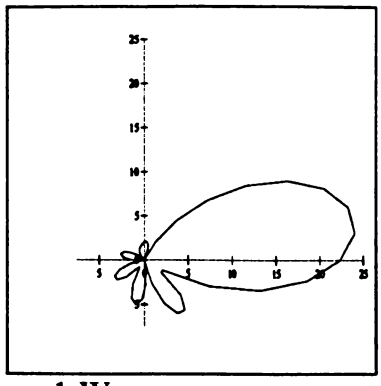

a. 1 Wave

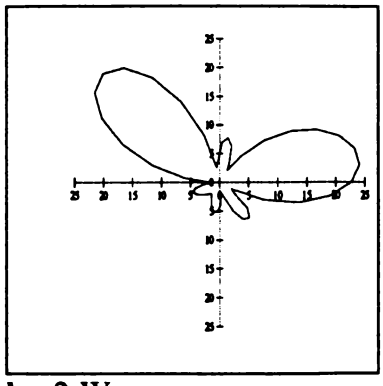

b. 2 Waves

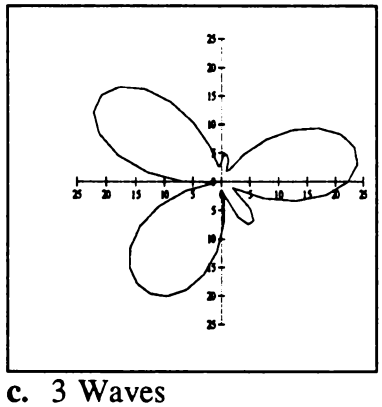

c. 3 Waves

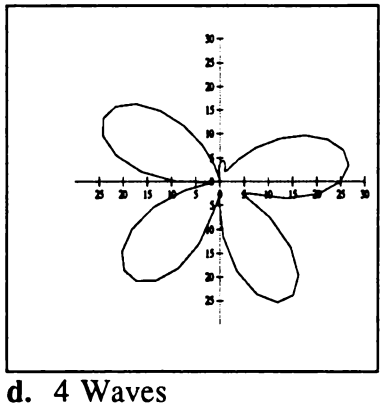

d. 4 Waves

Figure 3.4.1.2 Hypothetical source strength distributions for varying numbers of incoming plane waves.

3.4.2 Monopoles and Evanescent Waves

Plane waves are not the only sources of sound which the HSM must be able handle, as monopoles, n-poles and evanescent waves may also be used. An evanescent wave is similar to a plane wave along one axis, but decays exponentially along the other. Figures 3.4.2.1a+b show the development of the errors of a plane wave, one to three monopoles, and evanescent waves (with phase Mach numbers of 0.2 and 0.8). The monopoles have similar magnitude errors as the plane wave, and similar phase errors results comparable to prior cases conducted with more than one plane wave. The evanescent waves' solution is much poorer, but improves as the Mach number increases. If the Mach number is supersonic (>1), the evanescent wave becomes a plane wave, explaining why the evanescent errors seem to converge toward the errors for a plane wave as the Mach number increases.

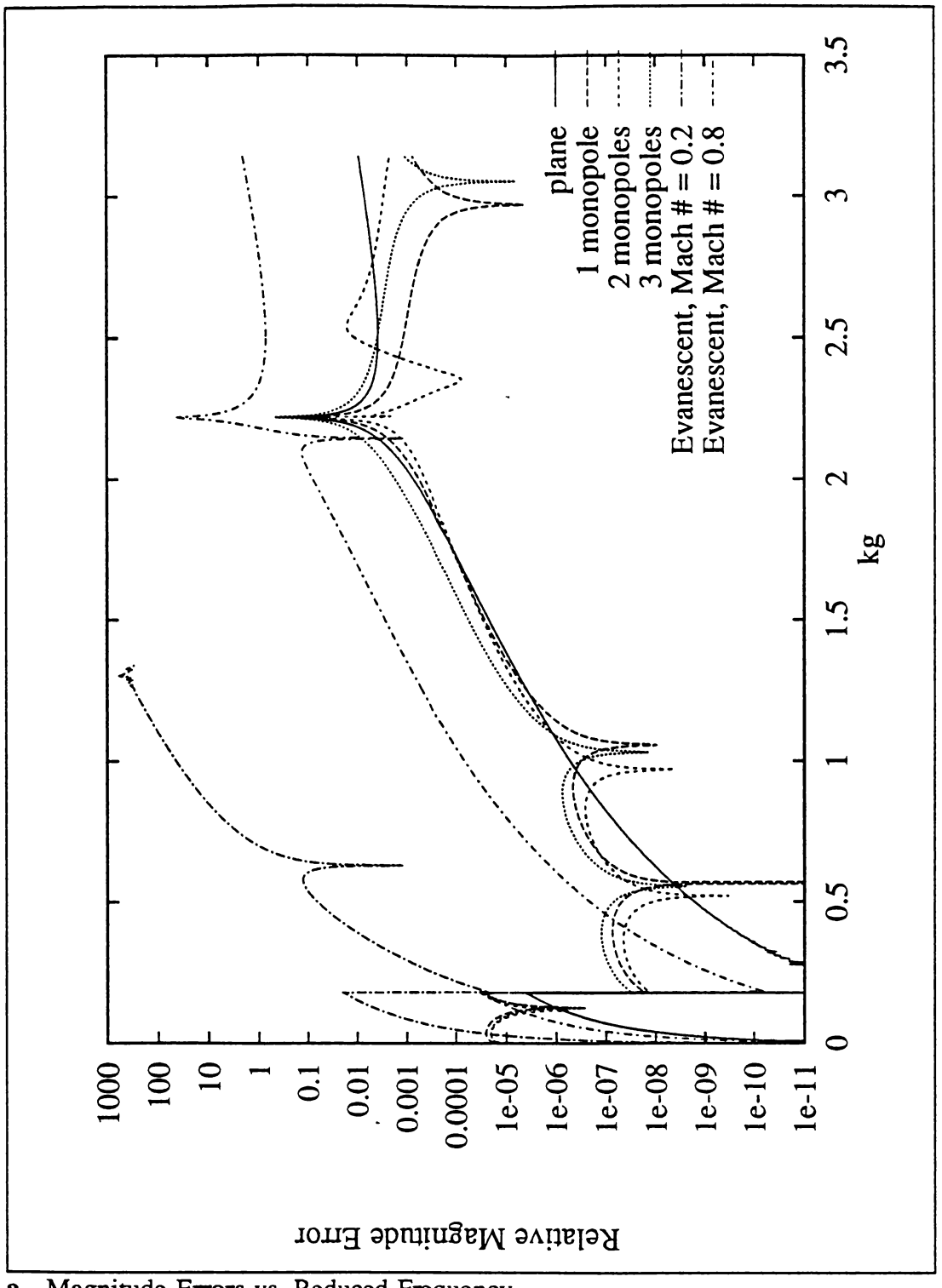

a. Magnitude Errors vs. Reduced Frequency

Figure 3.4.2.1. Comparison of Plane, Monopole and Evanescent Wave Computational Accuracy

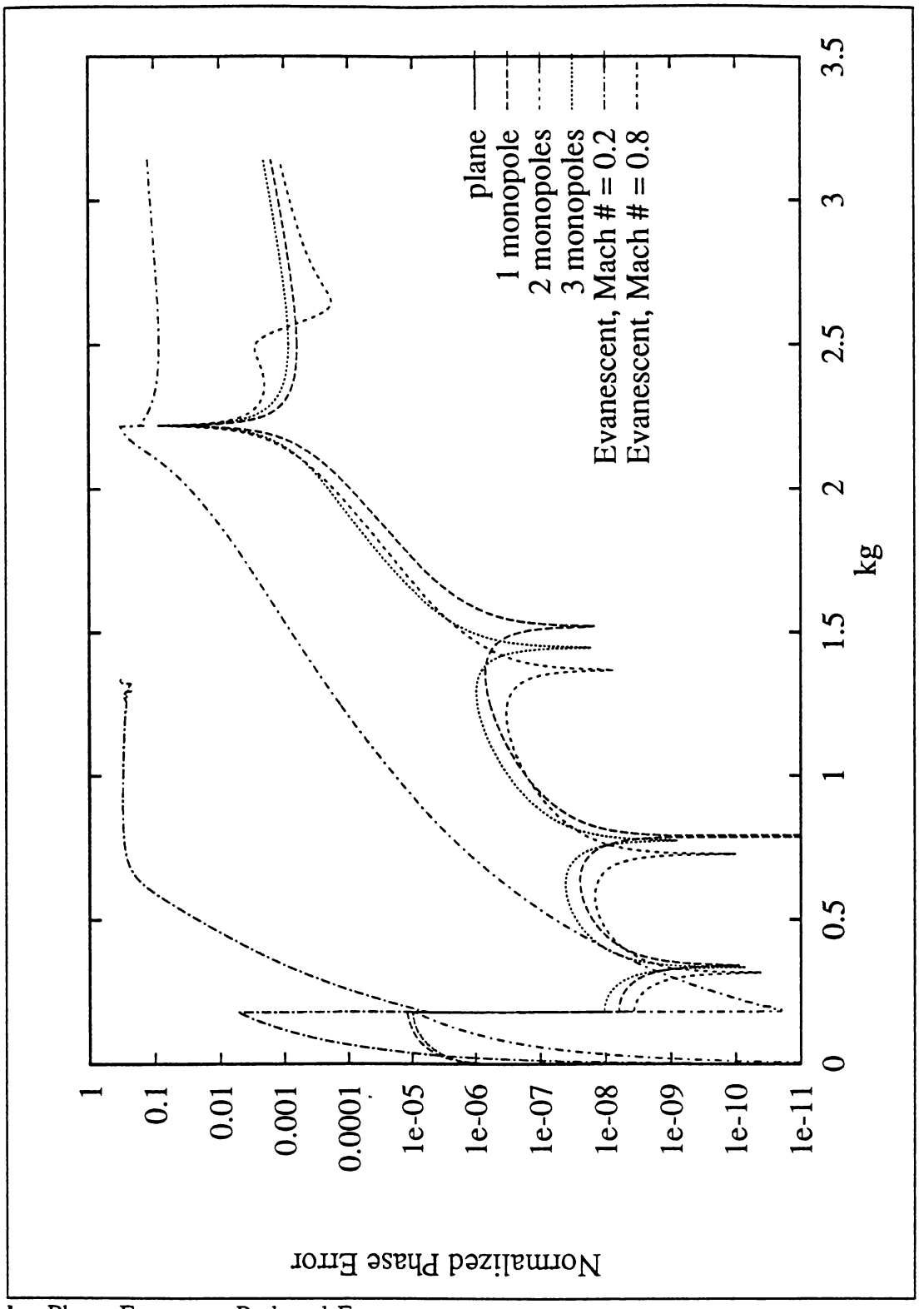

b. Phase Errors vs. Reduced Frequency

Figure 3.4.2.1. (continued)

3.4.3 Aspect Ratio

This aspect ratio study examines the changes in the solution as the grid is varied. Aspect ratios of 1:1, 2:1 and 4:1 are examined (see fig. 3.4.3.1). The square grid's nodes are spread apart in the x direction by a factor of the aspect ratio, while in the y direction the nodes are a unitary distance apart. A plane wave is passed from the right and from the top through the computational domain to determine how the method would responds. When a plane wave is passed along an axis for the 1:1 case, the square becomes more accurate than usual. To prevent this from affecting the results, cases are conducted with the wave approaching from 15° and 105°. The results of the computations are displayed using k_d, with L_d based on the diagonal of the grid.

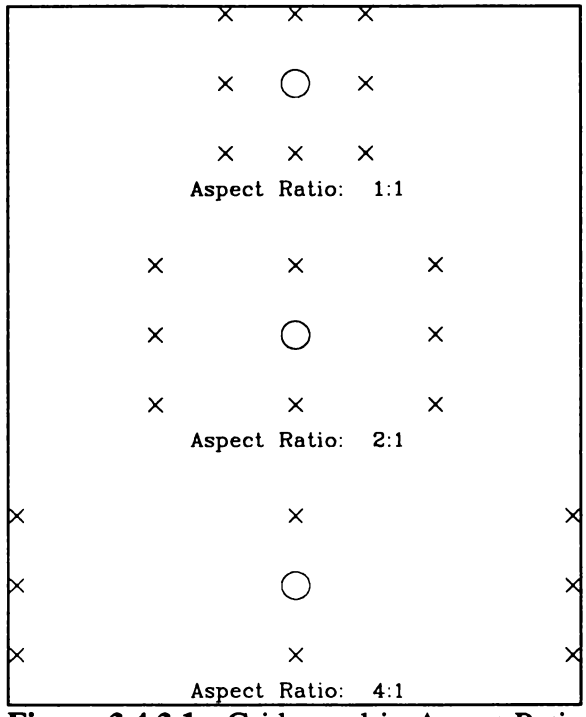

Figure 3.4.3.1. Grids used in Aspect Ratio study.

Figures 3.4.3.2-3 shows that while the reduced frequency (k_d, based on the diagonals of the different grids) is less than 2, the angle the wave is coming from is inconsequential. As a check, note that for an aspect ratio of 1:1, the 15° and 105° cases produce the same magnitude errors, as they are the same problem. The accuracy of the solution does decrease by a magnitude for grids without a 1:1 aspect ratio, but the size of the error appears to be limited.

Examination of hypothetical source strengths for the properly non-dimensionalized aspect ratios shows that the shapes are similar for the different aspect ratios. (figures

3.4.3.4-5). The hypothetical source strengths cannot be normalized as precisely as for the study of the number of hypothetical sources (section 3.2.2).

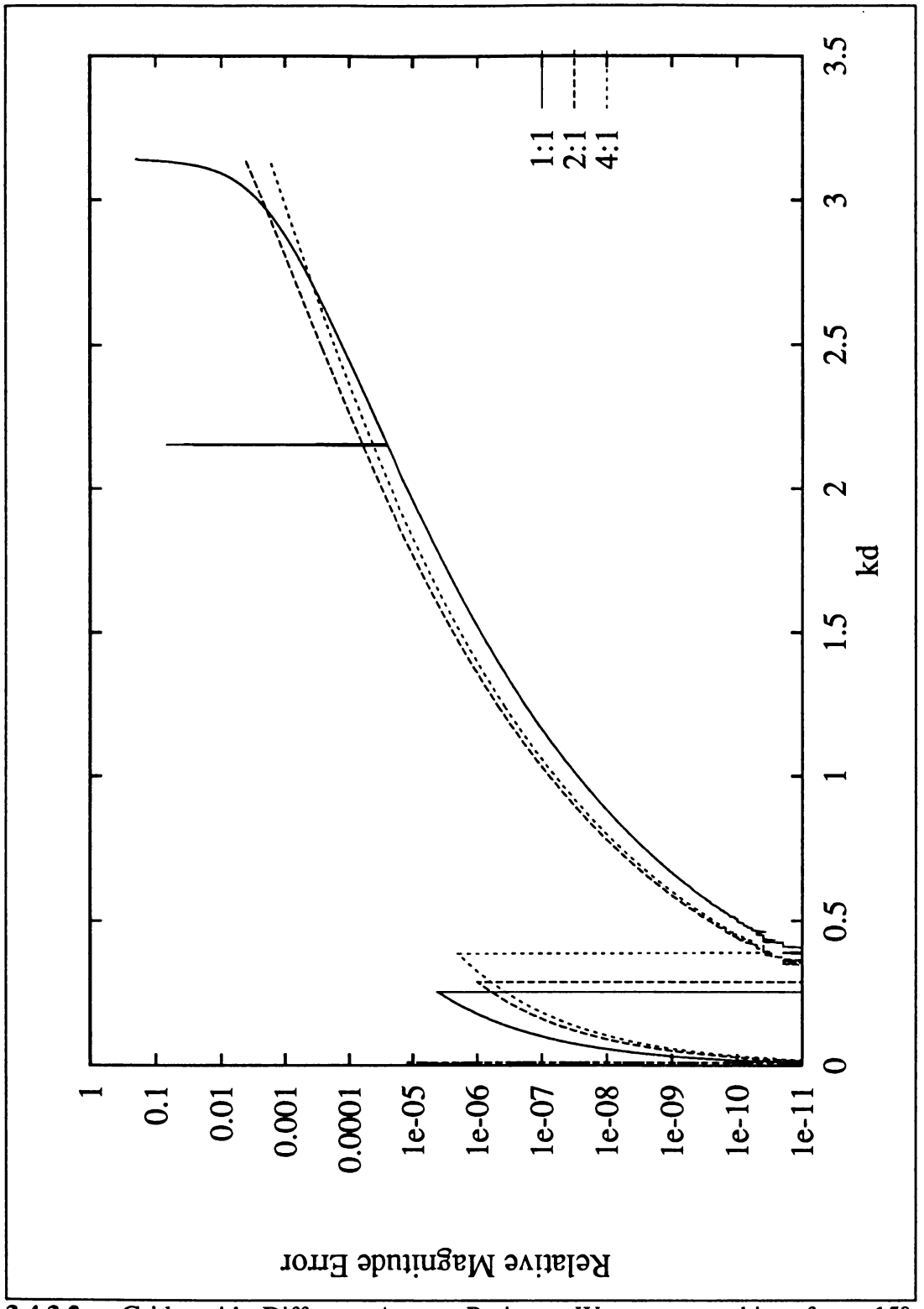

3.4.3.2. Grids with Different Aspect Ratios: Wave approaching from 15°, Magnitude Errors vs. Reduced Frequency

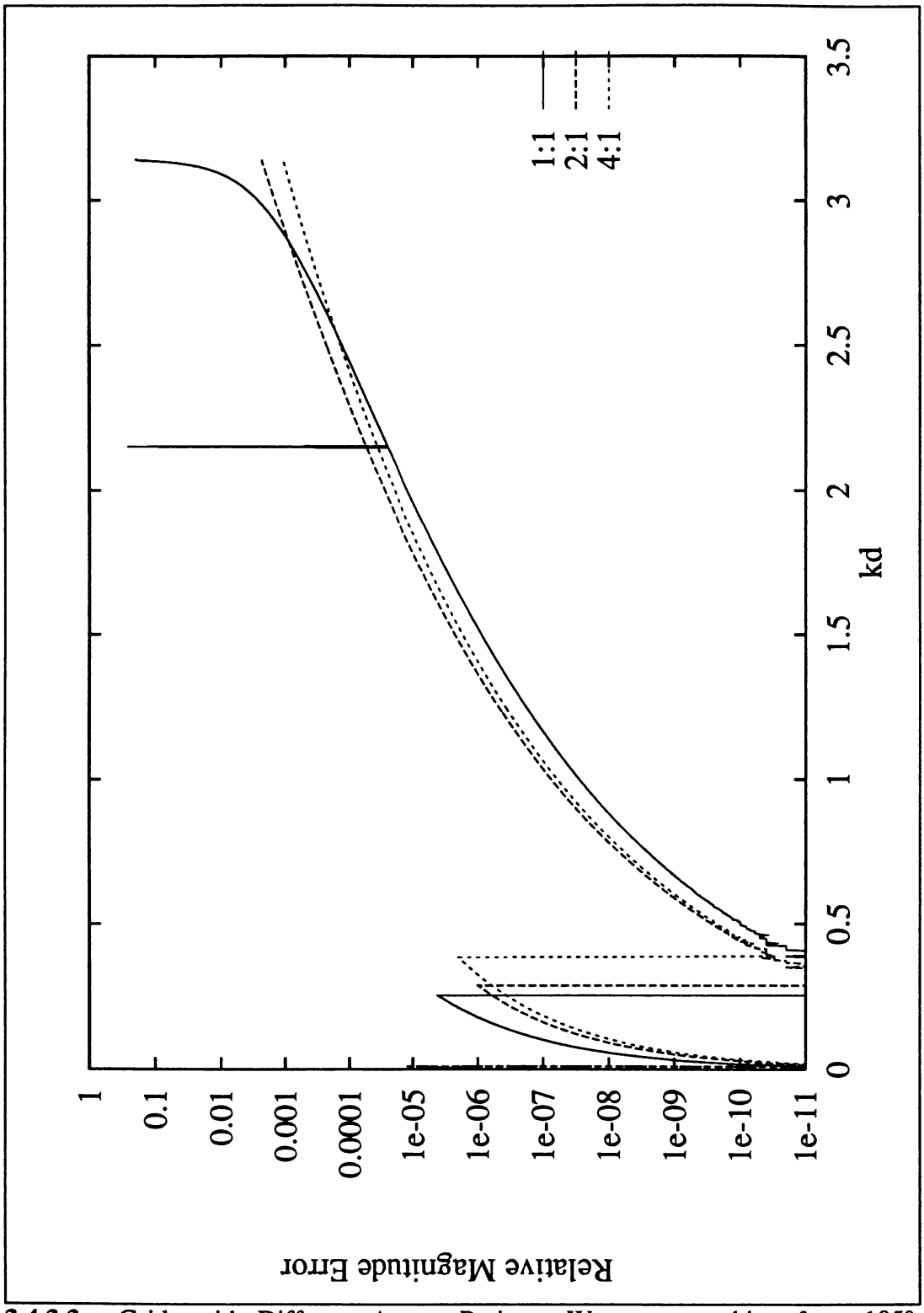

3.4.3.3. Grids with Different Aspect Ratios: Wave approaching from 105°, Magnitude Errors vs. Reduced Frequency

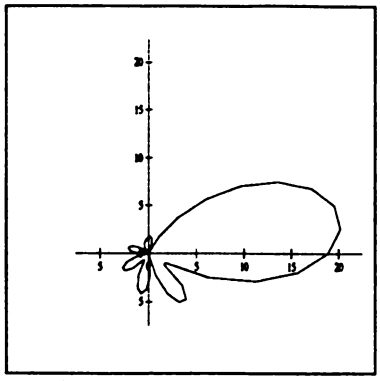

a. AR 1:1

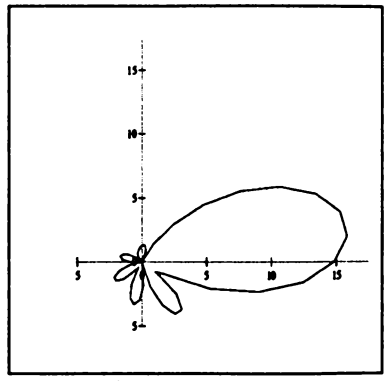

b. AR 2:1

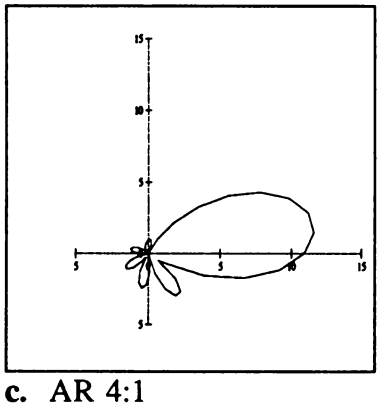

c. AR 4:1

Figure 3.4.3.4. Hypothetical source strength distributions for different aspect ratios, with a plane wave approaching from 15°.

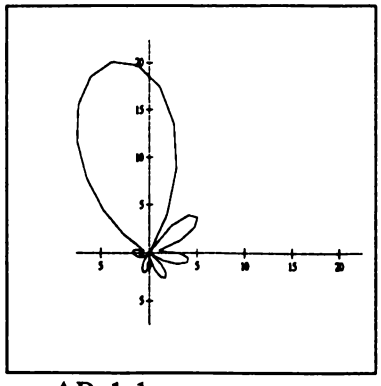

a. AR 1:1

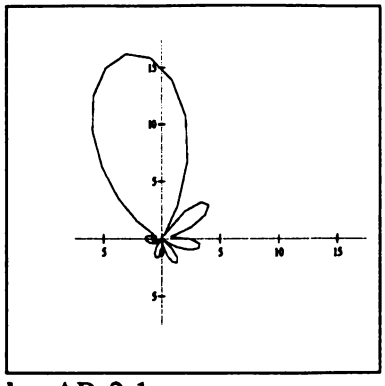

b. AR 2:1

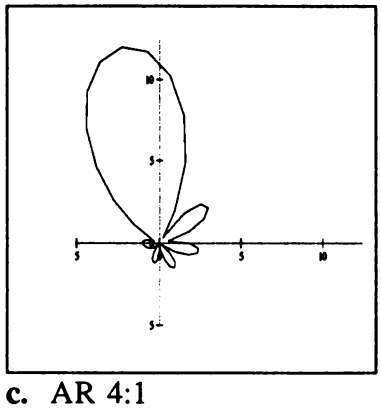

c. AR 4:1

Figure 3.4.3.5. Hypothetical source strength distributions for different aspect ratios, with a plane wave approaching from 105°.

3.5 Comparison to Existing Methods

3.5.1 Comparison Using Single Computed Node Grid

In the following, the new method is compared to simple 5 and 9 node finite difference schemes (see Appendix 3). The five and nine node methods used have built in singularities at $k_g = 2$ and $k_g = \sqrt{10/3}$, respectively. Large errors in the magnitude appear for a reduced frequency (k_g) greater than one for the five and nine node methods. Figures 3.5.1.1a+b show the accuracy of accurate the hypothetical source method relative to finite difference schemes. The HSM's solutions do not deteriorate from the truncation errors that plague the finite difference methods, but the HSM fails as the reduced frequency approaches the resonant frequency, resulting in an infinite number of homogeneous solutions corrupting the solution.

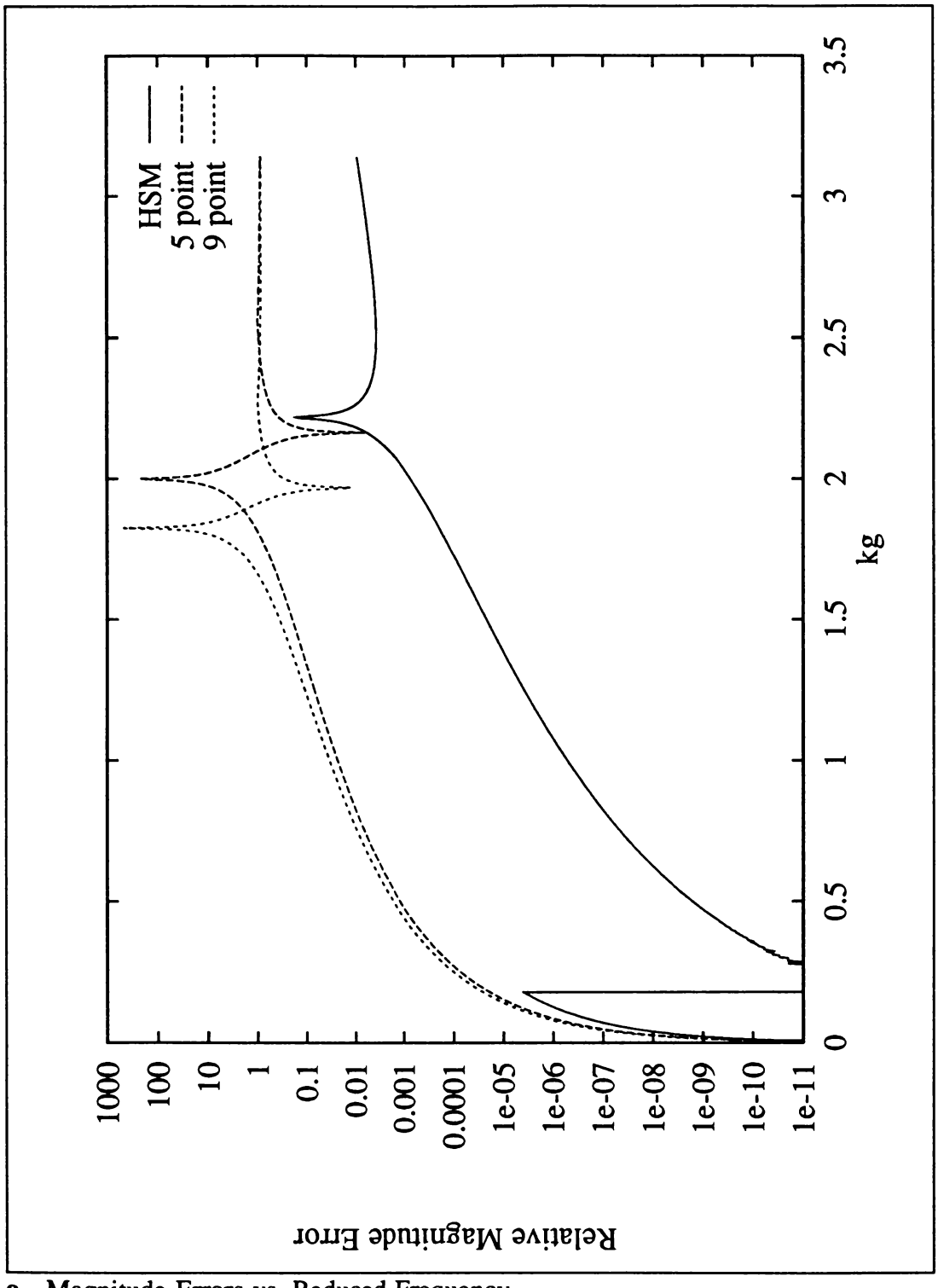

a. Magnitude Errors vs. Reduced Frequency

Figure 3.5.1.1. Comparison of hypothetical source method with 5 and 9 node FD methods

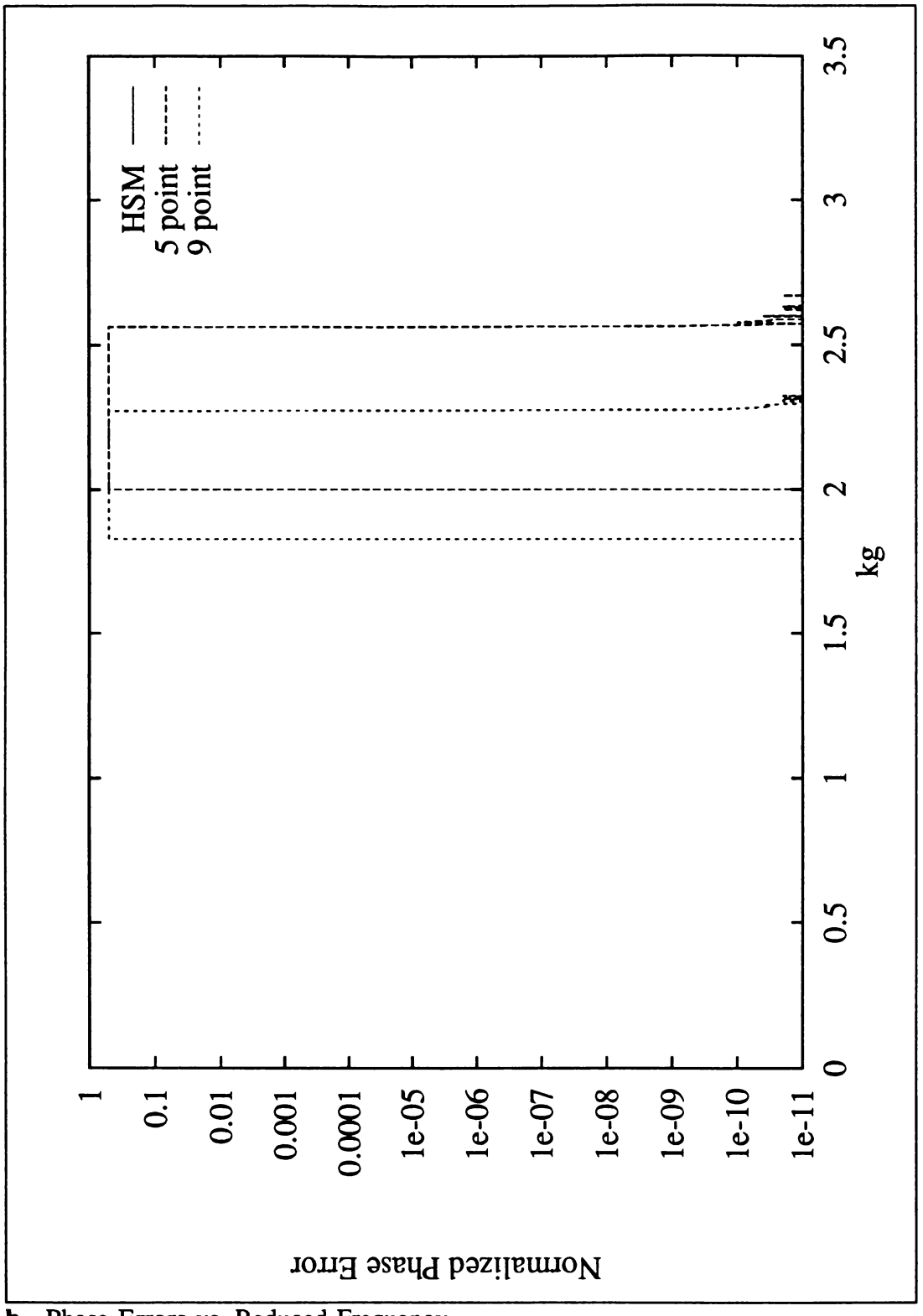

b. Phase Errors vs. Reduced Frequency

Figure 3.5.1.1. (continued)

3.6 2-D Boundary Value Test Problem

3.6.1 Problem Description and Boundary Conditions

To verify that the solution's characteristics extend beyond a single node, a new testing scheme is used with a rectangular 15x15 node Cartesian mesh. To compare the HSM with other methods, simple five and nine node finite difference schemes are used with the same boundary conditions.

The grid spacing is one in both the x and y directions; the five and nine node FD cases are also computed with a grid that is twice as dense (grid spacing is ½ in both the x and y directions). The boundary conditions used by the HSM and the five and nine node FD schemes have Dirichlet boundary conditions on the bottom and right hand sides, and radiation boundary conditions are used on the left and top sides (see fig 3.6.1.1). Three monopole sound sources are placed on a line below the computational grid as in figure 3.6.1.1, to compute the exact solutions for the Dirichlet boundary conditions, and to inform the radiation boundary conditions as to the position of the source of the sound. To provide more challenging boundary conditions, the HSM case is also computed using three nodes placed as in figure 3.6.1.2.

A block tri-diagonal matrix solver is used to solve the systems of equations, following a scheme set forth by Caruthers and Dalton [2, p. 79, eq. 38-46]. That scheme is modified to allow for the appropriate boundary conditions. Using the notation of that reference as follows (in case $|C^1| = 0$):

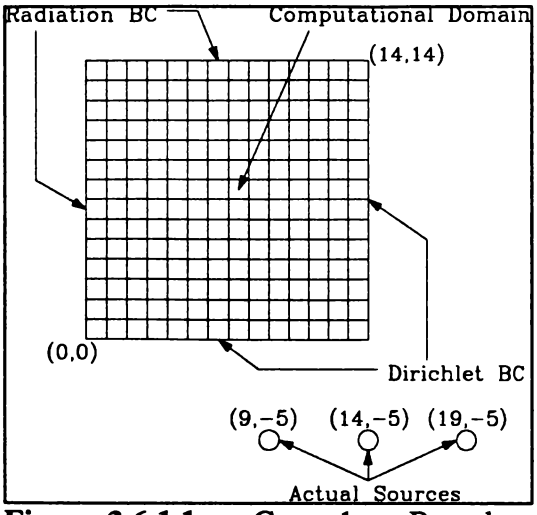

Figure 3.6.1.1. Case 1: Boundary Conditions and Standard Actual Sources.

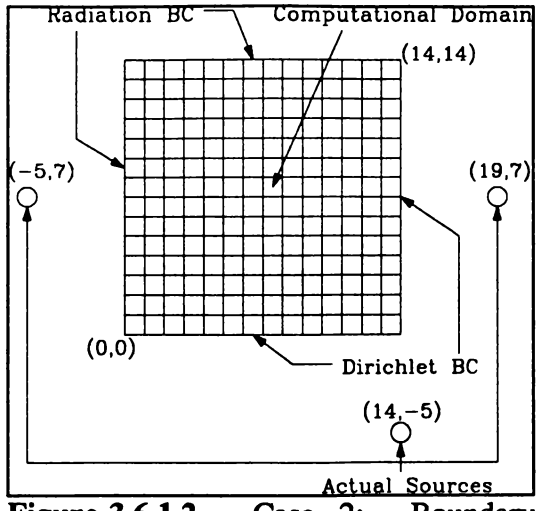

Figure 3.6.1.2. Case 2: Boundary Conditions and Difficult Actual Sources (for extra "odd" HSM case only).

$$B^1\phi_1 + C^1\phi_2 = F^1$$

$$\phi_2 = a_1' + b_1'\phi_1$$

$$B^1\phi_1 + C^1(a_1' + b_1'\phi_1) = F^1 \qquad (3.3)$$

$$(B^1 + C^1b_1')\phi_1 = F^1 - C^1a_1'$$

$$\therefore \phi_1 = (B^1 + C^1b_1')^{-1}(F^1 - C^1a_1')$$

Furthermore, to allow for radiating boundary conditions on the right hand side ($|F^M| \neq 0$):

$$A^M\phi_{M-1} + B^M\phi_M = F^M$$

$$B^M\phi_M = F^M - A^M\phi_{M-1}$$

$$\phi_{I+1} = a_I + b_I\phi_I \qquad (3.4)$$

$$B^M\phi_I = B^M(a_{I-1} + b_{I-1}\phi_{I-1})|_{I=M} = B^Ma_{M-1} + B^Mb_{M-1}\phi_{M-1}$$

$$\therefore a_{M-1} = (B^M)^{-1}F^M, \quad b_{M-1} = -(B^M)^{-1}A^M$$

3.6.2 Results

To examine the accuracy of the large test grid, the maximum, average, minimum and standard deviations of the magnitude and phase errors are computed for a range of reduced frequencies.

Figures 3.6.2.1-3 compares each method's maximum, average and standard deviations of its magnitude and phase errors. For the five and nine node cases, the errors decrease as the grid's mesh is made denser, but the errors are still much greater than those of the HSM. Only as k_g becomes smaller (< 0.1) does the nine node case surpass the HSM. Interestingly, the HSM has more problems at lower frequencies than at intermediate ones. Section 3.3.1 details potential reasons for this.

Figures 3.6.2.4-5 display the statistical accuracy information of the HSM (both cases). The accuracy was similar to the results found for the 3x3 grid cases. As was found in the 3x3 case, a peak appears at $k_g = 2.221$, an expected error in light of theory and the previous computations, verifying that the resonant frequency remains as limit for a large grid. The more difficult boundary conditions of case 2 only increase the errors by about one order of magnitude, but the results are still satisfactory.

Black and white plots of the magnitude and phase for solutions with $k_g = 1$ and 2 are located in Appendix 2. They demonstrate the accuracy of the HSM by comparing actual computed mode shapes and phase contours with exact and FD solutions. To create these figures, the interpolation scheme of eq. 2.5 is applied in between the computed nodes (the exact solution plots used exact values at the interpolation points). In addition, they demonstrate how the five and nine point schemes fail for the higher frequency.

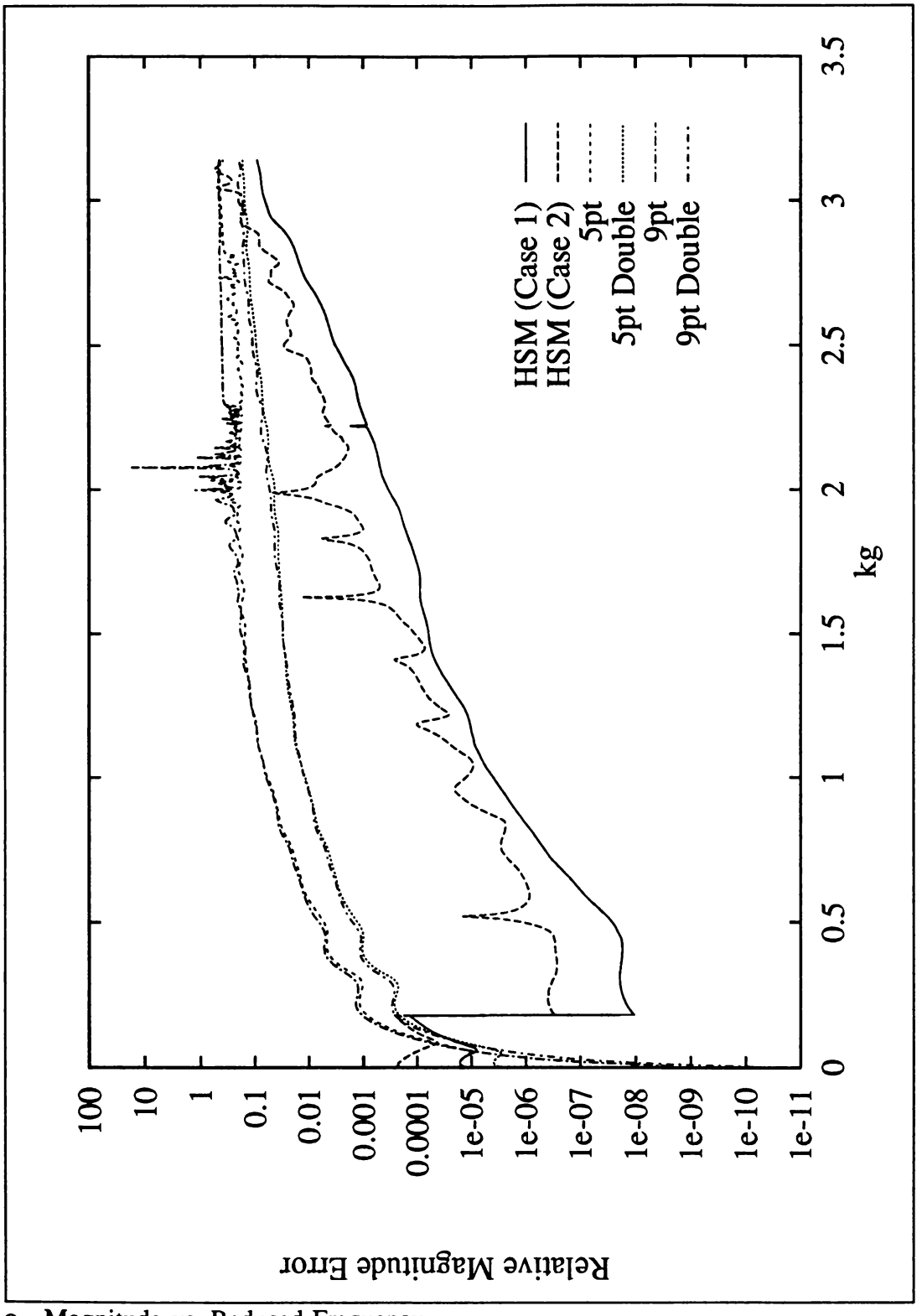

a. Magnitude vs. Reduced Frequency

Figure 3.6.2.1. Comparison Between Methods: Large Test Grid Average Errors

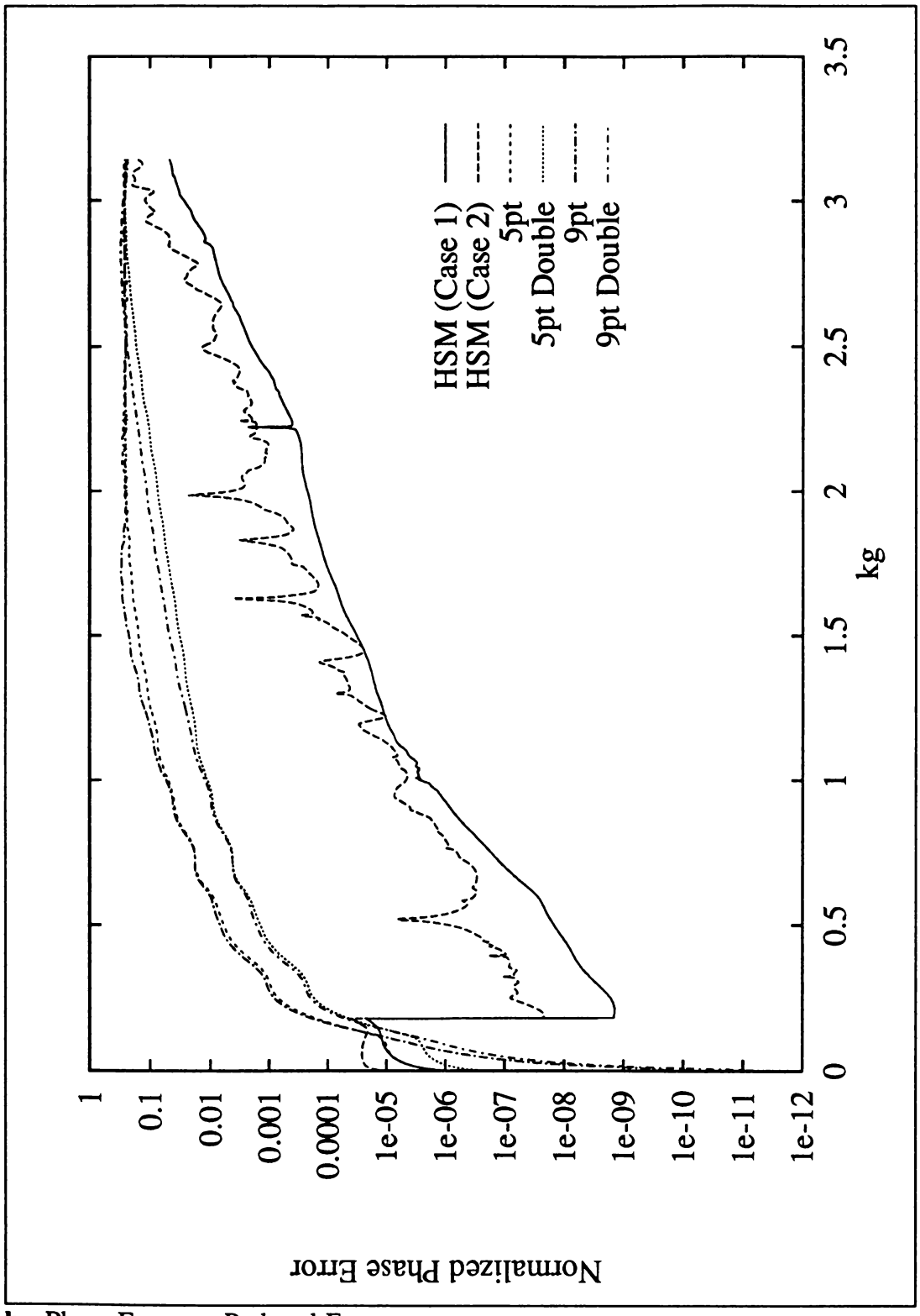

b. Phase Error vs. Reduced Frequency

Figure 3.6.2.1. (continued)

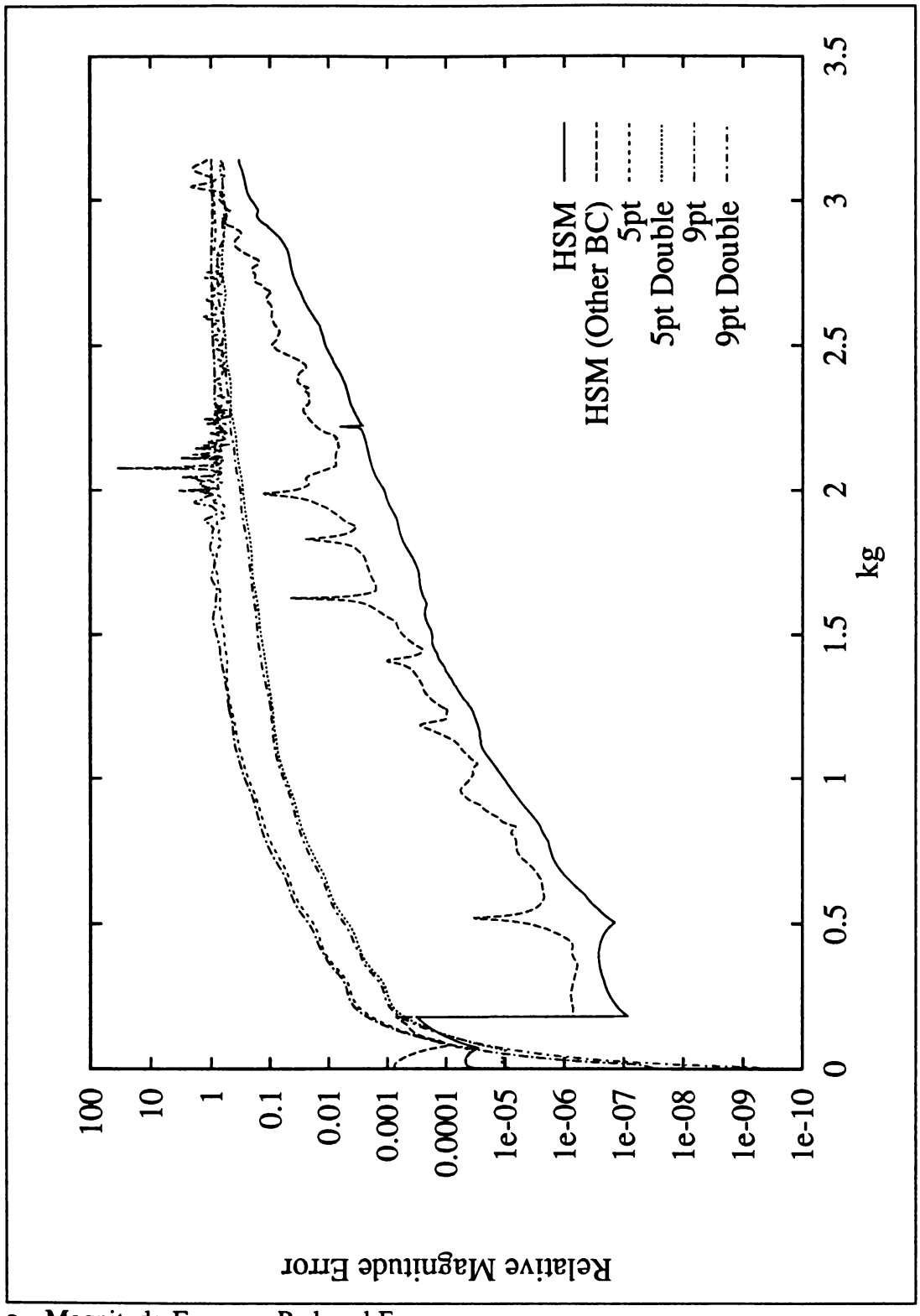

a. Magnitude Error vs. Reduced Frequency

Figure 3.6.2.2. Comparison Between Methods: Large Test Grid Maximum Errors

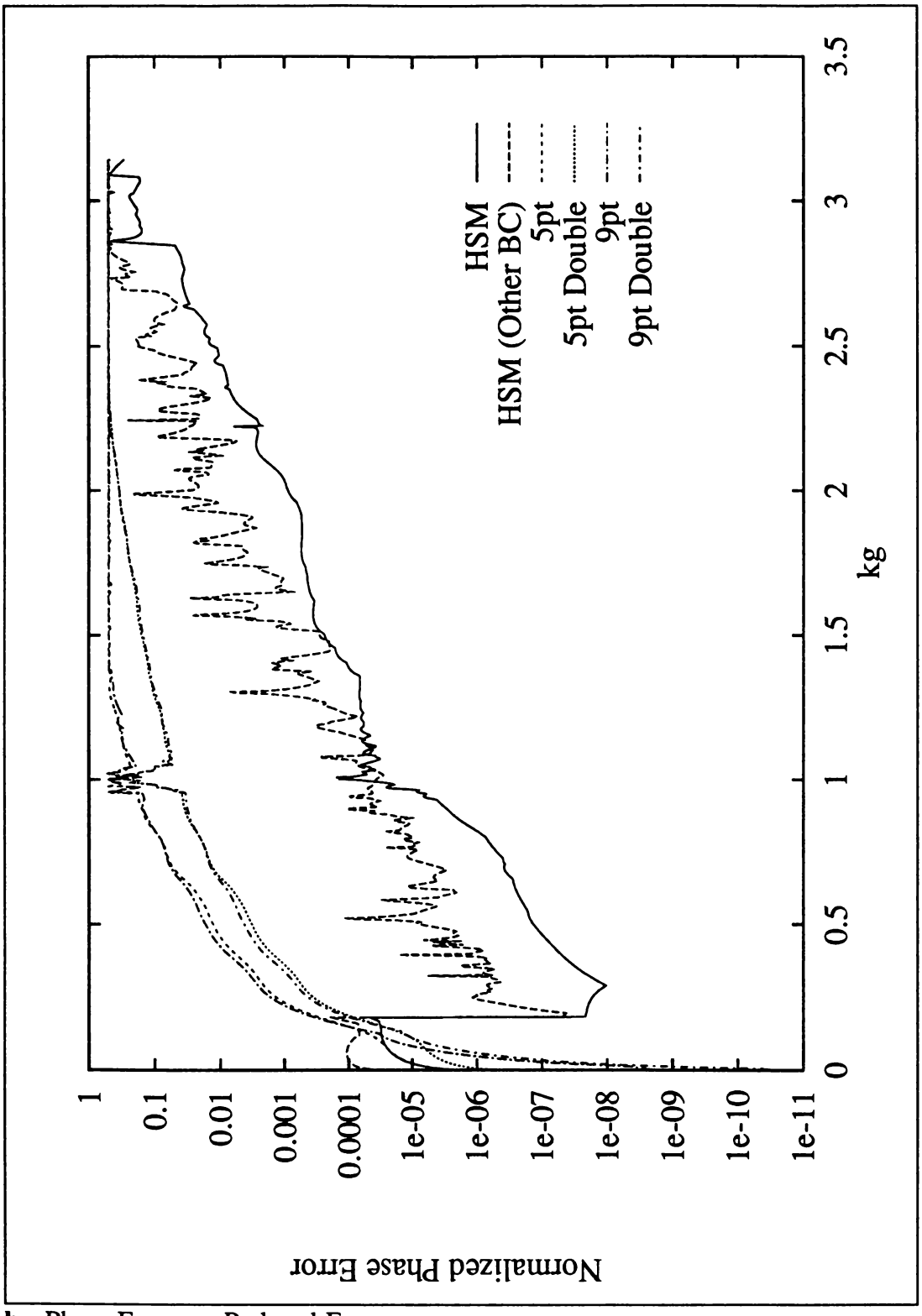

b. Phase Error vs. Reduced Frequency

Figure 3.6.2.2. (continued)

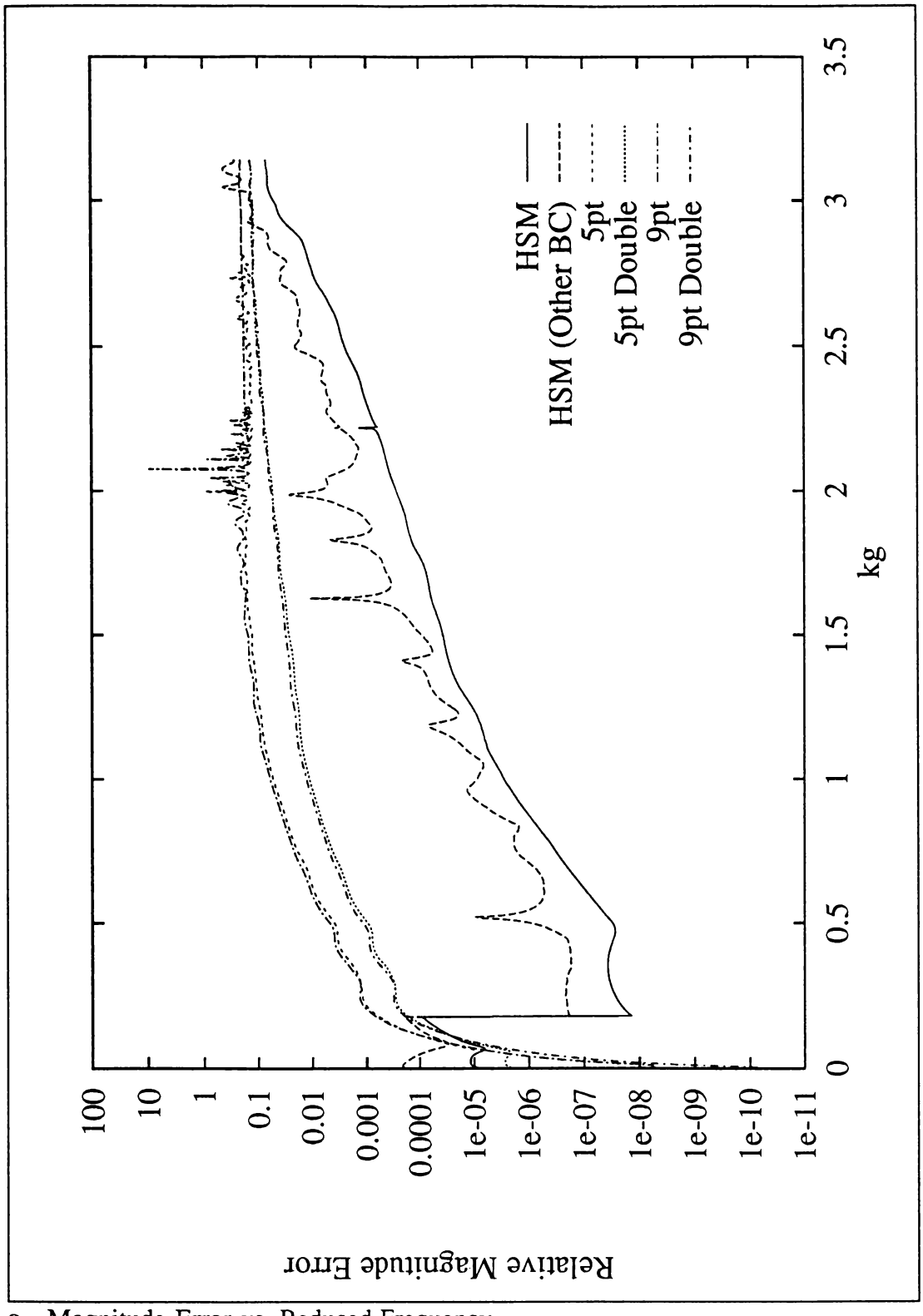

a. Magnitude Error vs. Reduced Frequency

Figure 3.6.2.3. Comparison Between Methods: Large Test Grid Standard Deviation

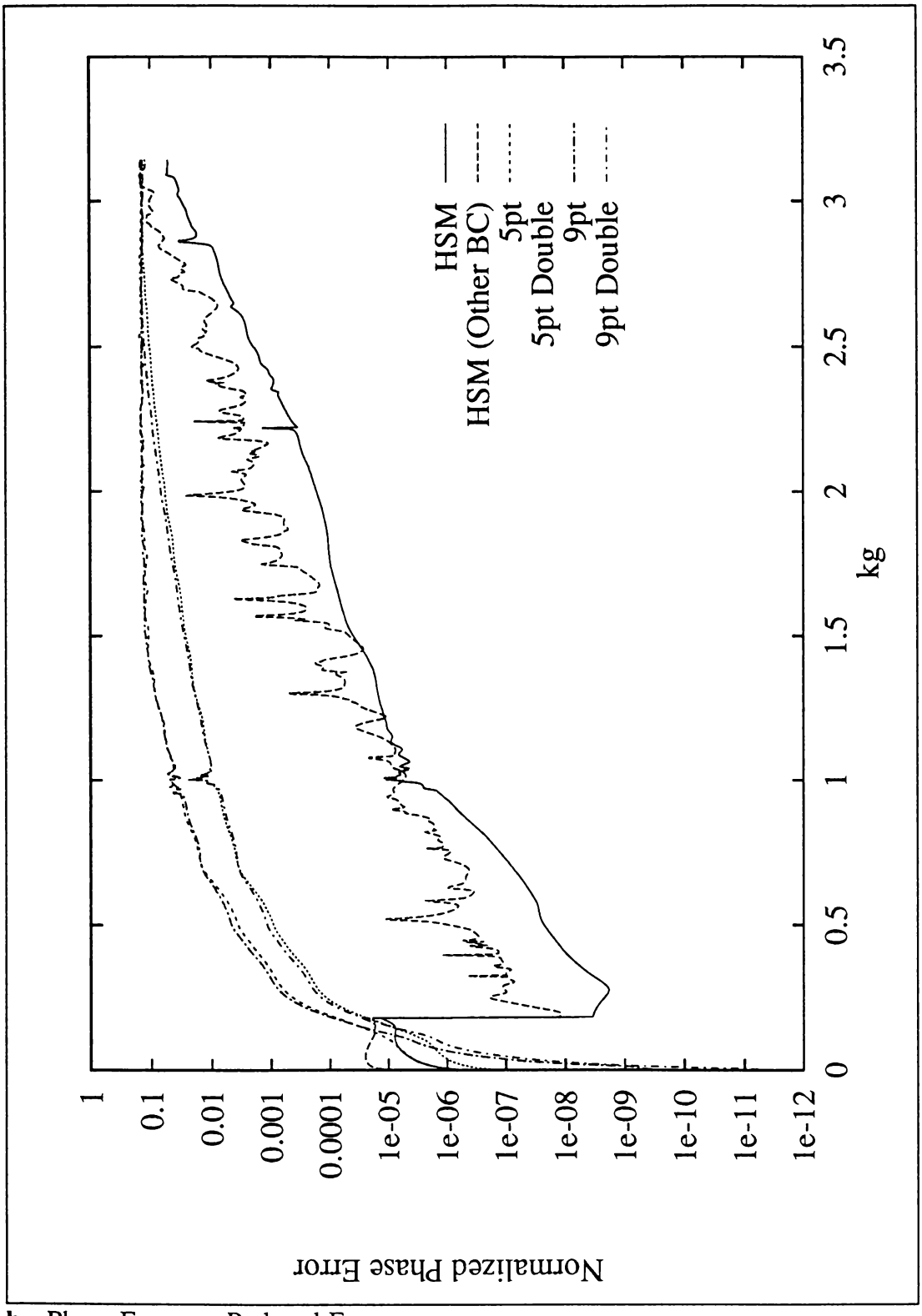

b. Phase Error vs. Reduced Frequency

Figure 3.6.2.3. (continued)

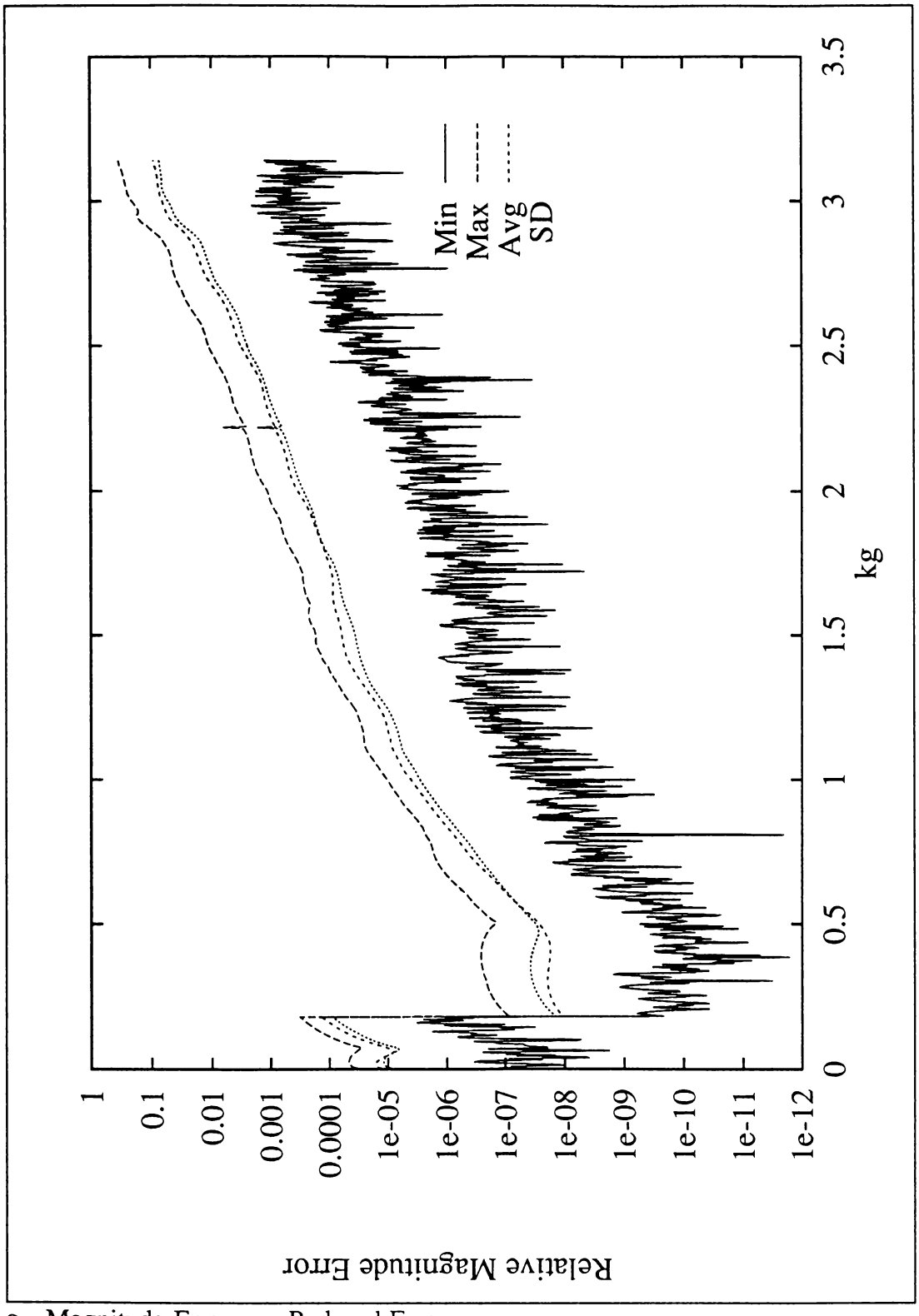

a. Magnitude Errors vs. Reduced Frequency

Figure 3.6.2.4. Hypothetical Source Method Errors: Case 1

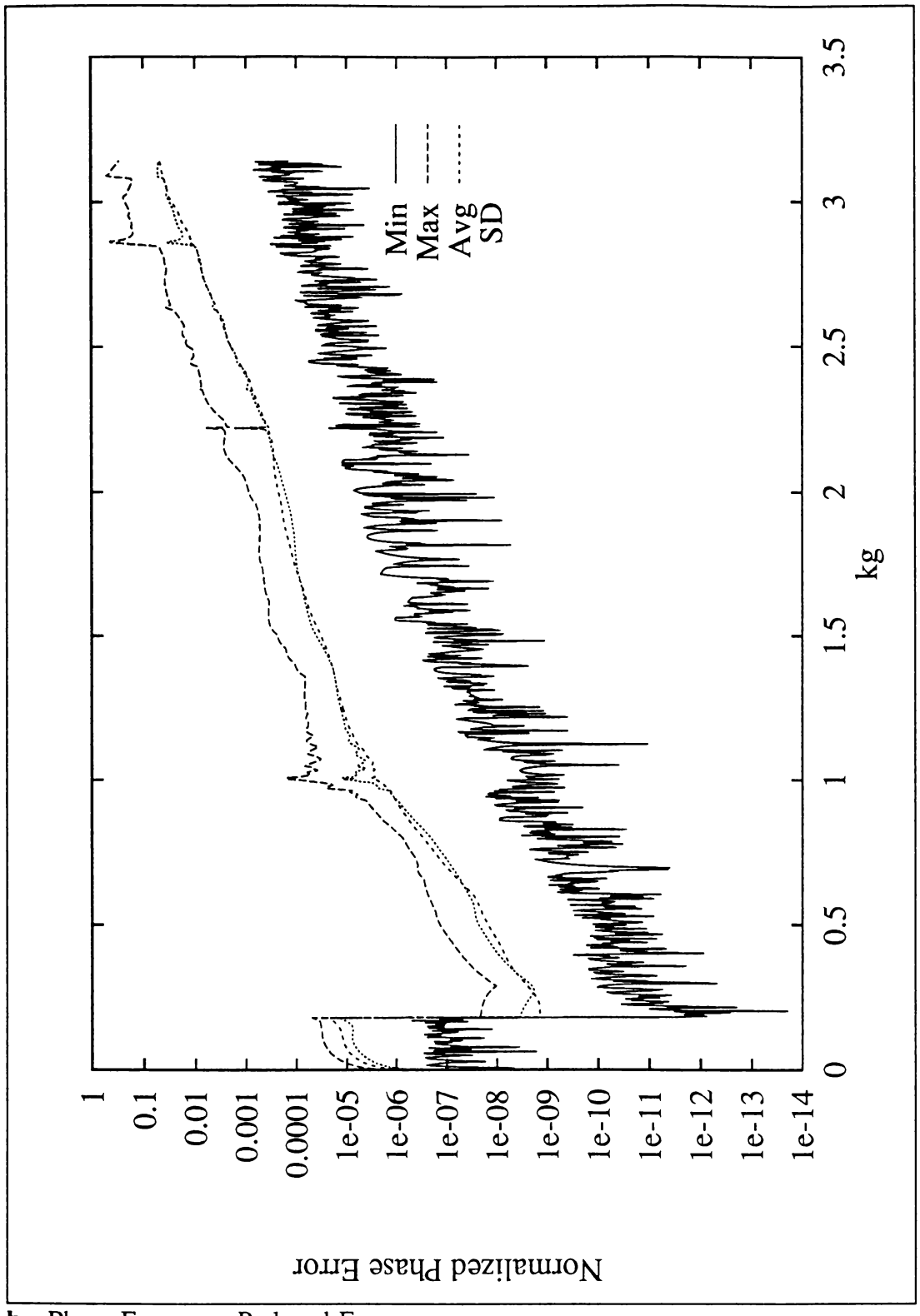

b. Phase Errors vs. Reduced Frequency

Figure 3.6.2.4. (continued)

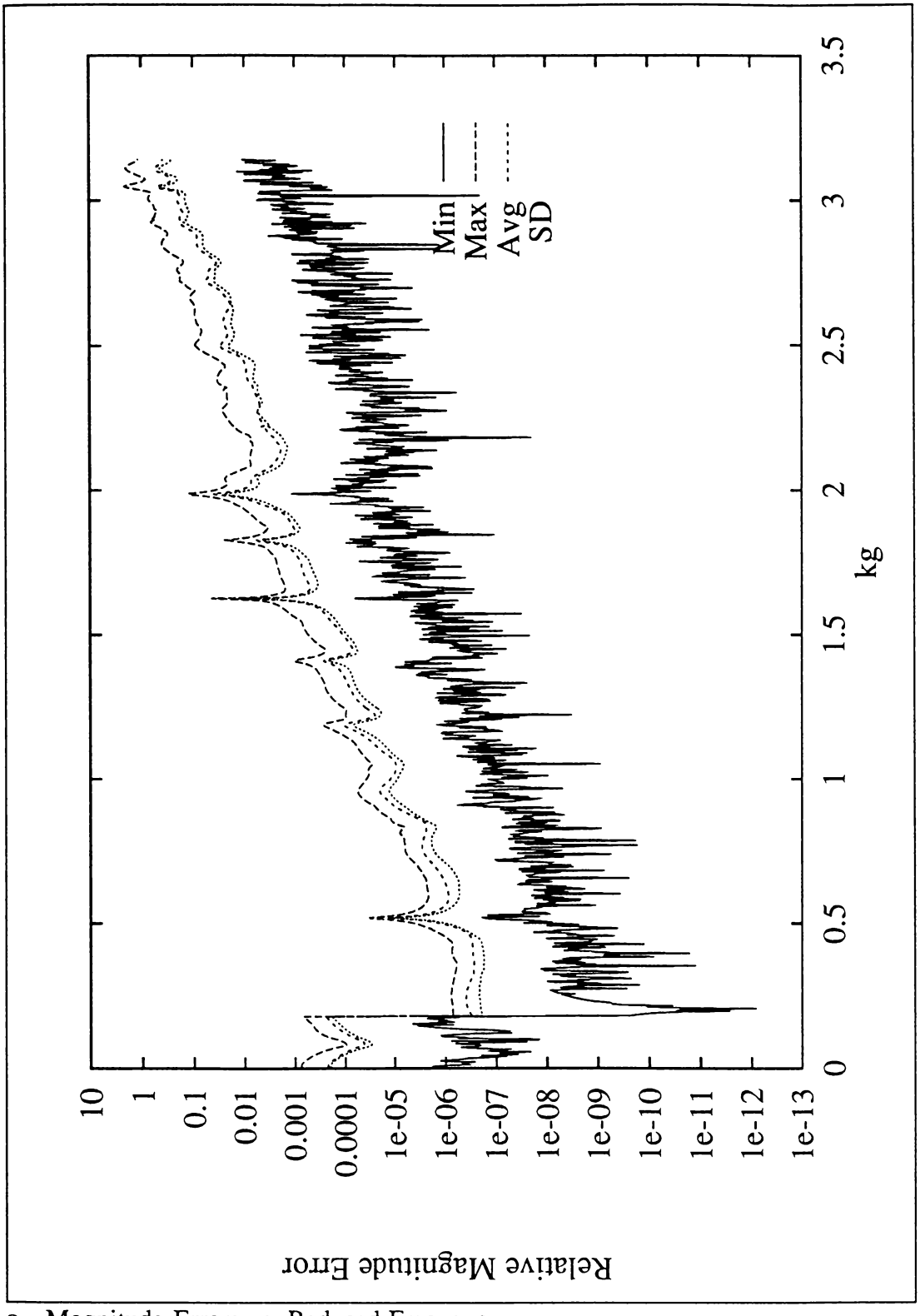

a. Magnitude Errors vs. Reduced Frequency

Figure 3.6.2.5. Hypothetical Source Method Errors: Case 2

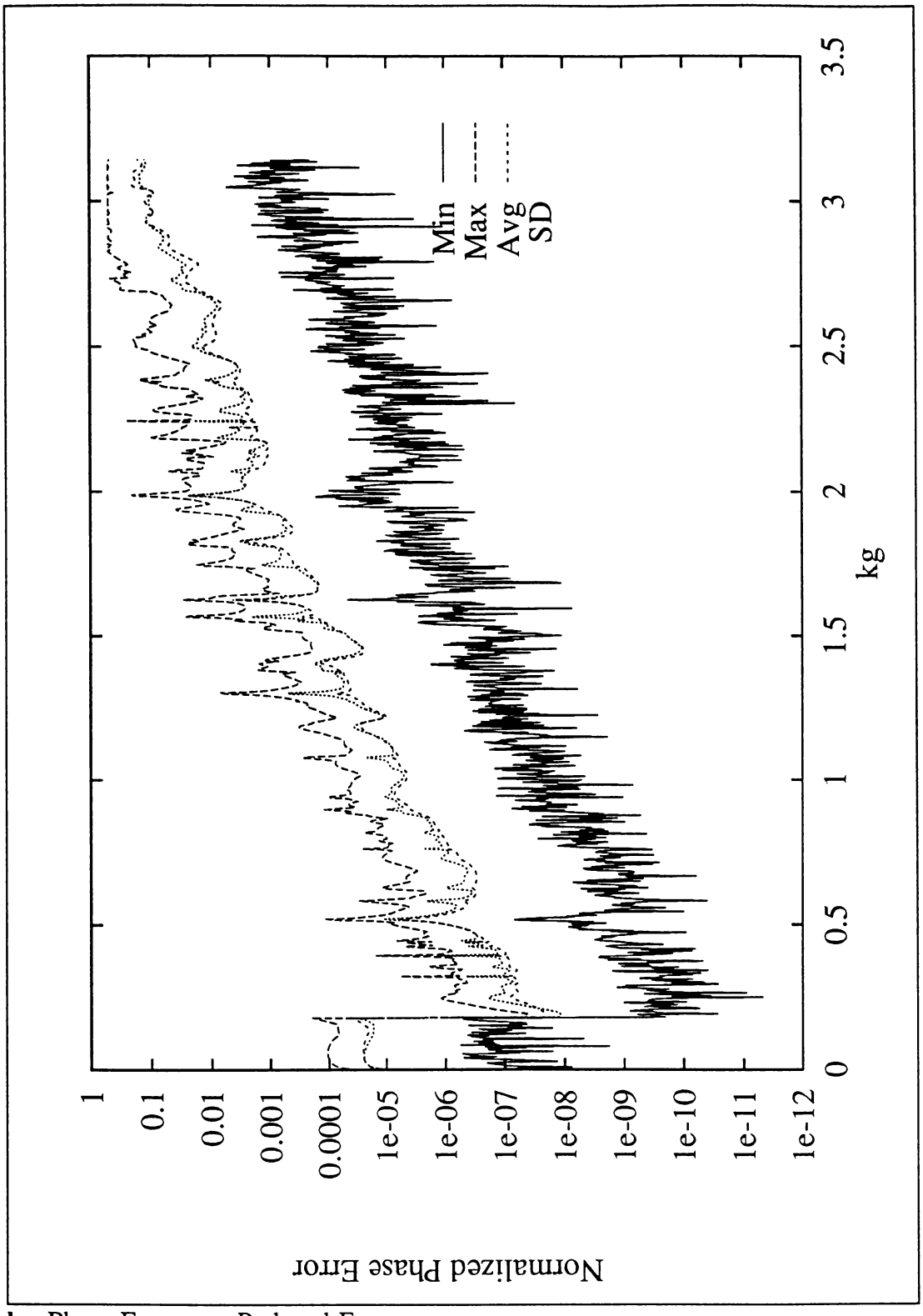

b. Phase Errors vs. Reduced Frequency

Figure 3.6.2.5. (continued)

CHAPTER 5

CONCLUSIONS

For a homogeneous medium in two dimensions, this method can produce accurate solutions of the Helmholtz equation, with the reduced frequency computed relative to the grid resolution approaching the resonant frequency limit. This solution limit has been demonstrated both theoretically and through numerical experiments. For Cartesian meshes, the primary factor in finding the largest allowable value for reduced frequency is the distance between the center and the furthest of the neighboring nodes in the discretization, as was shown for varying aspect ratios. For other discretizations, the limit is determined by the resonant frequency, the frequency that produces homogeneous solutions for the given field.

Important variations in the solution's accuracy, beyond the dependence on the reduced frequency, can be categorized as follows:

Boundary Conditions:
- Incoming plane wave angle
- Multiple plane waves
- Multiple monopole sources
- Evanescent waves

Grid Formation:
- Number of neighboring ("local") nodes
- Aspect ratio

Pseudo-Inversion Process:
- Number and position of Hypothetical Sources
- Number of singular values truncated

The direction of the oncoming plane wave does affect the accuracy of the local discretization for the plane wave examples; however, the accuracy remains high over all

angles, with spikes of increased accuracy as certain axes are crossed. Multiple waves and monopole sources perturb the plane wave solution, while evanescent waves have large errors that converge to the plane wave solution as the Mach number approaches 0.

As the number of local nodes is increased, the solution becomes more accurate in both magnitude and phase. Unfortunately, this may also increase the computing time due to larger banded matrix structures. Varying the aspect ratio reduces the accuracy for the 3x3 case by a magnitude, but as the ratio increases, the size of the increase in the error is bound.

When the number of hypothetical sources is increased, a smoother hypothetical source distribution is generated, more closely approximating the integral of a hypothetical surface, and improving the accuracy of the solution. There is a limit as to how many hypothetical sources significantly improve the accuracy, and use of fewer sources will reduce the discretization time. The radius of the hypothetical sources from the computed node does not affect the solution greatly, except to vary the shape of the hypothetical source strength distributions. The hypothetical source radius has been studied for large values that cause the Green's functions to behave as plane waves. Near field effects have yet to be studied.

The singular value truncation should allow all but the most spurious values. Very small singular values may not be accurate due to their small number of significant digits. When the small singular values are inverted, they can then become very large and potentially incorrect, resulting in adding errors to the system. Eliminating these singular values keeps the system well-behaved. However, eliminating singular values does reduce the accuracy of the pseudo-inverse, so as few singular values as possible should be eliminated.

In comparison with simple differencing techniques, this method gives excellent results, thanks to the "exact" discretization (the only assumption made is that the least-

norm pseudo-inverse provides a better discretization). Some error may be introduced due to the discretization of the "hypothetical surface" (see Appendix 1), as well as homogenous solutions which can corrupt the solution as the resonant frequency is approached.

CHAPTER 6

FURTHER WORK

This thesis demonstrates that the method is a viable discretization technique, but the presented examination of the method is by no means exhaustive. It concentrates on computational experiments to demonstrate the viability of the method, rather than the mathematical theory driving it. Hypotheses have been formed from the results, but rigorous theoretical analysis of the method to show why the method works is still needed. The remainder of this section provides further theoretical questions to be answered and potential extensions of the method to be examined.

6.1 Theoretical Study Options

1. Singular Value Decomposition is not the only technique that could be used. There are other norms that could be used instead, with perhaps even better results.
2. Are there better ways to position the hypothetical source points (ex. two concentric circles)?
3. Should truncating many singular values be trusted, allowing the use of coarser grids?
4. How does the near-field Green's function with a small HS radius affect the discretization? From current analyses the near-field Green's functions do not seem to affect the solution, but do warp the hypothetical source point distribution.

6.2 Application Options

1. When varying the aspect ratio for the test box the least norm discretization seems to place too large a weight on the nearby nodes, and ignore nodes that are further away. This problem needs to be studied more thoroughly.
2. The method needs to be extended to three dimensions would be a simple extension of the method (although use of the tri-diagonal matrix solver would be more complicated).
3. The method could be extended for use with non-homogenous media (that is, varying reduced frequency or varying the speed of sound in a medium). This would facilitate solution of problems such as a better acoustical model for oceans.
4. Non-cartesian grids could be tried, with a routine to seek out points within a specified distance. For example, a hexagonal grid could be easily constructed to function with a tri-diagonal matrix solver.
5. Extension to the time domain should be attempted.

LIST OF REFERENCES

LIST OF REFERENCES

[1] Blitz, J., "Elements of Acoustics", Butterworth & Co., Ltd., Great Britain, © 1964.

[2] Caruthers, J.E., and Dalton, W.N., Unsteady Aerodynamic Response of a Cascade to Nonuniform Inflow, "Journal of Turbomachinery", January 1993, vol. 115, no. 1, p. 79.

[3] Dongarra, J.J., Moler, C.B., Bunch, J.R., and Stewart, G.W., "Linpack User's Guide", SIAM Publication, 1979.

[4] Dowling, A.P. and Williams, J.E.F., "Sound and Sources of Sound", Ellis Horwood Limited, Great Britain, © 1983.

[5] Haberman, R., "Elementary Applied Partial Differential Equations", Prentice-Hall, Inc., New Jersey, © 1983.

[6] Halliday, D., and Resnick, R., "Fundamentals of Physics", John Wiley & Sons, New York, © 1986, p. 325.

[7] Rayleigh, J.W.S., "The Theory of Sound", Dover Pub., New York, © 1945.

[8] Raviprakash, G.K., "A Computational Method for the Analysis of Acoustic Radiation from Turbofan Blades", Doctoral Dissertation, UTK, May 1992.

[9] Lee, D., Carmak, A., Vichnevetsky, R., Eds., "Computational Acoustics: Ocean-Acoustic Models and Supercomputing", Proceedings of the 2nd IMACS Symposium on Computational Acoustics, Elsevier Science Publishing Company, Inc., Netherlands, © 1990.

[10] Strang, G., Linear Algebra and Its Applications, 3rd edition, Harcourt-Brace-Jovanovich, San Diego, 1988.

[11] Caruthers, J.E., Class Notes, Advanced Engineering Acoustics, ES&M 539, Spring 1992.

[12] Morse, P.M., Ingard, K.U., "Theoretical Acoustics", McGraw-Hill, Inc., New York, © 1968.

[13] Caruthers, J.E., "A New Idea for Numerical Discretization of the Helmholtz Equation", UTSI Research Report # UTSI 93/05, April 1993.

[14] Anderson, D.A., Tannehill, J.C., and Pletcher, R.H., "Computational Fluid Mechanics and Heat Transfer", Hemisphere Publishing Corp., New York, © 1984.

[15] Abramowitz, M. and Stegun, I.A., "Handbook of Mathematical Functions", Dover Publications, Inc., New York, 10th printing.

APPENDICES

APPENDIX 1

DERIVATION OF

SINGLE LAYER POTENTIAL REPRESENTATION

This Appendix derives equation (2.1) [11]. Assume any general homogenous region V_o with an exterior E_1 and E_2, with a surface S_o between the region and the exterior, as in figure A1.1 Let $E = E_1 \cup E_2$. Note that $E \cap V_o = 0$. The derivation begins with Green's theorem:

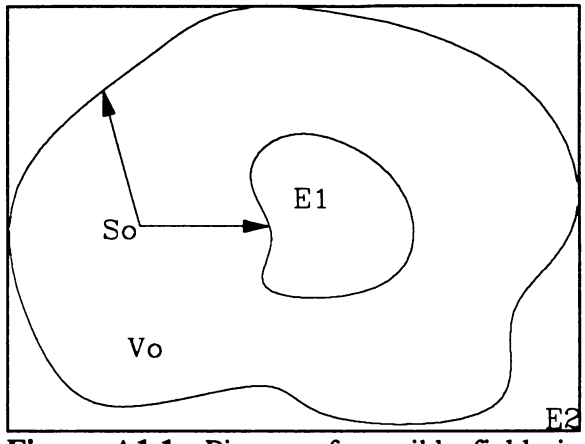

Figure A1.1 Picture of possible fields in question.

$$\int_{V_0} \nabla_0 \cdot \vec{v} dV_0 = \oint_{S_0} \vec{v} \cdot \hat{n} dS_0 \qquad \textbf{(A1.1)}$$

Let $\vec{v} = \nabla_0(\phi(\vec{r}_0) G(\vec{r},\vec{r}_0)) = G(\vec{r},\vec{r}_0)\nabla_0\phi(\vec{r}_0) - \phi(\vec{r}_0)\nabla_0 G(\vec{r},\vec{r}_0)$. Substituting into (A1.1):

$$\int_{V_0} \nabla_0 \cdot (G\nabla_0\phi - \phi\nabla_0 G) dV_0 = \oint_{S_0} (G\nabla_0\phi - \phi\nabla_0 G) \cdot \hat{n} dS_0$$

$$= \oint_{S_0} \left(G\frac{\partial\phi}{\partial n_0} - \phi\frac{\partial G}{\partial n_0} \right) dS_0 \qquad \textbf{(A1.2)}$$

Using Green's Symmetric Identity:

$$\nabla_0\cdot(G\nabla_0\phi - \phi\nabla_0 G) = \nabla_0 G\cdot\nabla_0\phi + G\nabla_0^2\phi - (\nabla_0\phi\cdot\nabla_0 G + \phi\nabla^2 G)$$

$$= G\nabla_0^2\phi - \phi\nabla_0^2 G \tag{A1.3}$$

$$\therefore \int_{V_0}(G\nabla_0^2\phi - \phi\nabla_0^2 G)dV_0 = \oint_{S_0}\left(G\frac{\partial\phi}{\partial n_0} - \phi\frac{\partial G}{\partial n_0}\right)dS_0$$

ϕ satisfies the Helmholtz equation,

$$\nabla_0^2\phi(\vec{r}_0) + k^2\phi(\vec{r}_0) = 0,\ \vec{r}_0 \in V_0 \tag{A1.4}$$

The corresponding Green's function to the Helmholtz equation must solve the equation:

$$\nabla^2 G(\vec{r},\vec{r}_0) + k^2 G(\vec{r},\vec{r}_0) = -\delta(\vec{r} - \vec{r}_0), \qquad \vec{r},\ \vec{r}_0 \in V_0 \tag{A1.5}$$

Assuming this Green's function is known, substituting into (A.1)

$$\int_{V_0}\left[G(\vec{r},\vec{r}_0)\left(-k^2\phi(\vec{r}_0)\right) - \phi(\vec{r}_0)\left(-\delta(\vec{r} - \vec{r}_0) - k^2 G(\vec{r},\vec{r}_0)\right)\right]dV_0$$

$$= \oint_{S_0}\left(G(\vec{r},\vec{r}_0)\frac{\partial\phi(\vec{r}_0)}{\partial n_0} - \phi(\vec{r}_0)\frac{\partial G(\vec{r},\vec{r}_0)}{\partial n_0}\right)dS_0 \tag{A1.6}$$

The volume integral simplifies to $\phi(\vec{r})$. Thus,

$$\phi(\vec{r}) = \oint_{S_0}\left(G\frac{\partial\phi}{\partial n_0} - \phi\frac{\partial G}{\partial n_0}\right)dS_0, \quad \vec{r},\ \vec{r}_0 \in V_0 \tag{A1.7}$$

Remembering that $E \cap V_0 = 0$, let ϕ_E satisfy $\nabla^2\phi_E + k^2\phi_E = 0,\ \vec{r} \in E$.

$$\phi_E(\vec{r}) = \oint_{S_0}\left(G\frac{\partial\phi_E}{\partial n_0} - \phi_E\frac{\partial G}{\partial n_0}\right)dS_0,\ \vec{r} \in E,\ \vec{r}_0 \in V_0 \tag{A1.8}$$

The sound heard in region E cannot come from V, so

$$0 = \oint_{S_0}\left(G\frac{\partial\phi_E}{\partial n_0} - \phi_E\frac{\partial G}{\partial n_0}\right)dS_0, \quad \vec{r}, \vec{r}_0 \in V_0 \tag{A1.9}$$

Combining equation A1.9 with A1.7,

$$\phi(\vec{r}) = \oint_{S_0}\left[G\left(\frac{\partial\phi}{\partial n_0} - \frac{\partial\phi_E}{\partial n_0}\right) - (\phi - \phi_E)\frac{\partial G}{\partial n_0}\right]dS_0, \quad \vec{r}, \vec{r}_0 \in V_0 \tag{A1.10}$$

To simplify this, ϕ_E is chosen to equal ϕ on the surface, because it is an arbitrary value. When we let

$$\sigma(\vec{r}_0) = \frac{\partial\phi}{\partial n_0} - \frac{\partial\phi_E}{\partial n_0}, \ \vec{r}_0 \in V_0 \tag{A1.11}$$

the equation can be simplified to the single layer potential equation:

$$\phi(\vec{r}) = \oint_{S_0}\sigma(\vec{r}_0)G(\vec{r},\vec{r}_0)dS_0, \quad \vec{r}, \vec{r}_0 \in V_0 \tag{A1.12}$$

or discretized as

$$\phi(\vec{r}) = \sum_{i=1}^{i=n}\sigma(r_i, \tfrac{2\pi i}{n})G(r, \theta; r_i, \tfrac{2\pi i}{n}), \ \vec{r} \in V_0 \tag{A1.13}$$

with $[r_i, \theta]$ on S_0, in which case S_0 is a circle. The σ_i's are referred to in this thesis as hypothetical sources, and n is the number of the sources.

The values for σ_i are unknown. With this discretization, the Green's function equations have been chosen, and the values for the boundary, σ_i, are computed. Equation (A1.13) can be rewritten in tensor notation as

$$\phi(\vec{r}) = \sigma_i G_i, \ i = 1 \ to \ n \tag{A1.14}$$

APPENDIX 2

2-D BOUNDARY VALUE TEST PROBLEM PLOTS

To see beyond the statistical determination of the accuracy of the solutions, magnitude and phase contour plots of the different solution methods follow for comparison. Case 1 from section 3.6 was computed for reduced frequencies of k = 1 and k = 2. The exact (analytical), HSM, 5 and 9 Node FD schemes resulting interpolated fields are plotted (figs. A2.1-4). The 5 and 9 Node FD schemes were also computed for doubly dense meshes, and the results are also included. Case 2 was computed for frequencies of k = 1 and k = 2, but only the exact and HSM solution of these fields is included (figs. A2.5-8).

From the plots, it is easy to see that even when the grid's number of nodes is doubled, the finite difference method contains large errors for higher frequencies, while the HSM produces very accurate results.

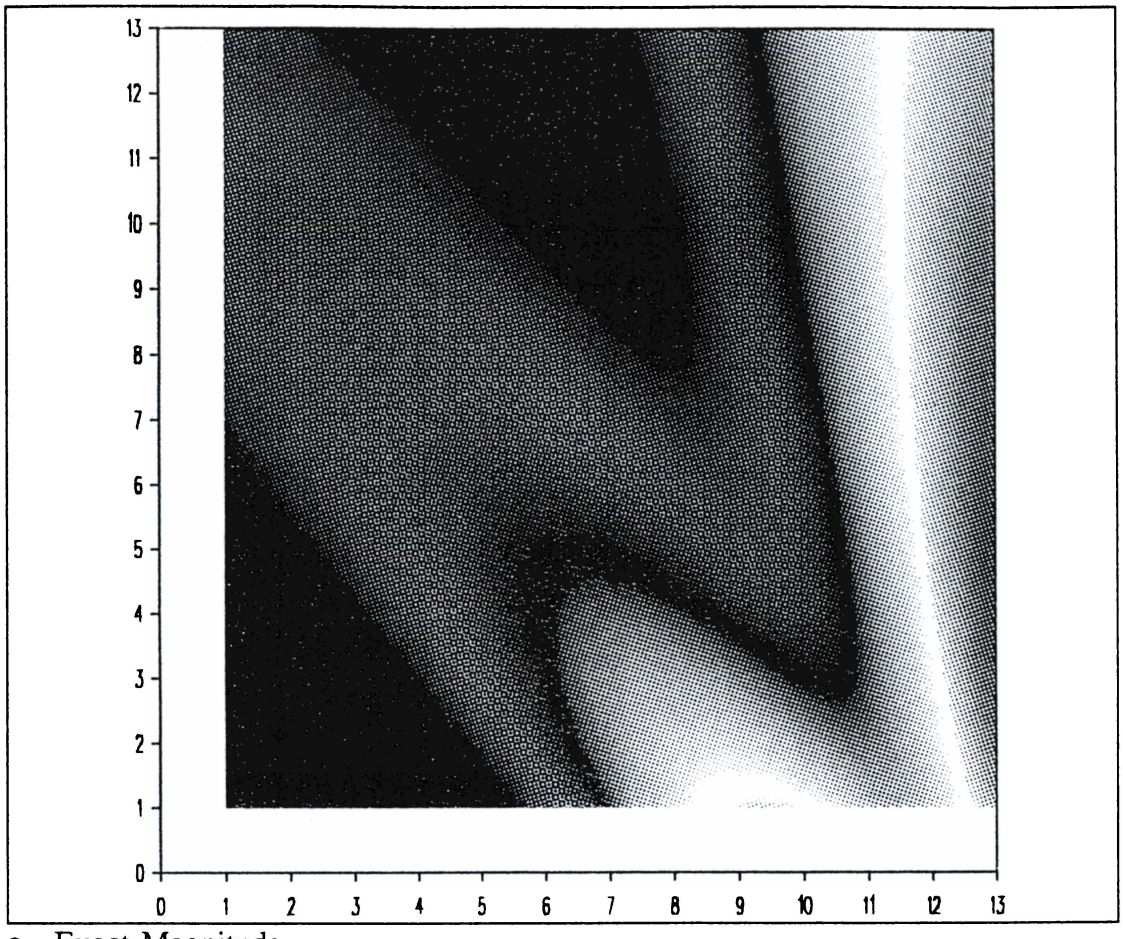

a. Exact Magnitude

Figure A2.1. Magnitude Plots for Case 1, $k_g = 1$

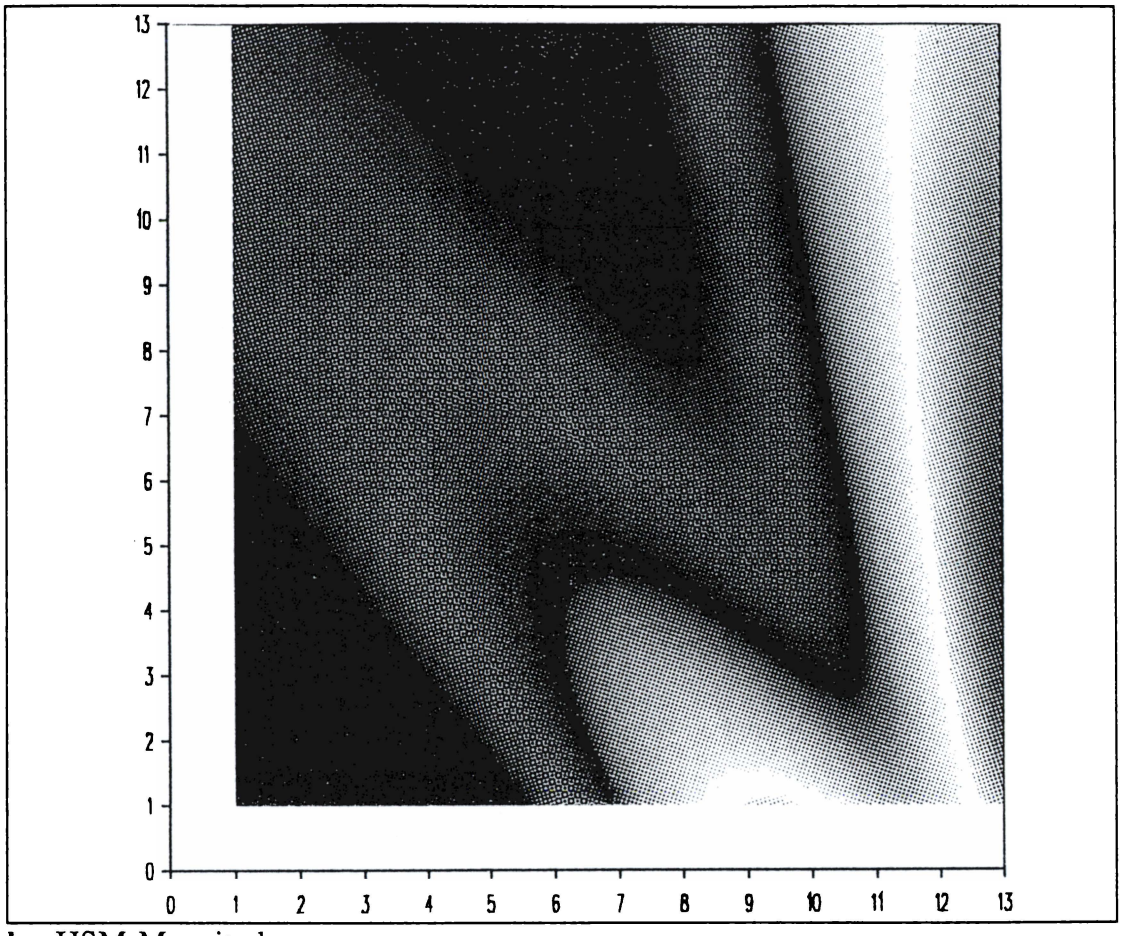

b. HSM Magnitude

Figure A2.1. (continued)

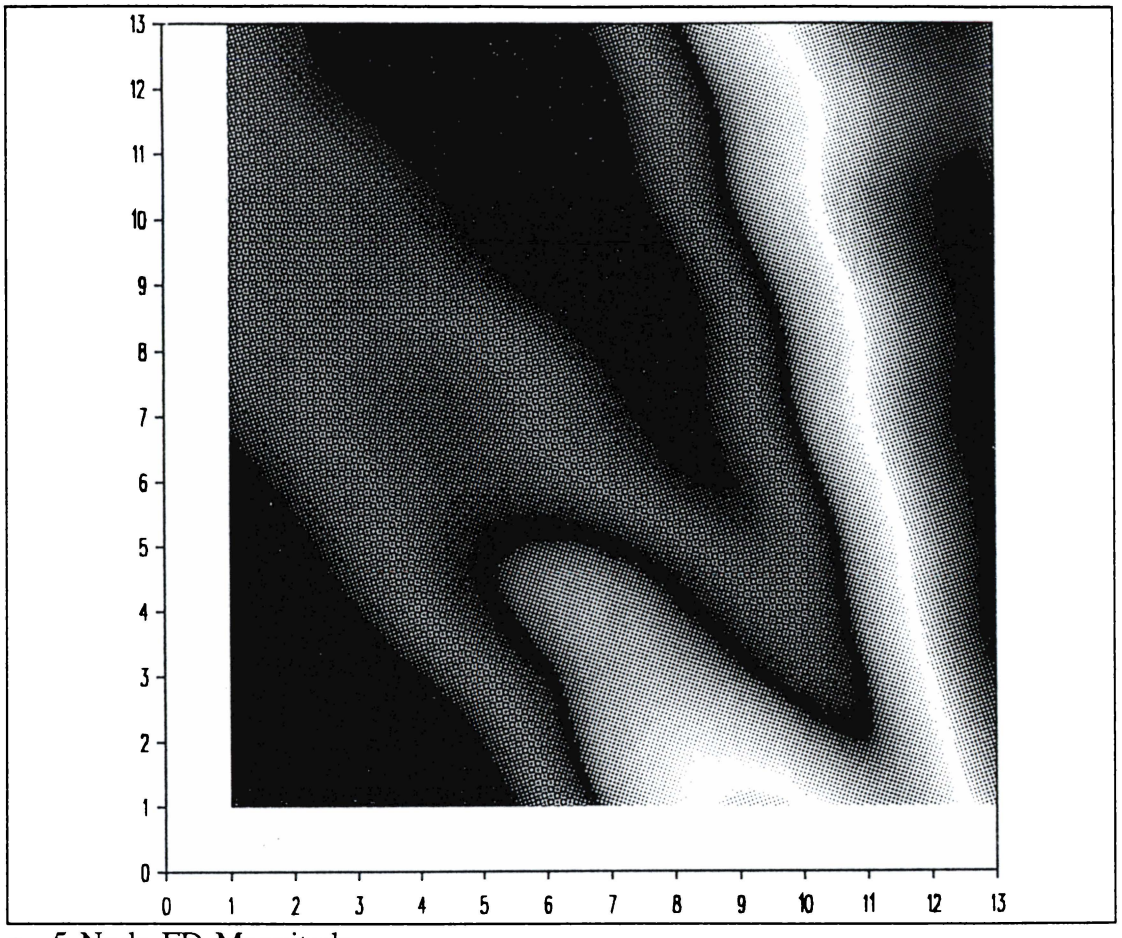

c. 5 Node FD Magnitude

Figure A2.1. (continued)

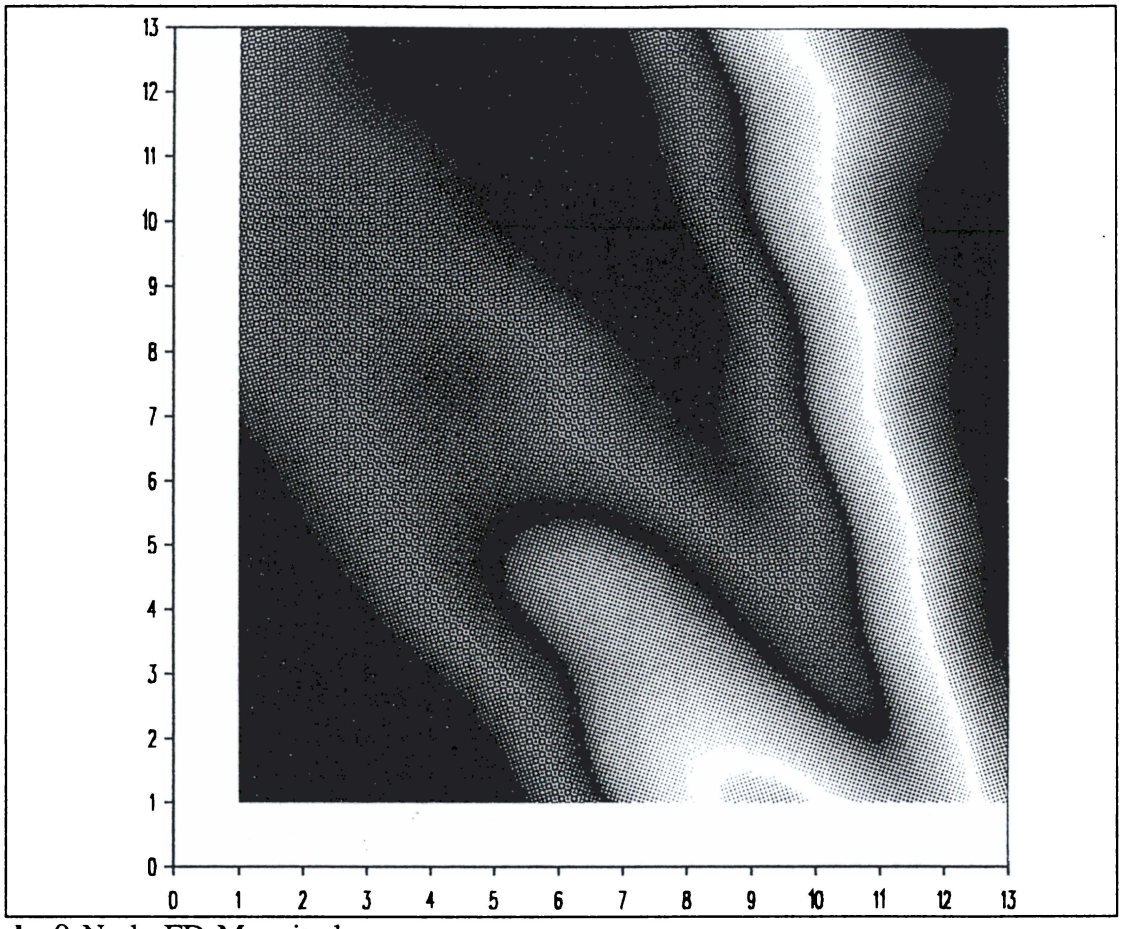

d. 9 Node FD Magnitude

Figure A2.1. (continued)

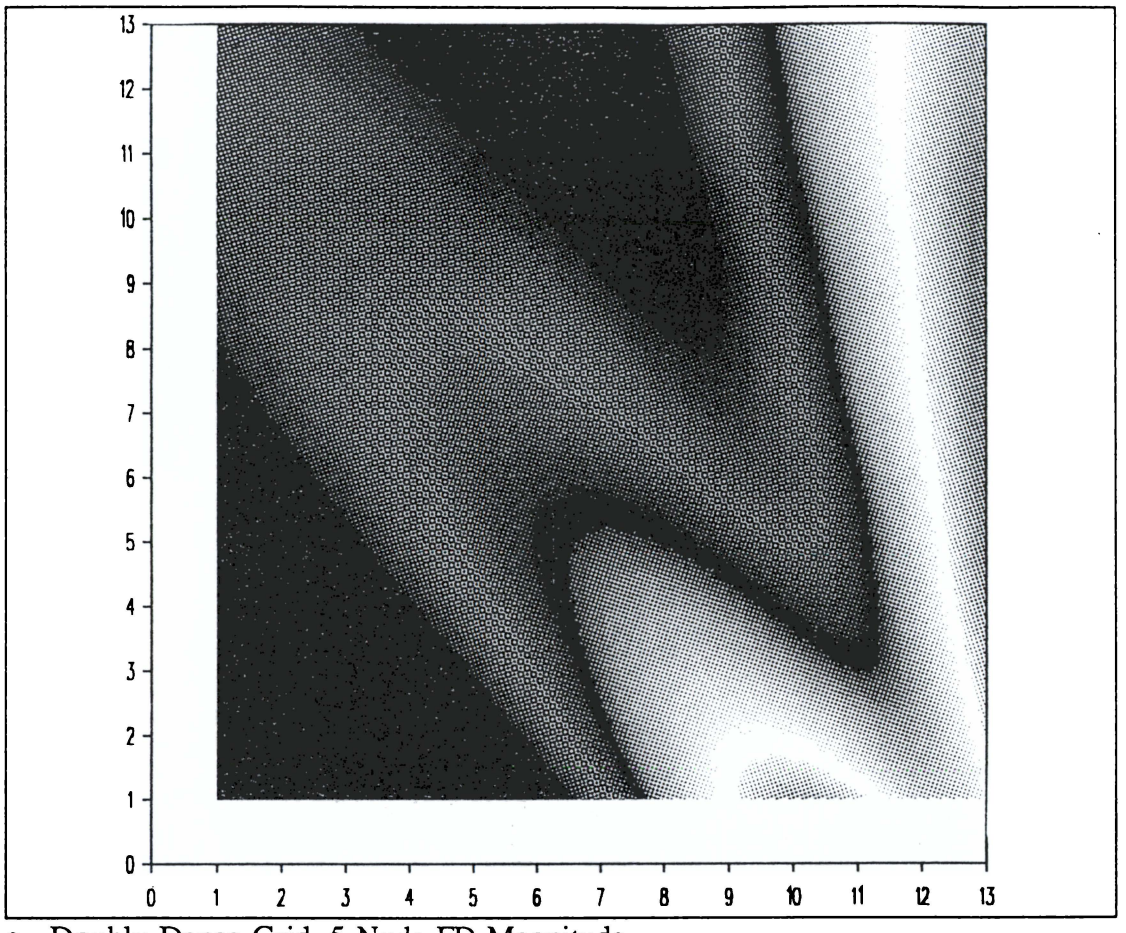

e. Doubly Dense Grid, 5 Node FD Magnitude

Figure A2.1. (continued)

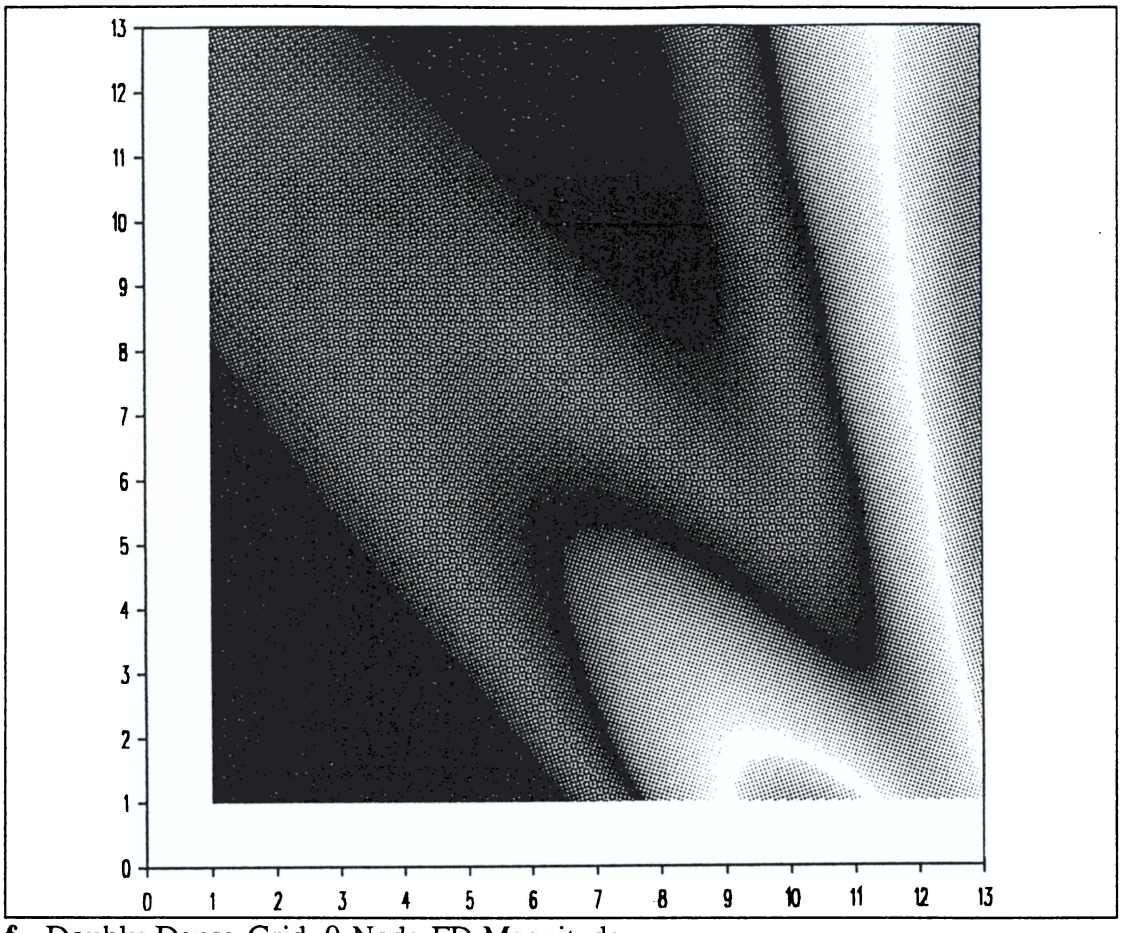

f. Doubly Dense Grid, 9 Node FD Magnitude

Figure A2.1. (continued)

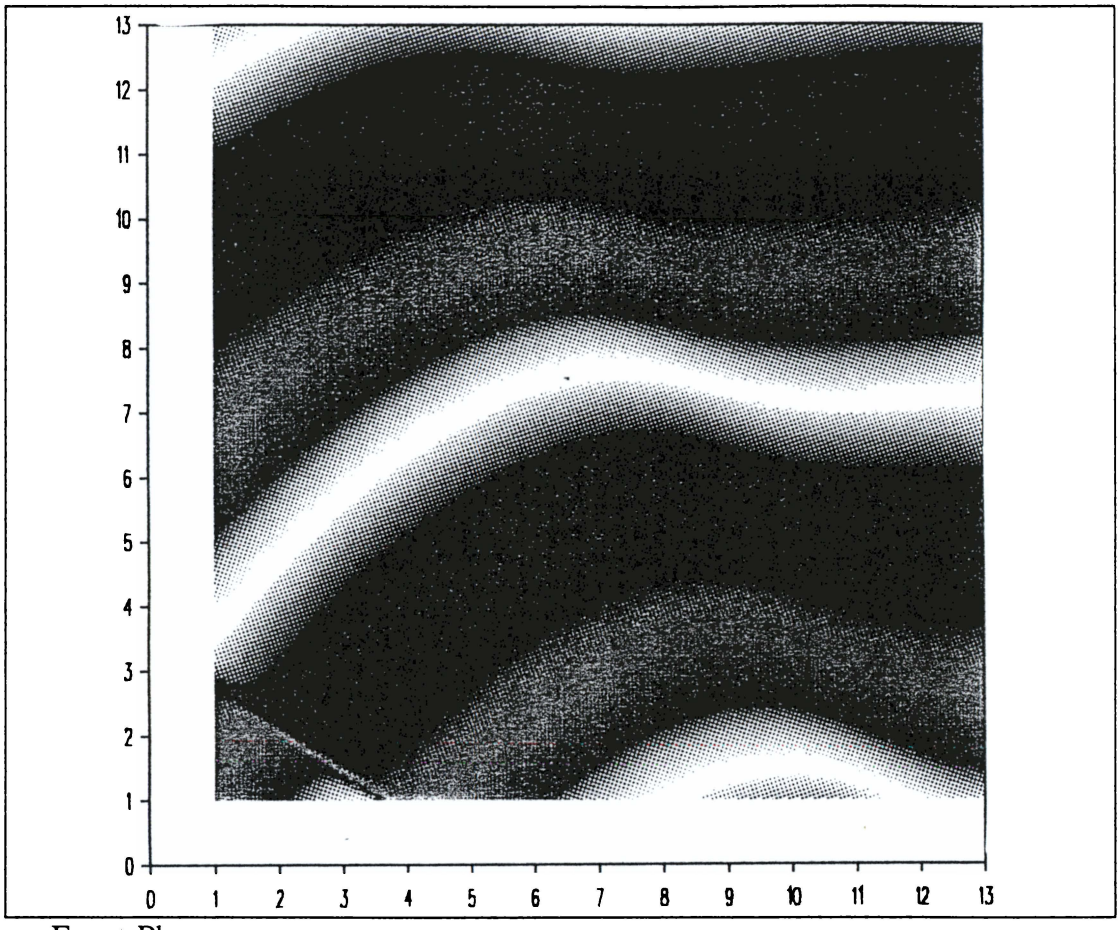

a. Exact Phase

Figure A2.2. Phase Plots for Case 1, $k_g = 1$

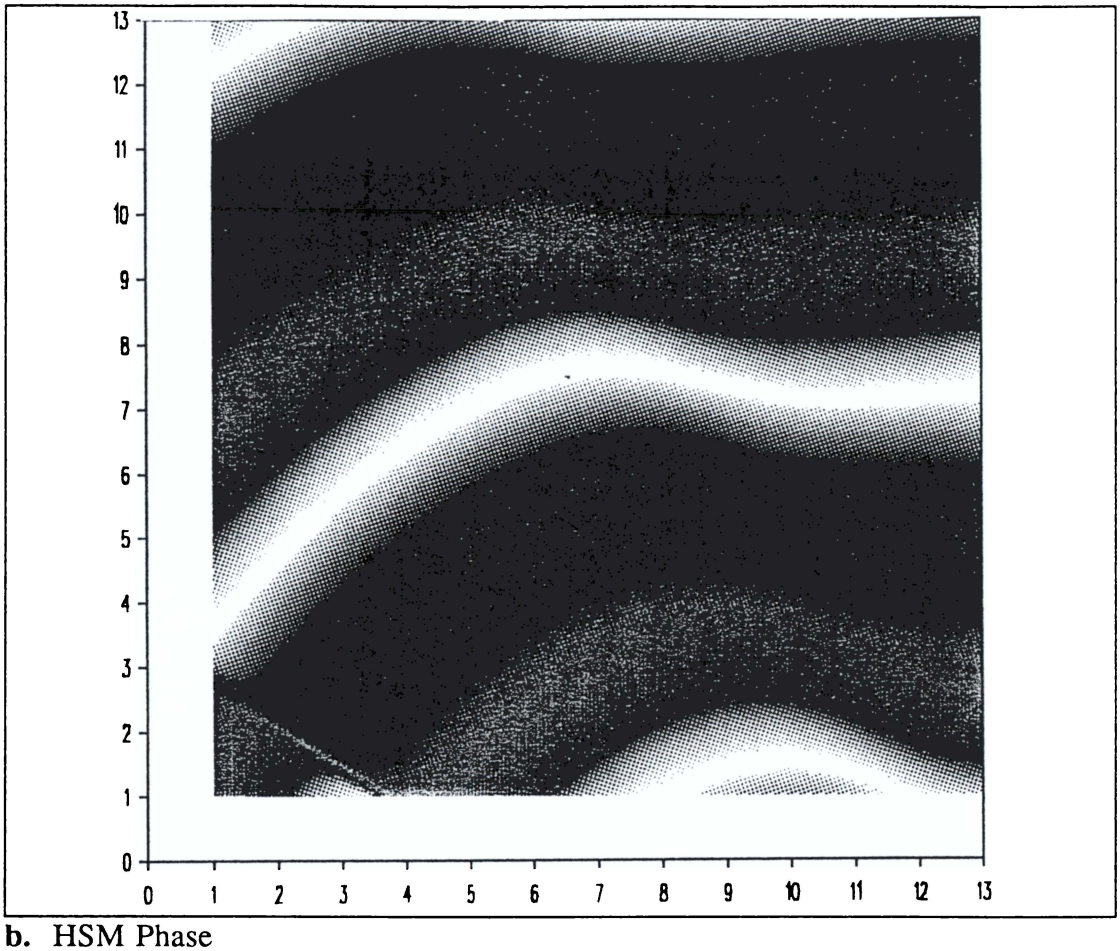

b. HSM Phase

Figure A2.2. (continued)

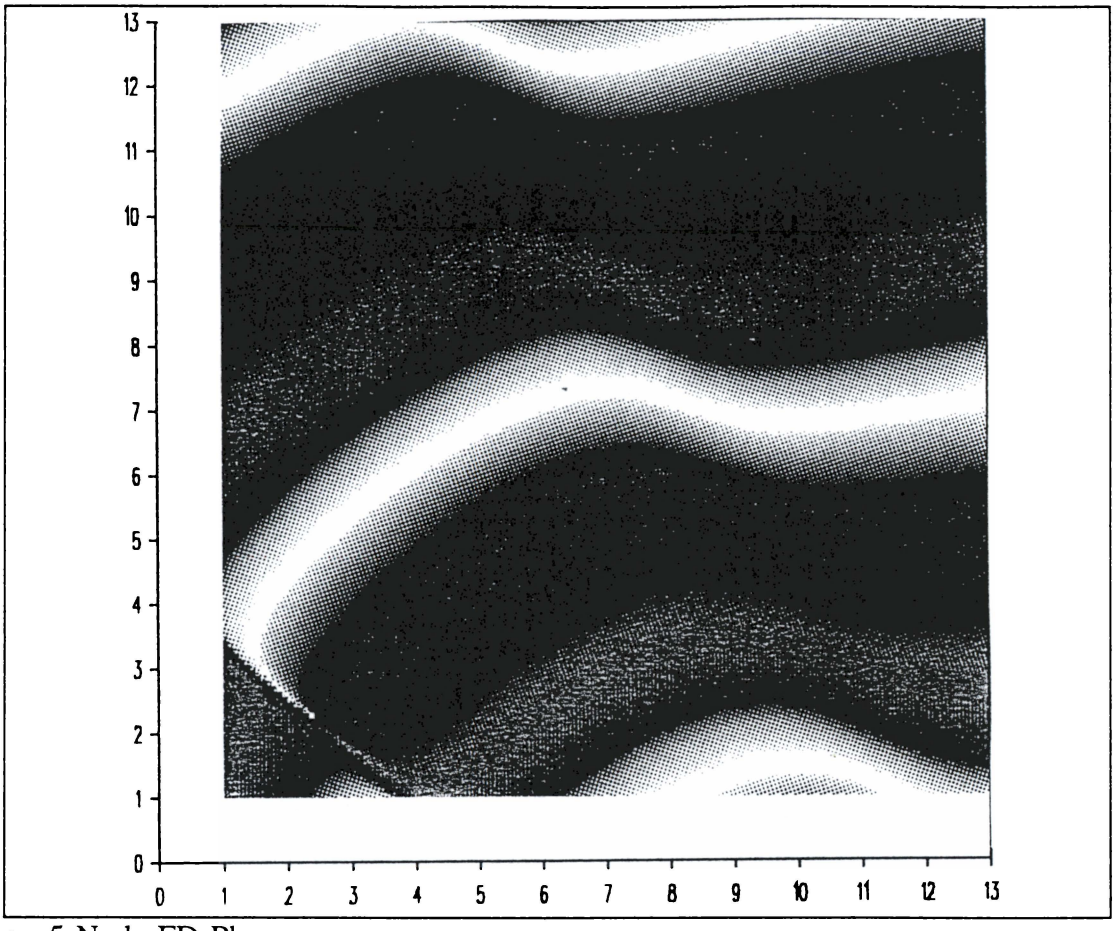

c. 5 Node FD Phase

Figure A2.2. (continued)

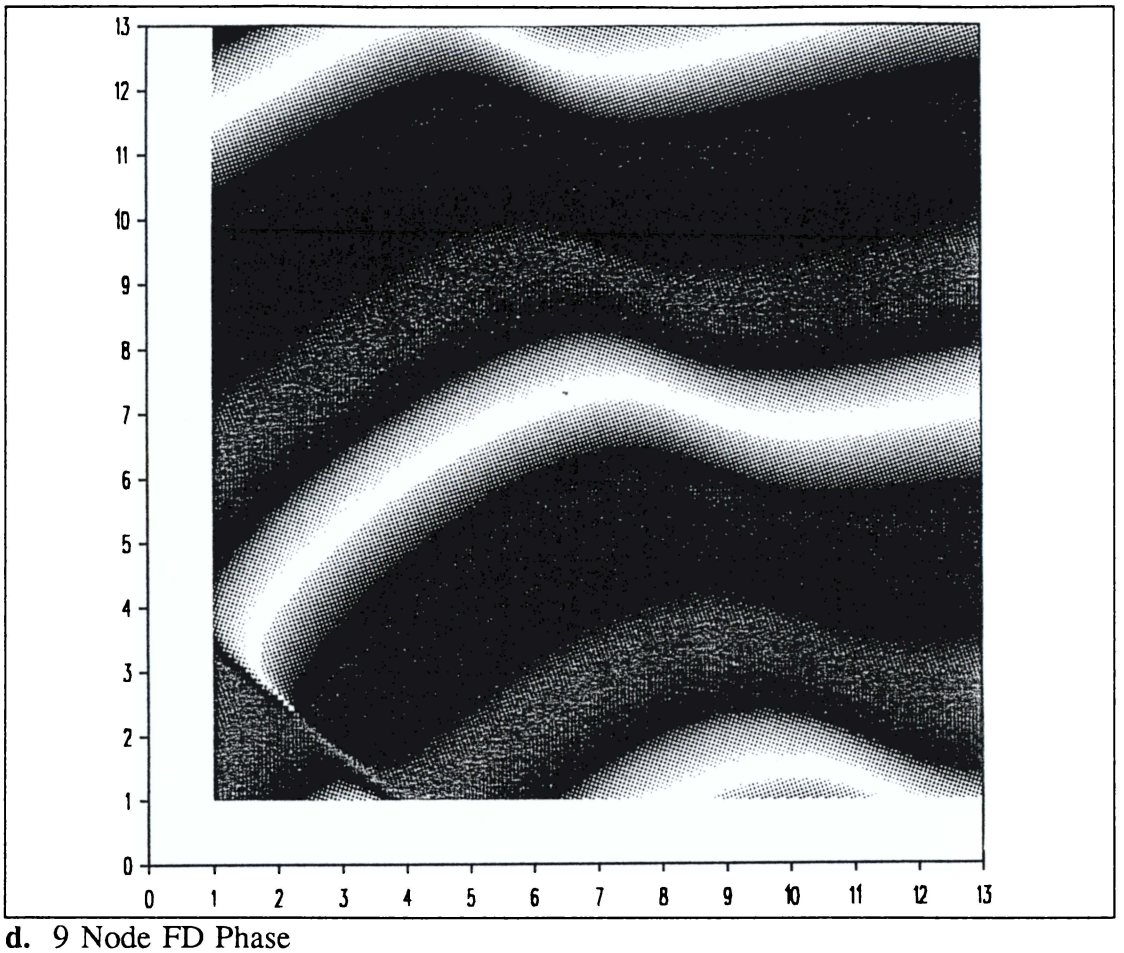

d. 9 Node FD Phase

Figure A2.2. (continued)

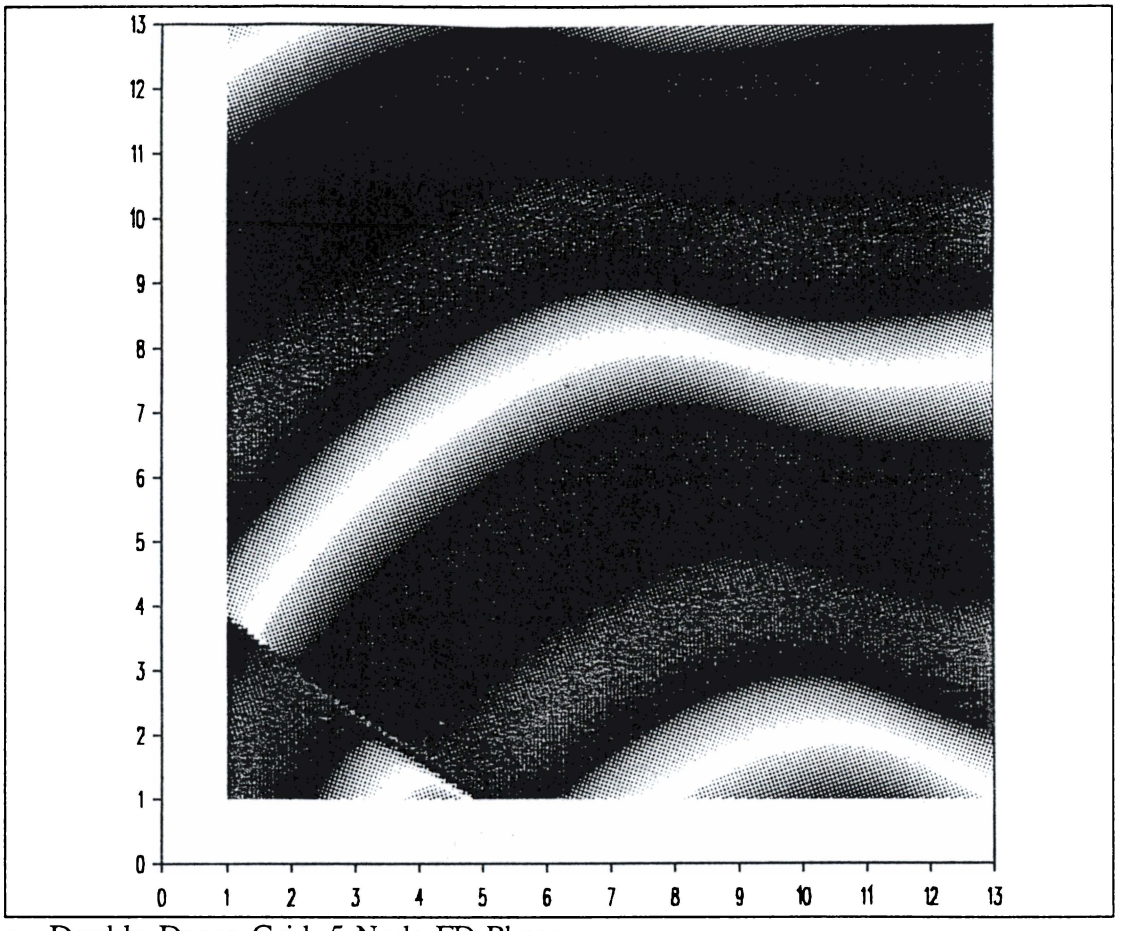

e. Doubly Dense Grid, 5 Node FD Phase

Figure A2.2. (continued)

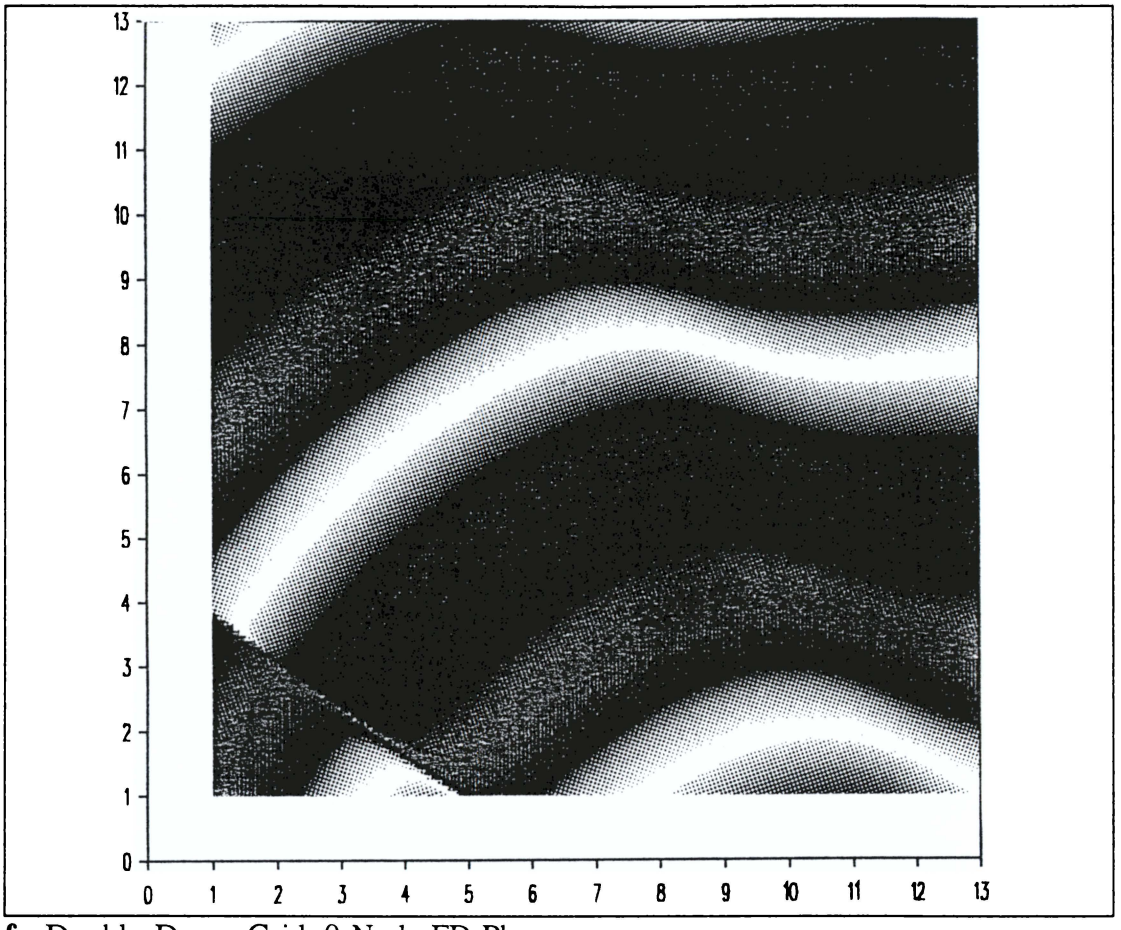

f. Doubly Dense Grid, 9 Node FD Phase

Figure A2.2. (continued)

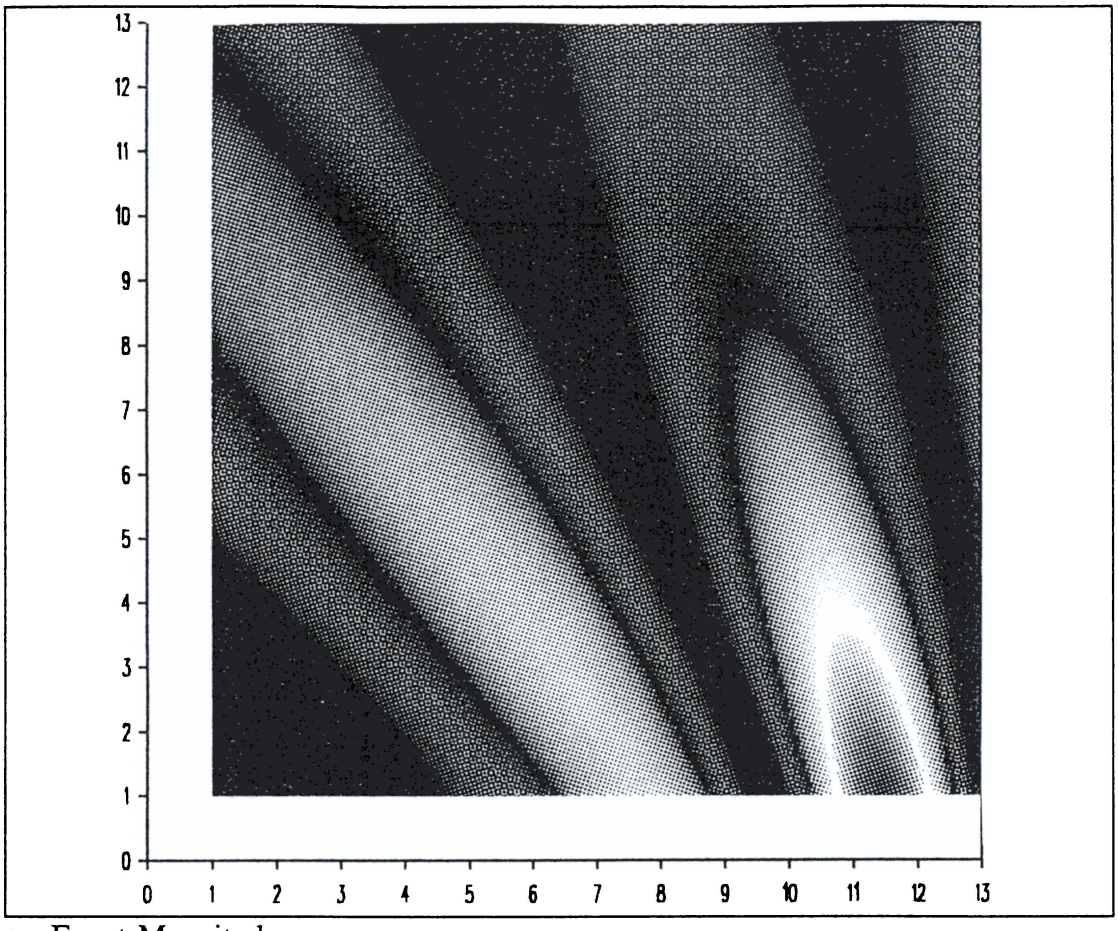

a. Exact Magnitude

Figure A2.3. Magnitude Plots for Case 1, $k_g = 2$

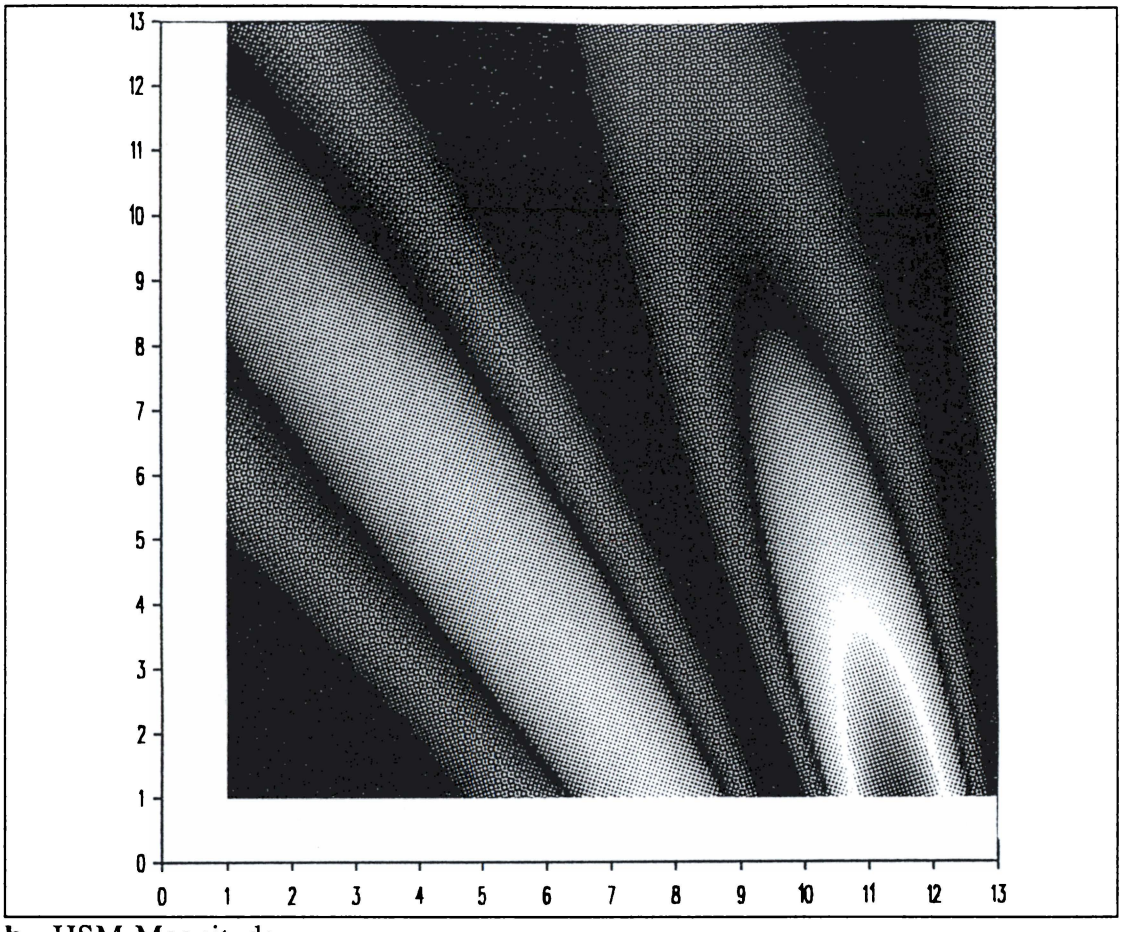

b. HSM Magnitude

Figure A2.3. (continued)

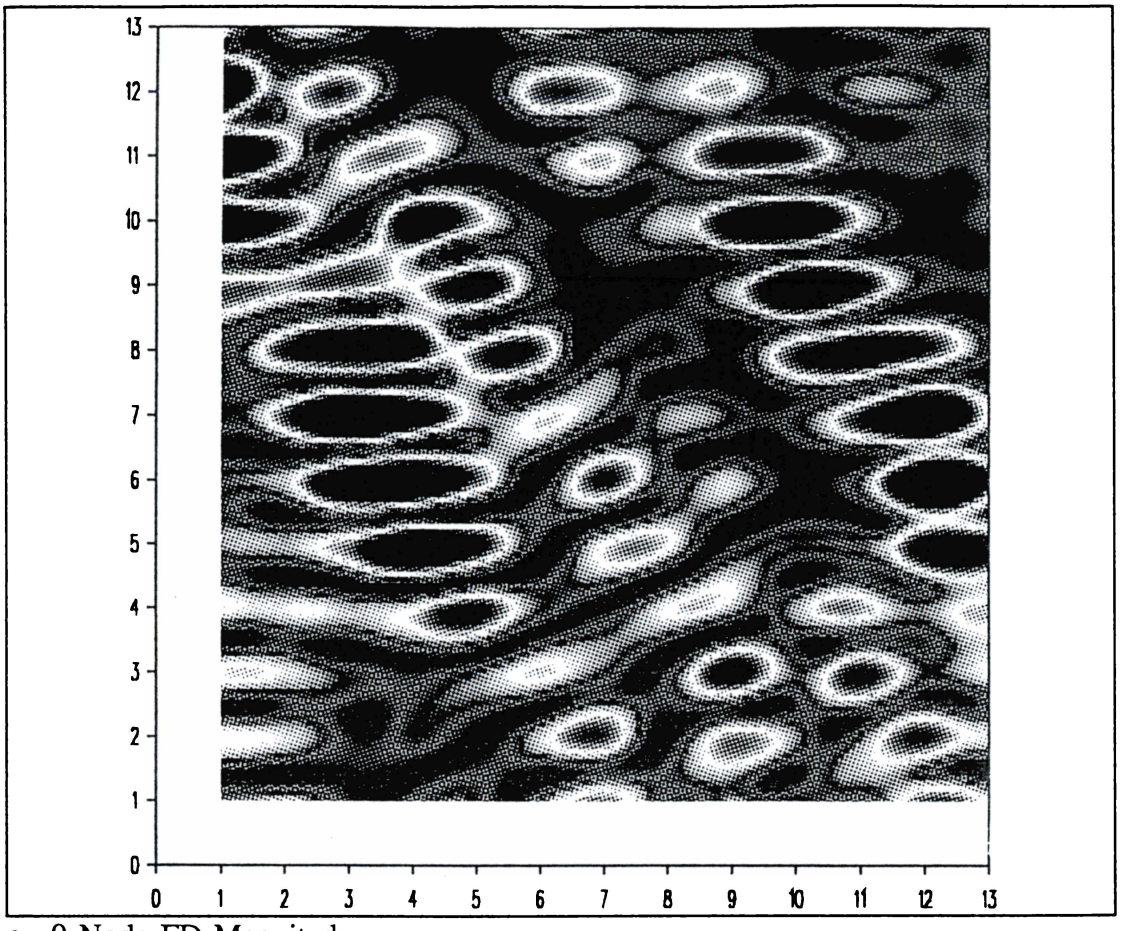

c. 9 Node FD Magnitude

Figure A2.3. (continued)

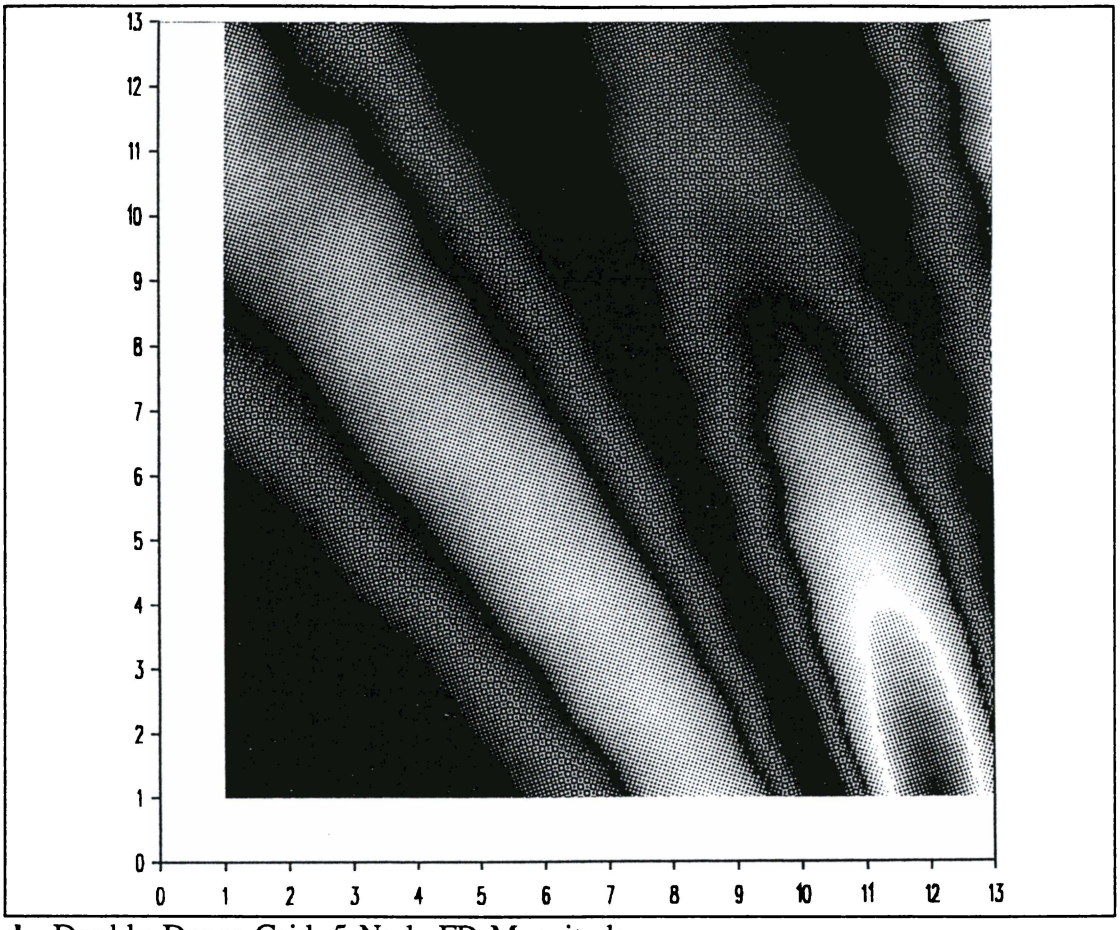

d. Doubly Dense Grid, 5 Node FD Magnitude

Figure A2.3. (continued)

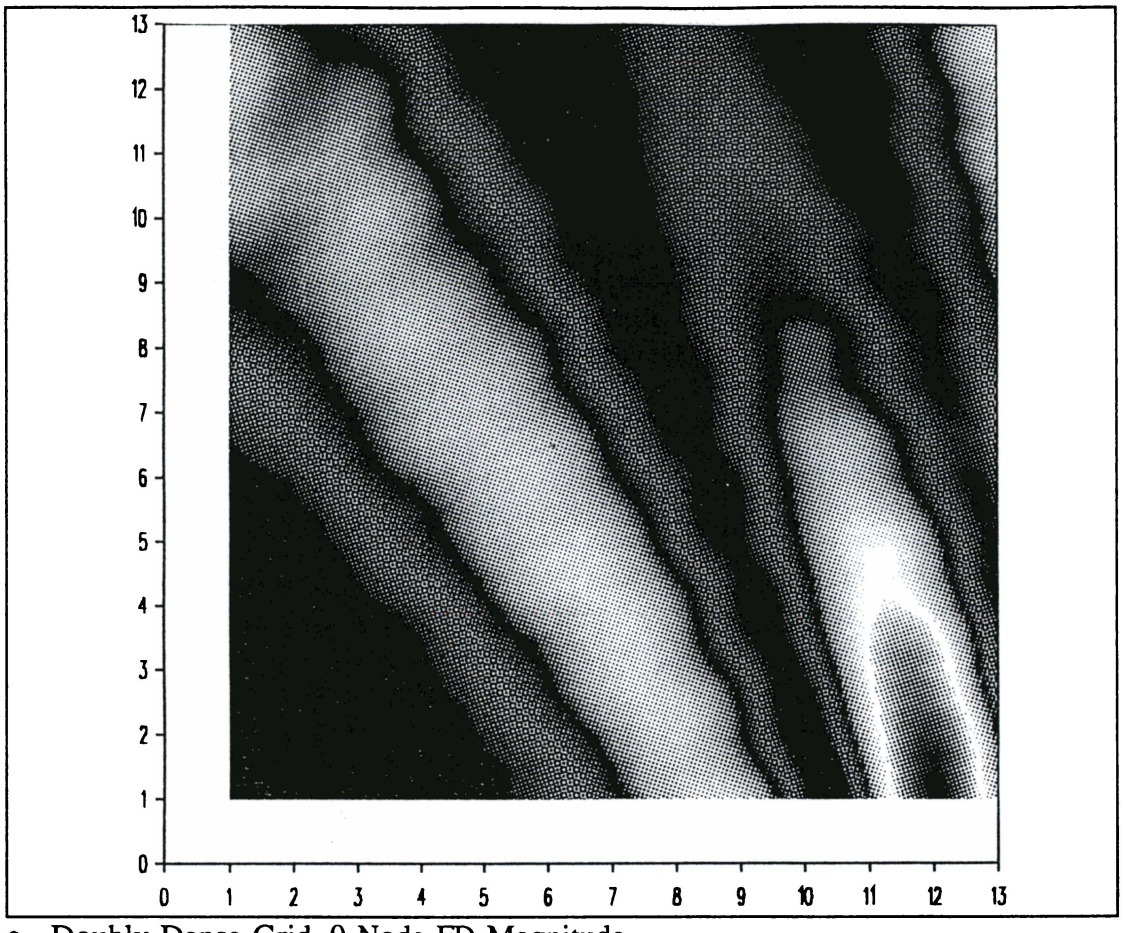

e. Doubly Dense Grid, 9 Node FD Magnitude

Figure A2.3. (continued)

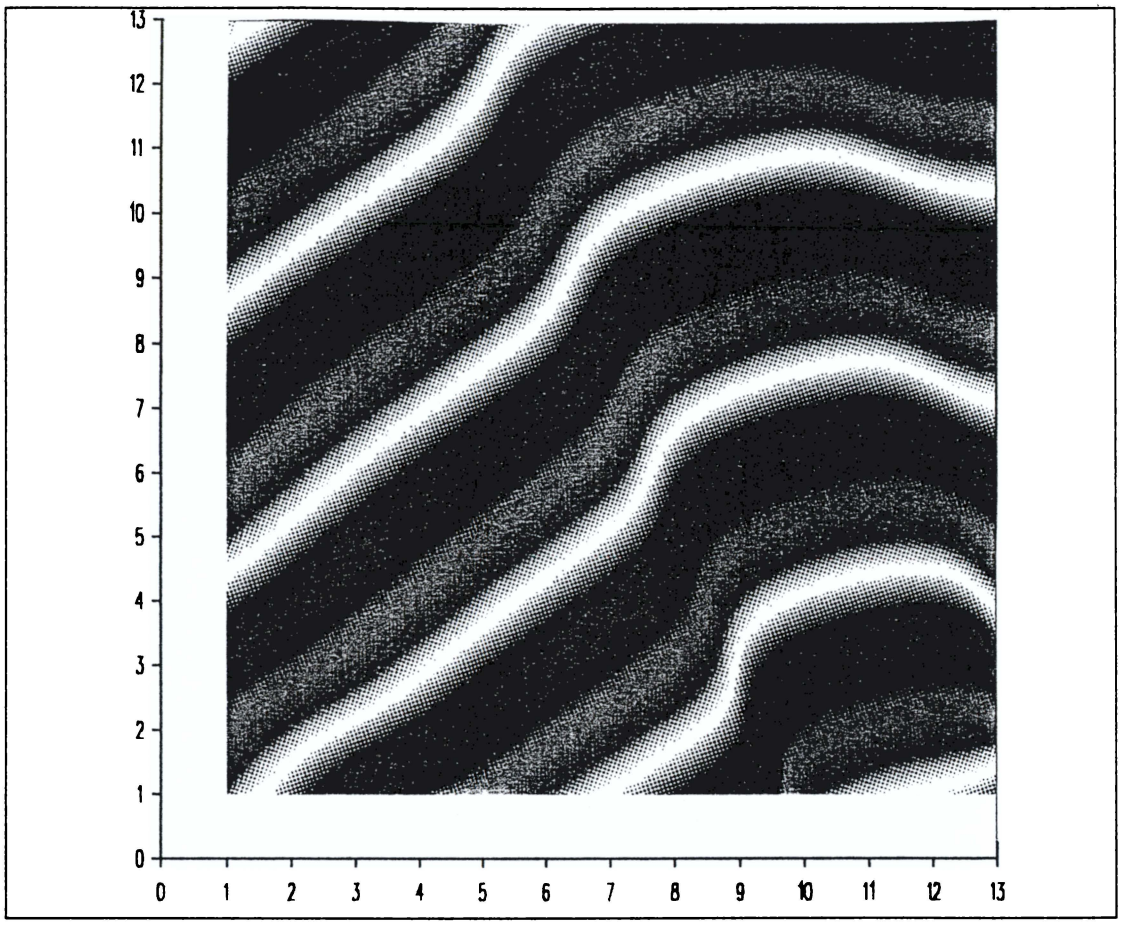

a. Exact Phase

Figure A2.4. Phase Plots for Case 1, $k_g = 2$

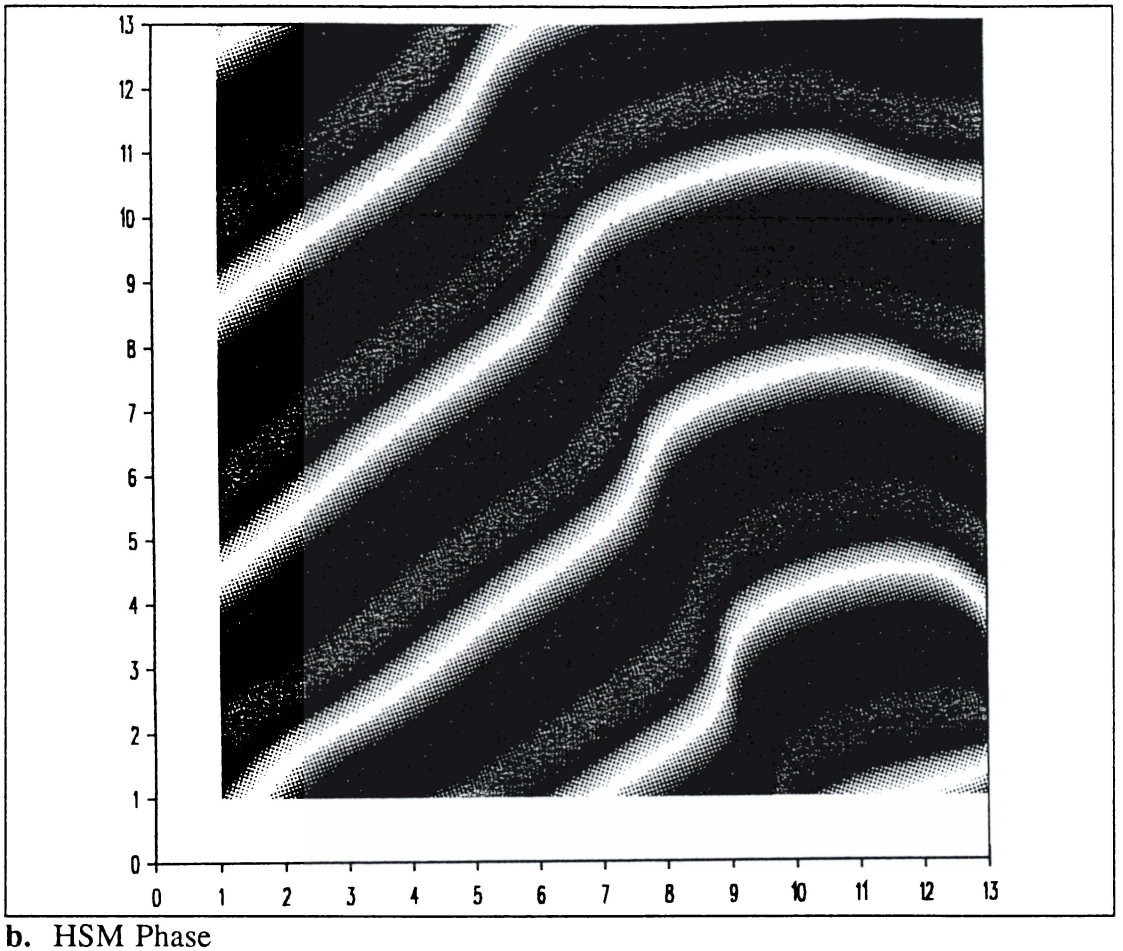

b. HSM Phase

Figure A2.4. (continued)

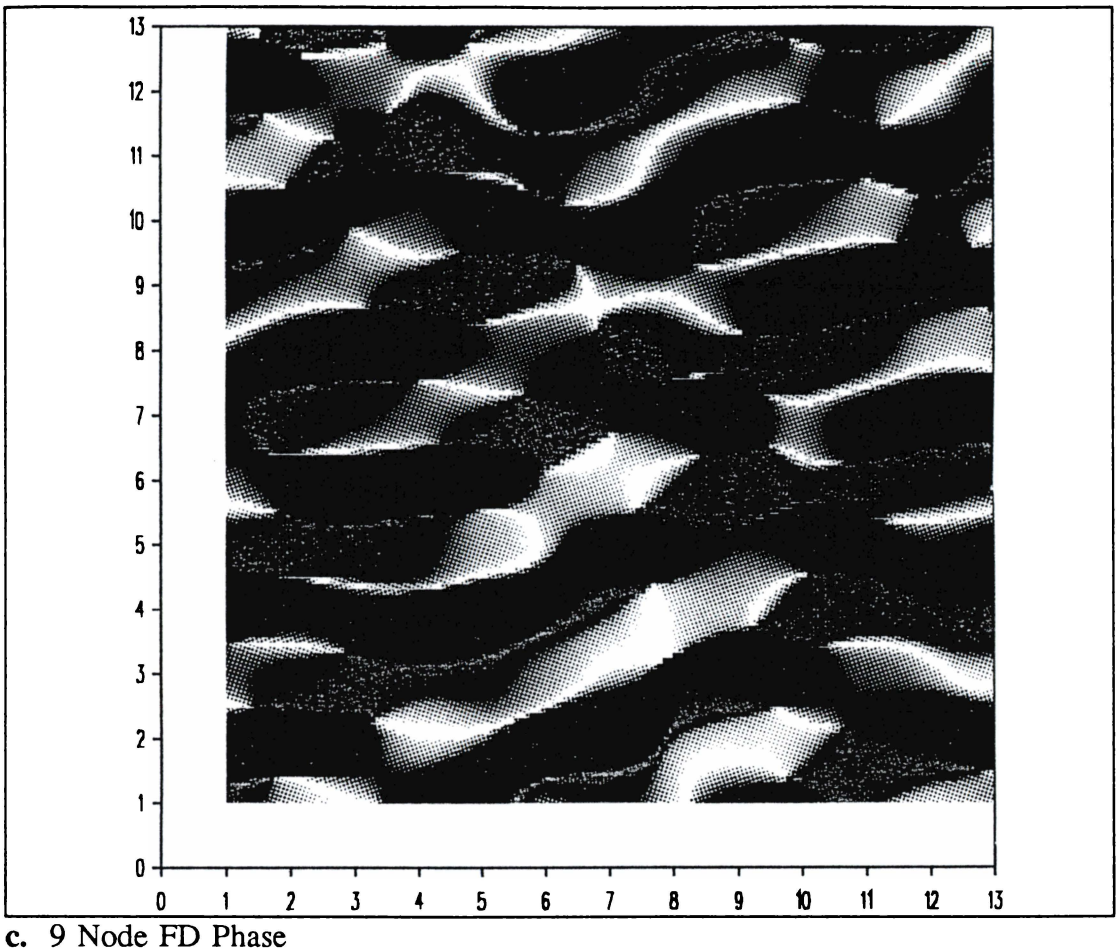

c. 9 Node FD Phase

Figure A2.4. (continued)

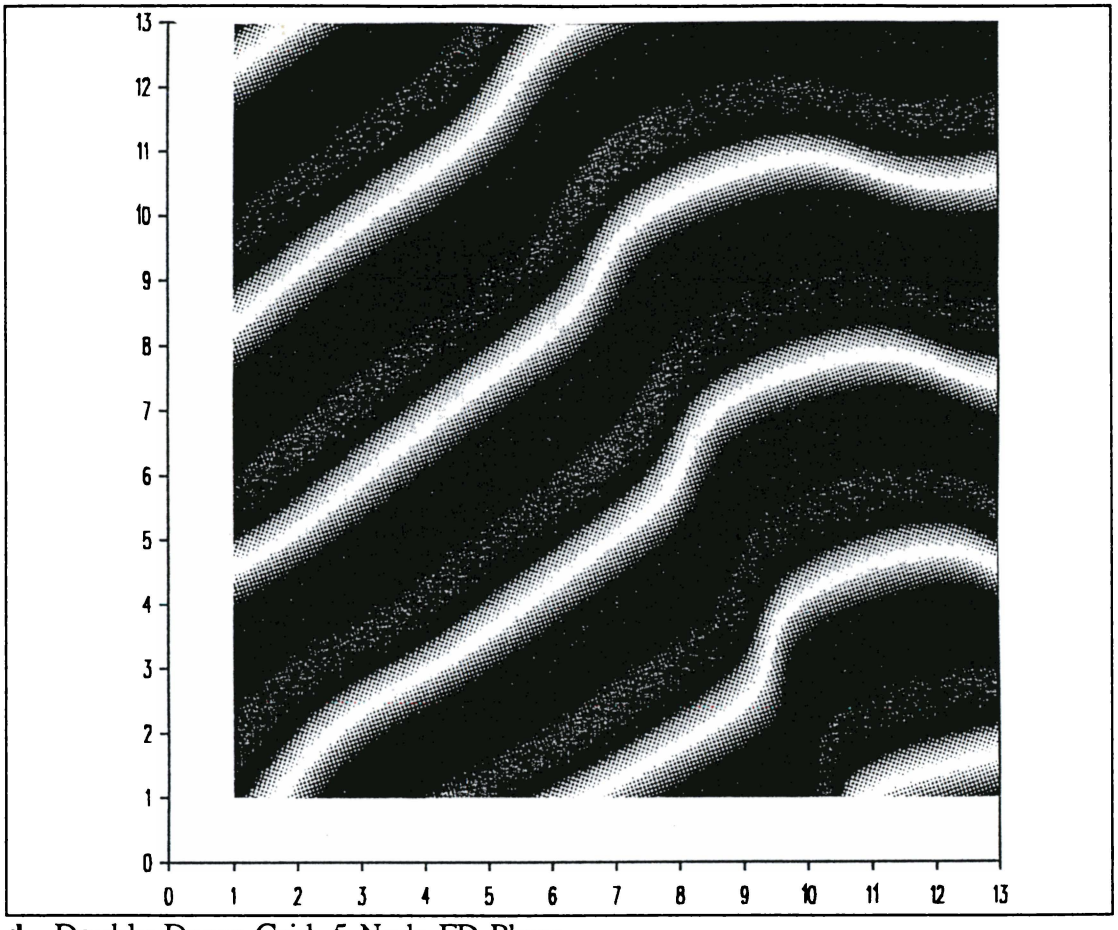

d. Doubly Dense Grid, 5 Node FD Phase

Figure A2.4. (continued)

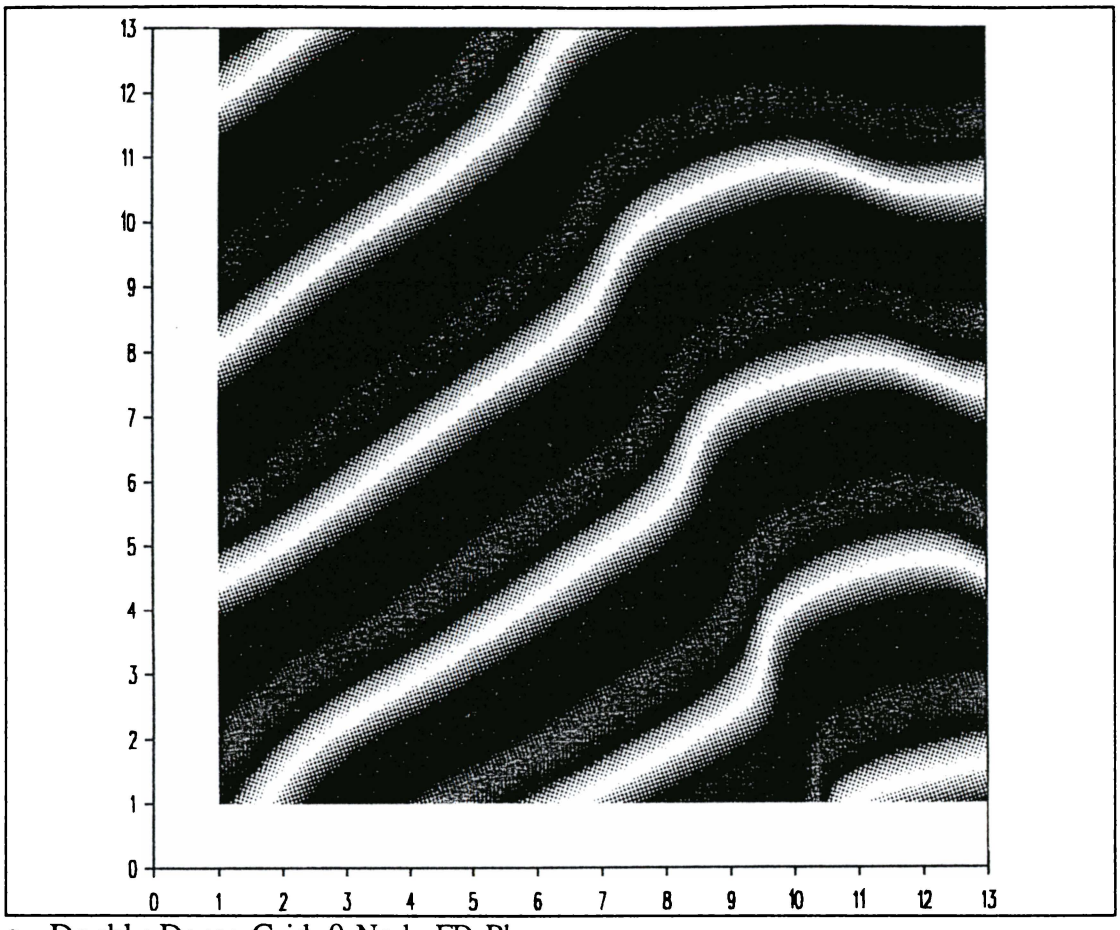

e. Doubly Dense Grid, 9 Node FD Phase

Figure A2.4. (continued)

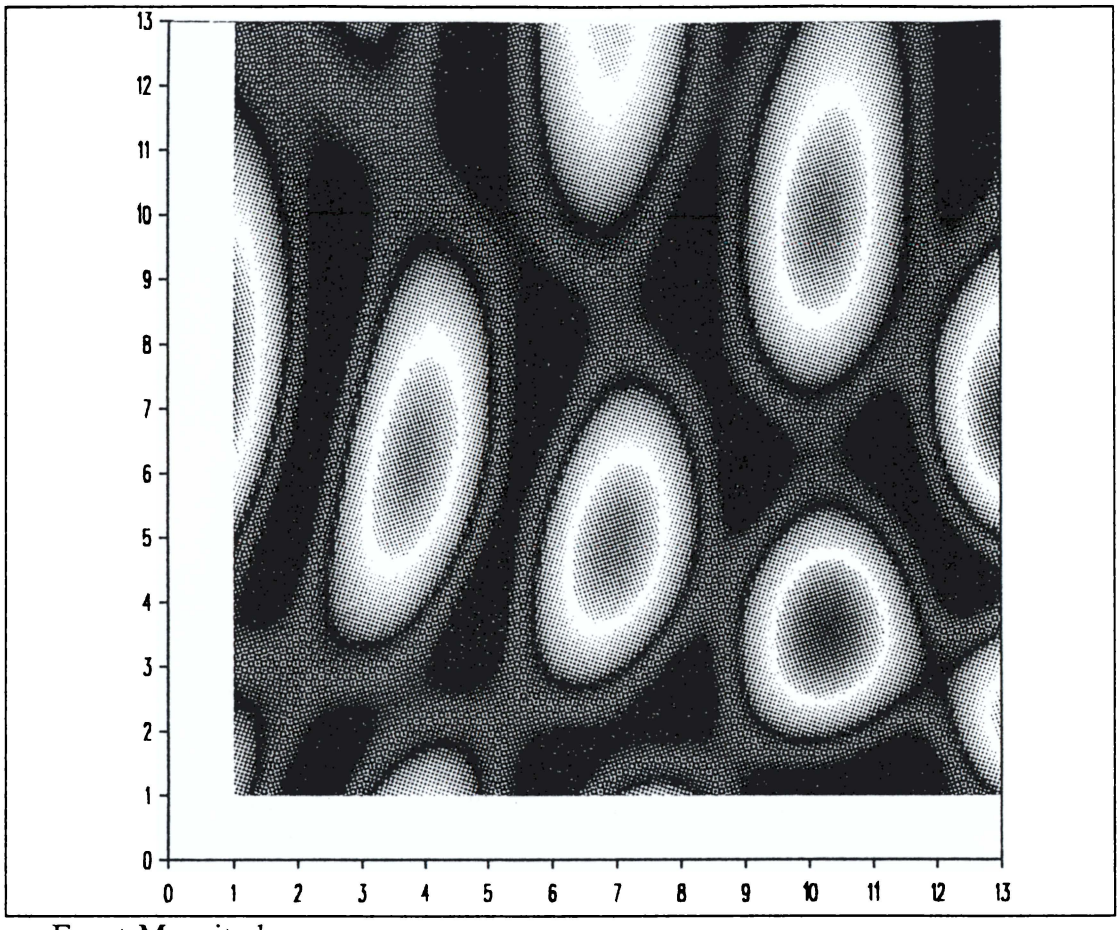

a. Exact Magnitude

Figure A2.5. Magnitude Plots for Case 2, $k_g = 1$

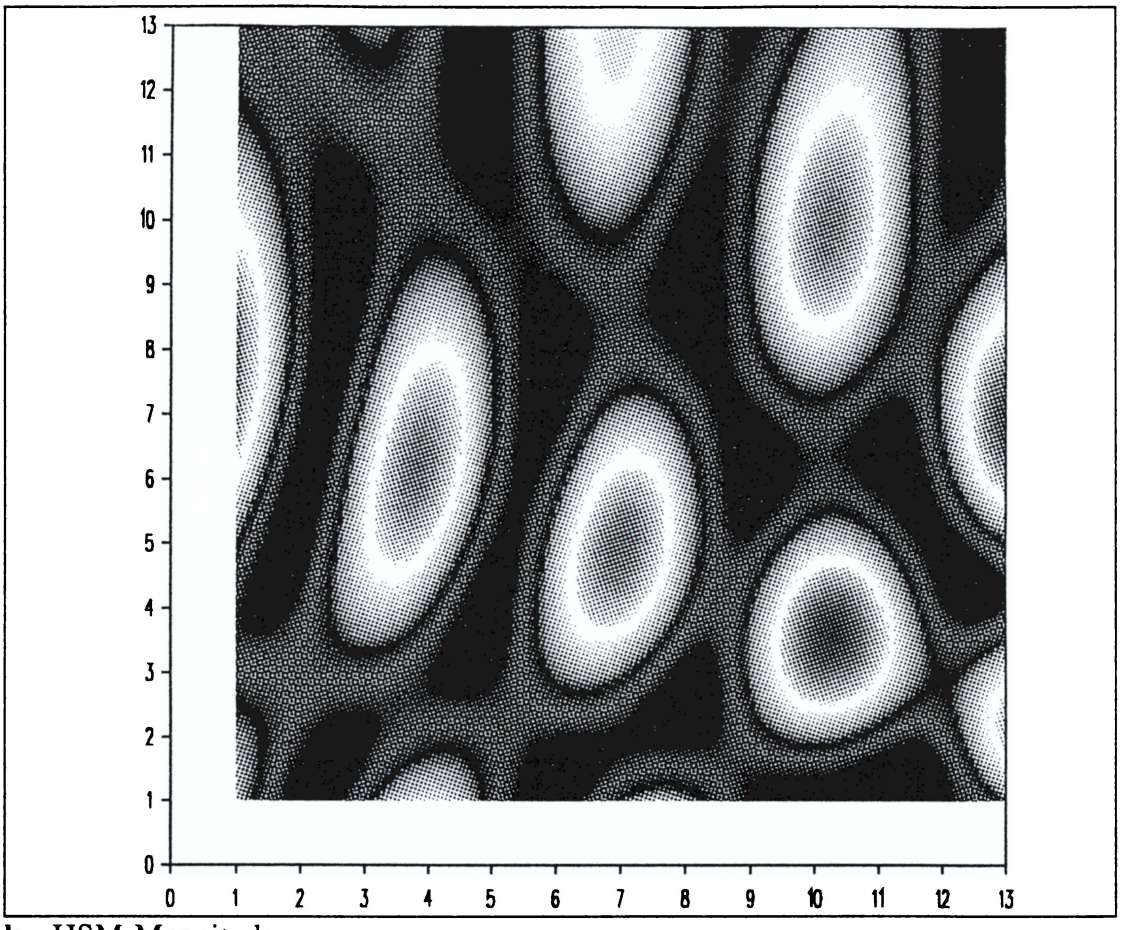

b. HSM Magnitude

Figure A2.5. (continued)

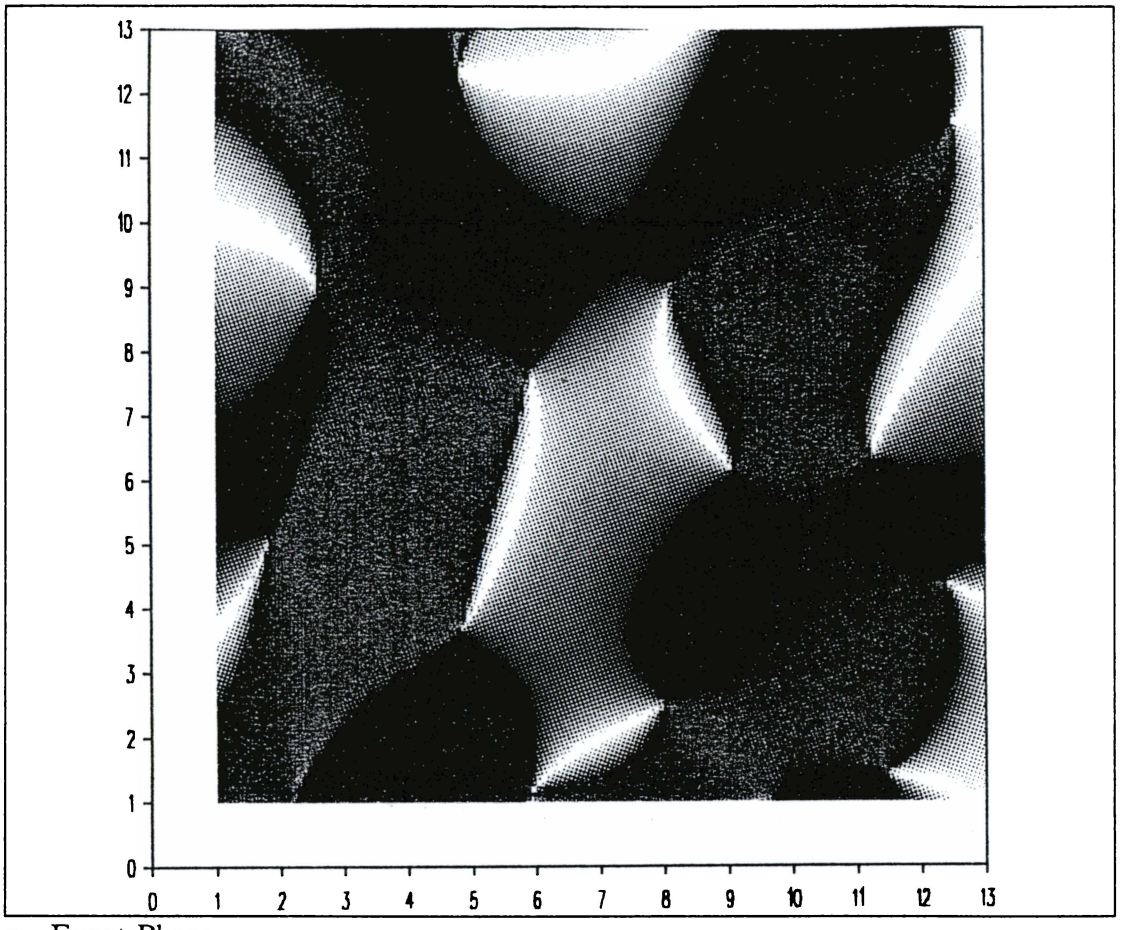

a. Exact Phase

Figure A2.6. Phase Plots for Case 2, k = 1

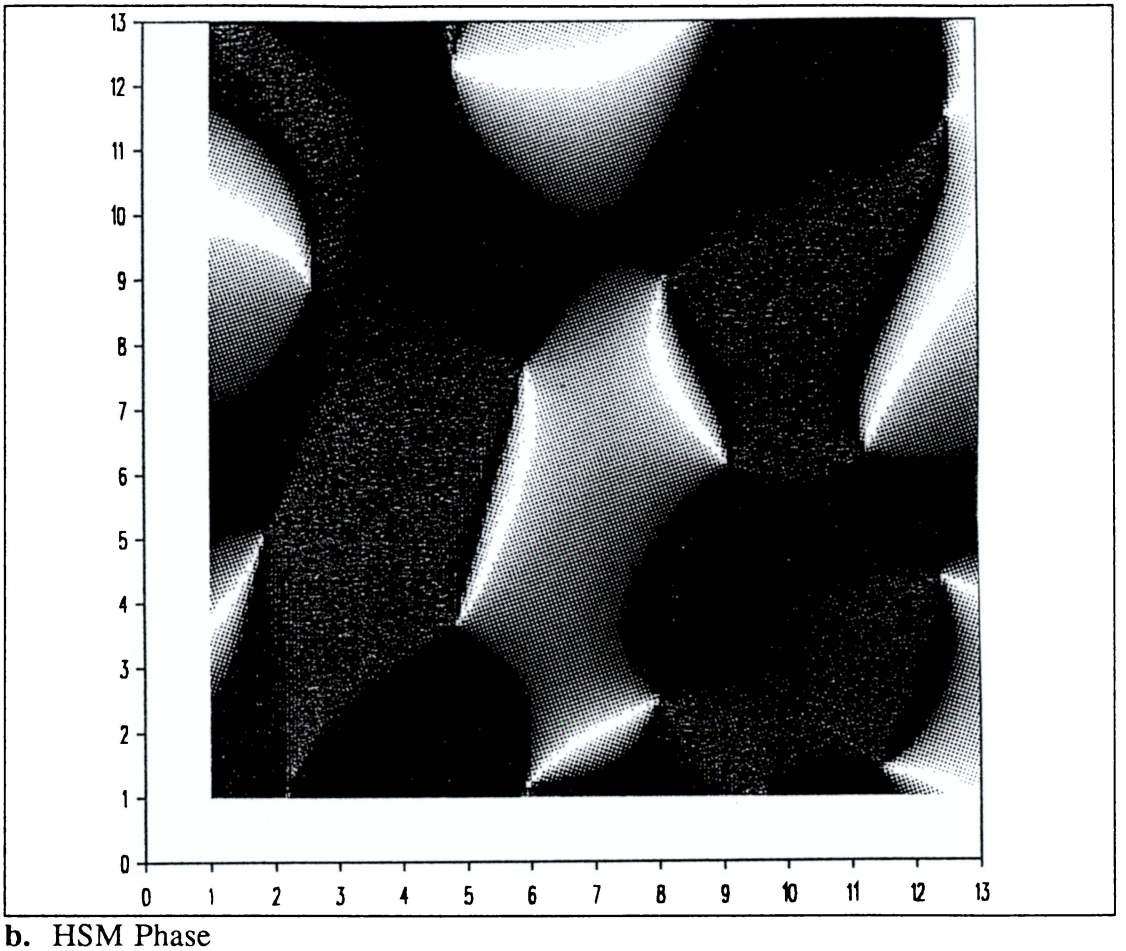

b. HSM Phase

Figure A2.6. (continued)

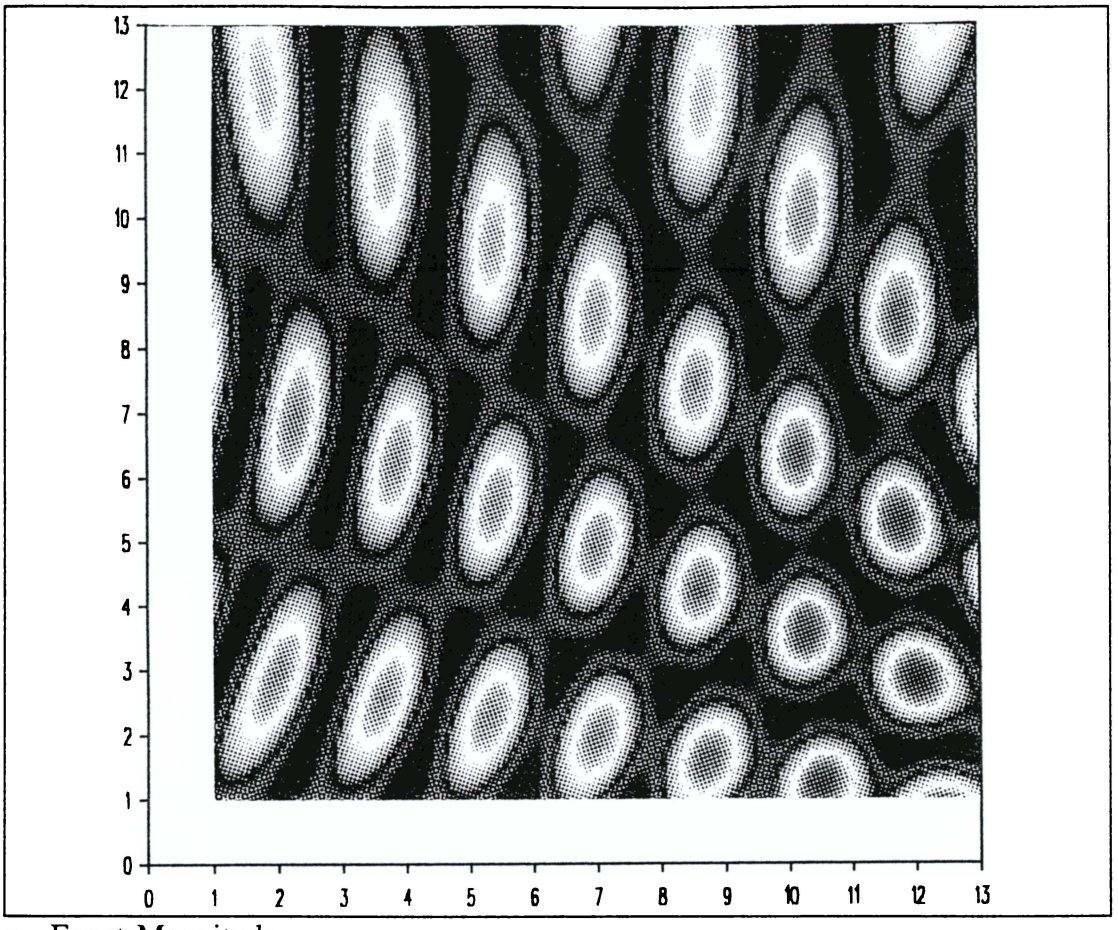

a. Exact Magnitude

Figure A2.7. Magnitude Plots for Case 2, k = 2

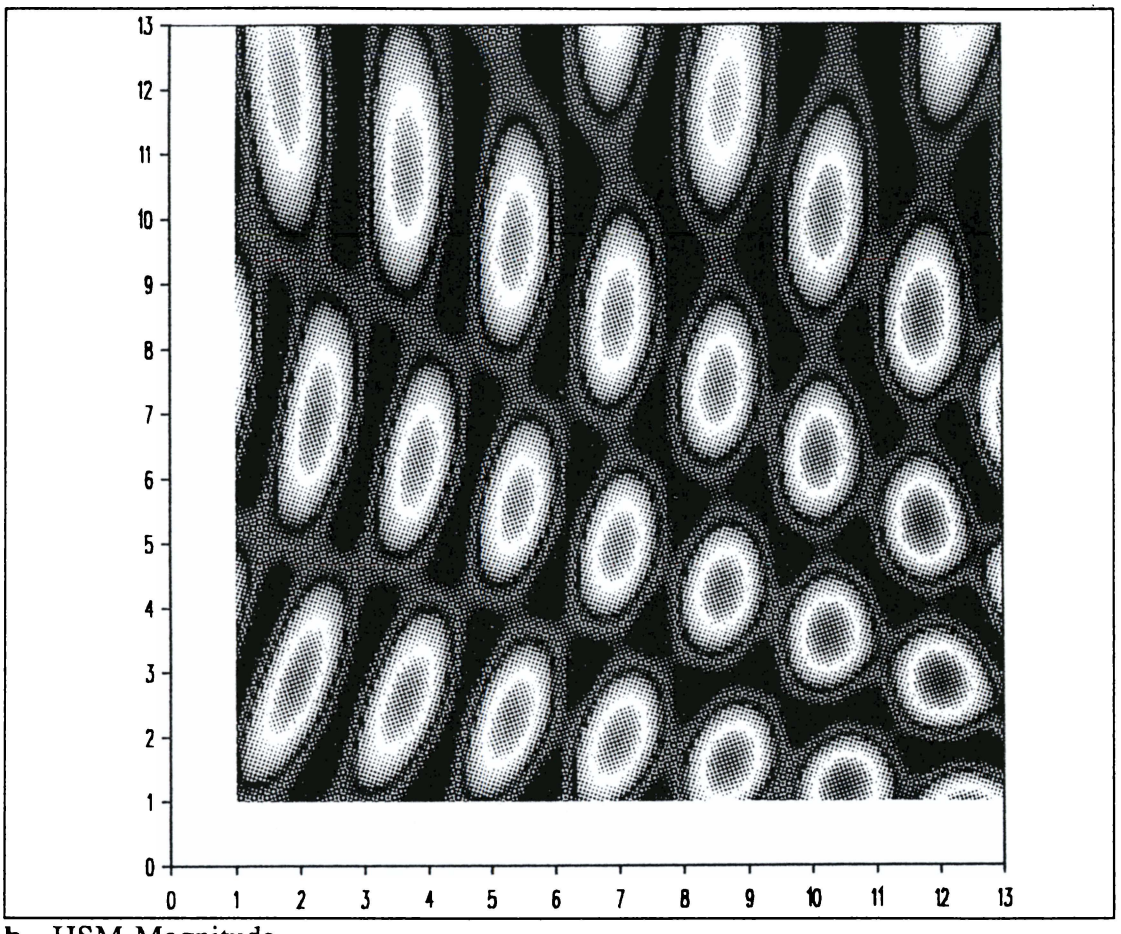

b. HSM Magnitude

Figure A2.7. (continued)

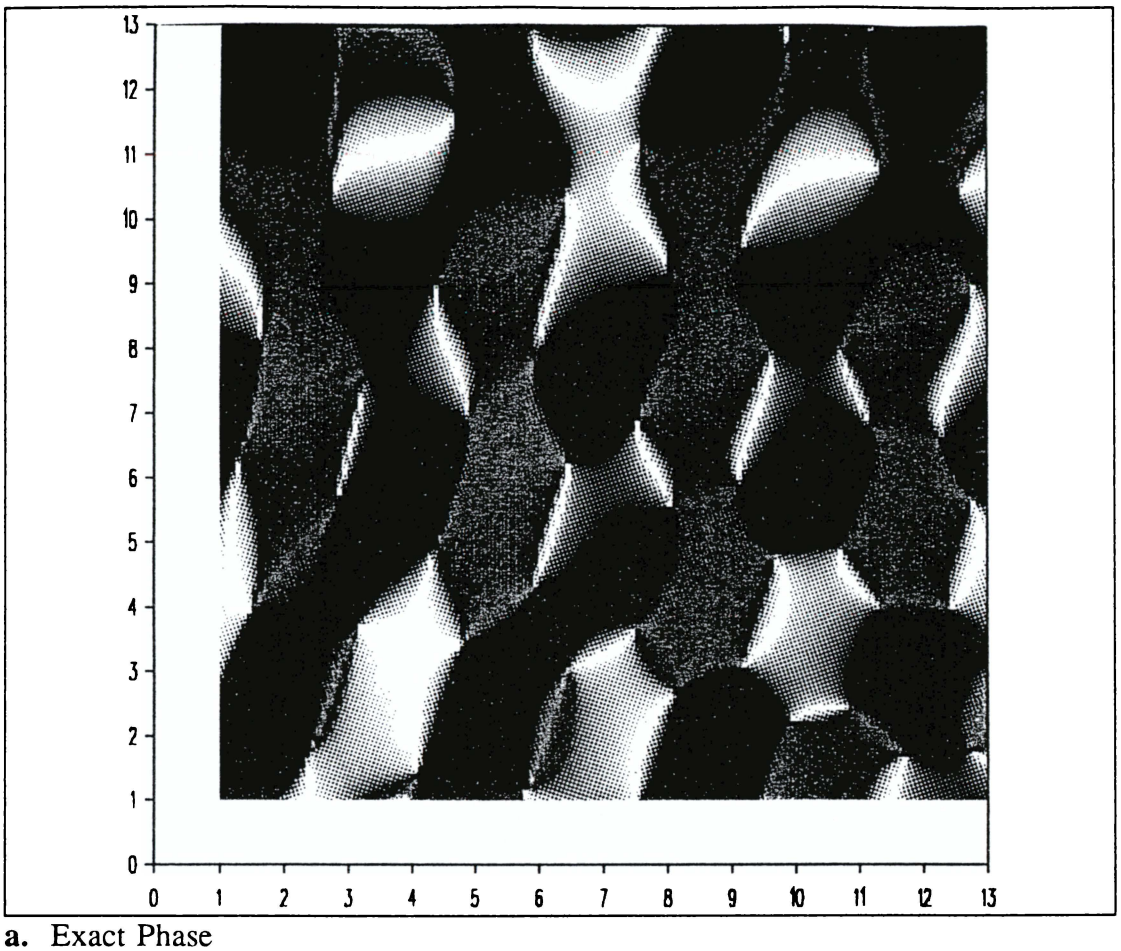

a. Exact Phase

Figure A2.8. Phase Plots for Case 2, k = 2

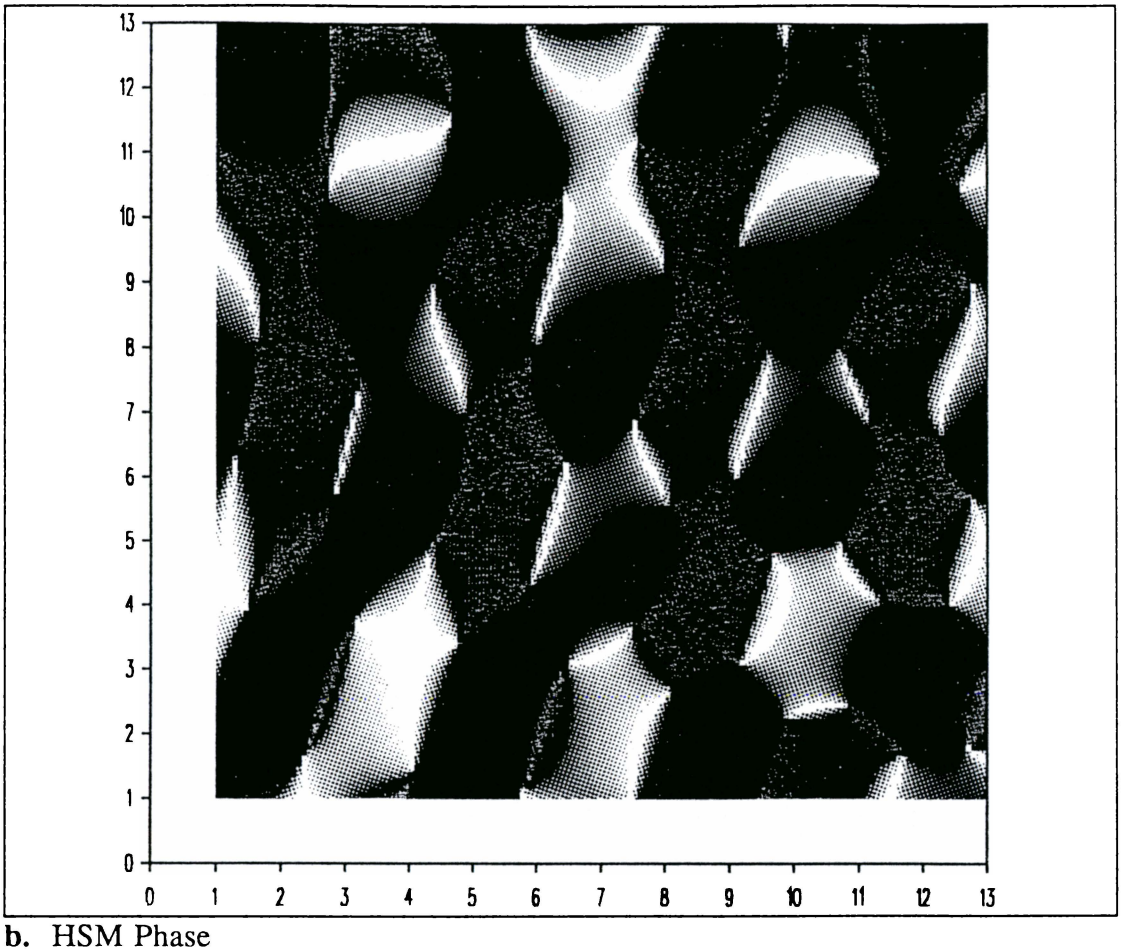

b. HSM Phase

Figure A2.8. (continued)

APPENDIX 3

FIVE AND NINE NODE FINITE DIFFERENCE SCHEMES

The five node scheme is derived from using central differencing with the Helmholtz equation:

$$\nabla^2\phi + k^2\phi = 0 \qquad \textbf{(A1.15)}$$

In two dimensions, this can be expressed as:

$$\frac{\partial^2\phi}{\partial x^2} + \frac{\partial^2\phi}{\partial y^2} + k^2\phi = 0 \qquad \textbf{(A1.16)}$$

Assuming a Cartesian coordinate system, the partial differential equations can be approximated by central differencing:

$$\frac{\phi_{i+1,j} - 2\phi_{i,j} + \phi_{i-1,j}}{(\Delta x)^2} + \frac{\phi_{i,j+1} - 2\phi_{i,j} + \phi_{i,j-1}}{(\Delta y)^2} + k^2\phi_{i,j} = 0 \qquad \textbf{(A1.17)}$$

Assuming $\Delta x = \Delta y$, this can be simplified to solve explicitly for $\phi_{i,j}$ (the five node equation):

$$\phi_{i-1j} - 2\phi_{ij} + \phi_{i+1j} + \phi_{ij+1} - 2\phi_{ij} + \phi_{ij-1} + (\Delta x)^2 k^2 \phi_{ij} = 0$$

$$4\phi_{ij} - (\Delta x)^2 k^2 \phi_{ij} = \phi_{i+1j} + \phi_{i-1j} + \phi_{ij+1} + \phi_{ij-1} \qquad \text{(A1.18)}$$

$$\phi_{ij} = \frac{1}{4 - (\Delta x)^2 k^2}\left(\phi_{i+1j} + \phi_{i-1j} + \phi_{ij+1} + \phi_{ij-1}\right)$$

The nine node equation is taken from [14, p. 122, eq. 4-114]. This equation was derived in [14] for a Laplacian differential equation, and according to the text, with $\Delta x = \Delta y$, it approximates the Laplacian operator to $O((\Delta x)^6)$. To modify the equation for the Helmholtz Equation, the two sets of central differences in the x and y directions need to be weighed. When [14] is examined, the central difference containing the computed node is weighed by multiplying it by 10/12, and the two central differences around it are each weighed by 1/12. Using these weights, the computed node can explicitly be solved for as follows:

$$\begin{aligned}
&\frac{1}{12}\left(\frac{\phi_{i+1j+1} - 2\phi_{ij+1} + \phi_{i-1j+1}}{(\Delta x)^2}\right) + \frac{5}{6}\left(\frac{\phi_{i+1j} - 2\phi_{ij} + \phi_{i-1j}}{(\Delta x)^2}\right) \\
&\quad + \frac{1}{12}\left(\frac{\phi_{i+1j-1} - 2\phi_{ij-1} + \phi_{i-1j-1}}{(\Delta x)^2}\right) \\
&+ \frac{1}{12}\left(\frac{\phi_{i+1j+1} - 2\phi_{i+1j} + \phi_{i+1j-1}}{(\Delta y)^2}\right) + \frac{5}{6}\left(\frac{\phi_{ij+1} - 2\phi_{ij} + \phi_{ij-1}}{(\Delta y)^2}\right) \\
&\quad + \frac{1}{12}\left(\frac{\phi_{i-1j+1} - 2\phi_{i-1j} + \phi_{i-1j-1}}{(\Delta y)^2}\right) \\
&\quad + k^2\phi_{ij} = 0
\end{aligned} \qquad \text{(A1.19)}$$

$$
\begin{aligned}
&(\phi_{i+1j+1} - 2\phi_{ij+1} + \phi_{i-1j+1}) + 10(\phi_{i+1j} - 2\phi_{ij} + \phi_{i-1j}) \\
&\quad + (\phi_{i+1j-1} - 2\phi_{ij-1} + \phi_{i-1j-1}) \\
&+ (\phi_{i+1j+1} - 2\phi_{i+1j} + \phi_{i+1j-1}) + 10(\phi_{ij+1} - 2\phi_{ij} + \phi_{ij-1}) \\
&\quad + (\phi_{i-1j+1} - 2\phi_{i-1j} + \phi_{i-1j-1}) \\
&\quad + 12(\Delta x)^2 k^2 \phi_{ij} = 0
\end{aligned}
\tag{A1.20}
$$

$$
\begin{aligned}
&(\phi_{i+1j+1} - 2\phi_{ij+1} + \phi_{i-1j+1}) + 10(\phi_{i+1j} + \phi_{i-1j}) + (\phi_{i+1j-1} - 2\phi_{ij-1} + \phi_{i-1j-1}) \\
&+ (\phi_{i+1j+1} - 2\phi_{i+1j} + \phi_{i+1j-1}) + 10(\phi_{ij+1} + \phi_{ij-1}) + (\phi_{i-1j+1} - 2\phi_{i-1j} + \phi_{i-1j-1}) \\
&\quad = (40 - 12(\Delta x)^2 k^2)\phi_{ij} = 0
\end{aligned}
\tag{A1.21}
$$

$$
\begin{aligned}
&2(\phi_{i+1j+1} + \phi_{i-1j+1} + \phi_{i+1j-1} + \phi_{i-1j-1}) \\
&\quad + 8(\phi_{ij+1} + \phi_{i+1j} + \phi_{ij-1} + \phi_{i-1j}) \\
&\quad = (40 - 12(\Delta x)^2 k^2)\phi_{ij}
\end{aligned}
\tag{A1.22}
$$

$$
\begin{aligned}
\phi_{ij} = \frac{1}{20 - 6(\Delta x)^2 k^2} \Big(&\phi_{i+1j+1} + \phi_{i-1j+1} + \phi_{i+1j-1} + \phi_{i-1j-1} \\
&+ 4(\phi_{ij+1} + \phi_{i+1j} + \phi_{ij-1} + \phi_{i-1j}) \Big)
\end{aligned}
\tag{A1.23}
$$

For unequal grid spacing, a similar equation can be constructed, but the error increases to $O((\Delta x)^4, (\Delta y)^4)$ for the Laplacian portion.

APPENDIX 4

HYPOTHETICAL SOURCE STRENGTHS FOR DIFFERENT NUMBERS OF LOCAL NODES

Lobe variations for the standard stencil in section 3.2.2 provided the inspiration to try other n-gons to see how their lobes changed. The number of lobes occurring when the plane wave travels along an axis proves to be the same as the number of local nodes, and the number of lobes that appear when the angle approaches along a bisector between two outside nodes is two less than the number of local nodes (figs. A4.1-8, for bisectors see section 3.3.2, fig. 3.3.2.1b). If an odd number of nodes is used, the number of lobes is always one less than the number of local nodes, independent of the incoming angle (see fig. A4.2, A4.4, and A4.7). Actually, the number of lobes is related to the number of singular values used instead of the number of nodes, and the previous statements concerning the number of local nodes are true for the number of singular values. However, usually all of the singular values are used.

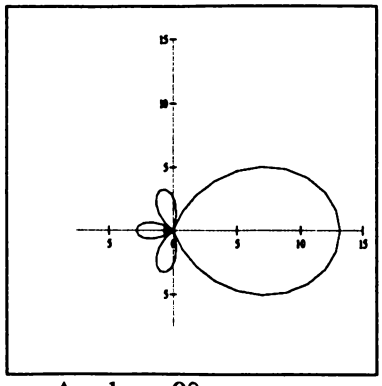

a. Angle = 0°

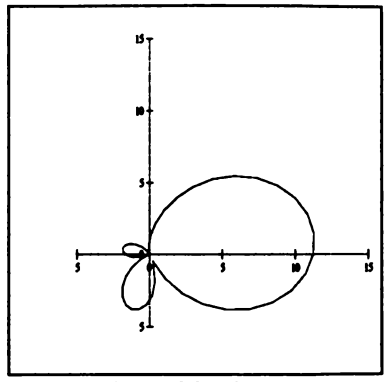

b. Angle = 22.5°

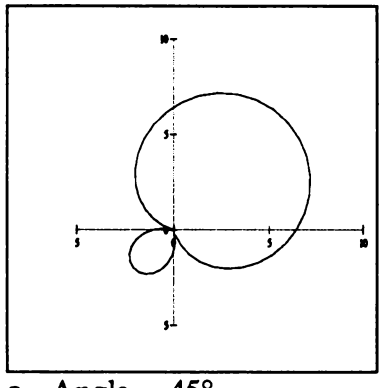

c. Angle = 45°

Figure A4.1. Hypothetical source strength distributions for plane waves that approach from different angles; 4 circularly distributed local nodes with k = 1.0

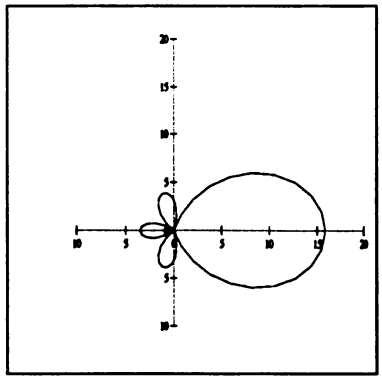

a. Angle = 0°

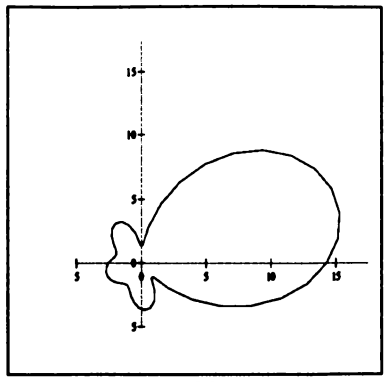

b. Angle = 18°

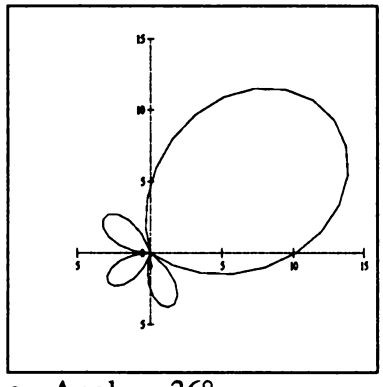

c. Angle = 36°

Figure A4.2. Hypothetical source strength distributions for plane waves that approach from different angles; 5 circularly distributed local nodes with k = 1.0

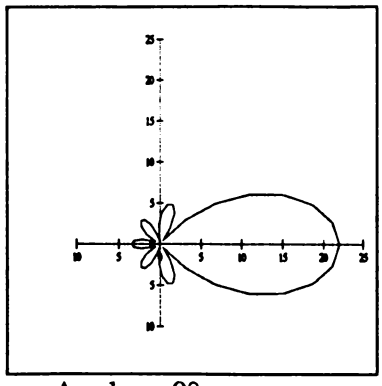

a. Angle = 0°

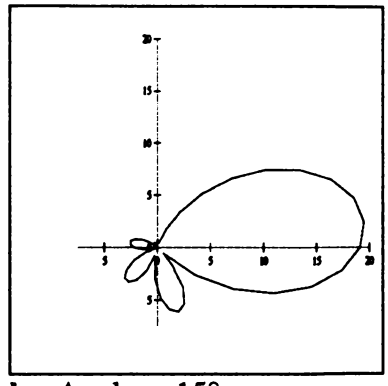

b. Angle = 15°

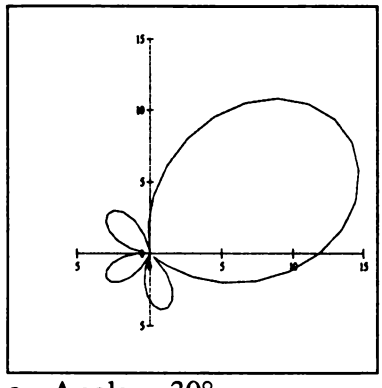

c. Angle = 30°

Figure A4.3. Hypothetical source strength distributions for plane waves that approach from different angles; 6 circularly distributed local nodes with k = 1.0

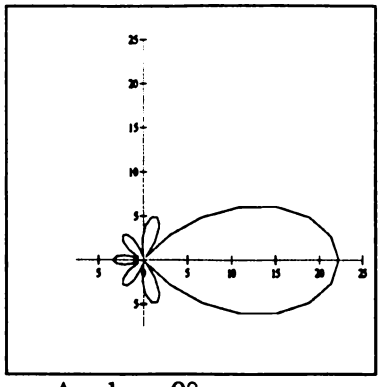

a. Angle = 0°

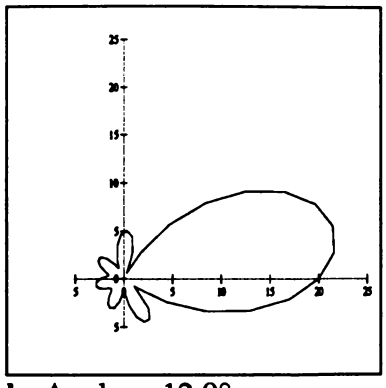

b. Angle = 12.9°

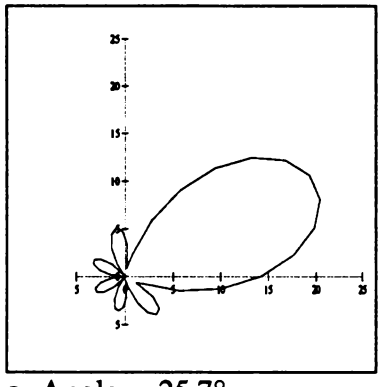

c. Angle = 25.7°

Figure A4.4. Hypothetical source strength distributions for plane waves that approach from different angles; 7 circularly distributed local nodes with k = 1.0

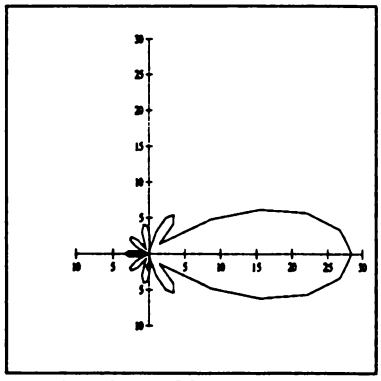

a. Angle = 0°

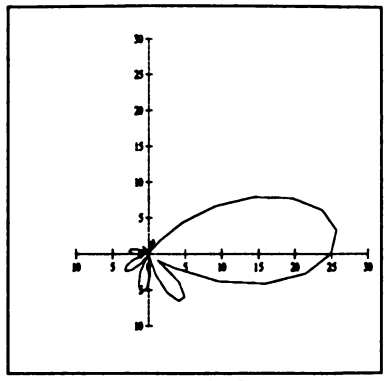

b. Angle = 11.25°

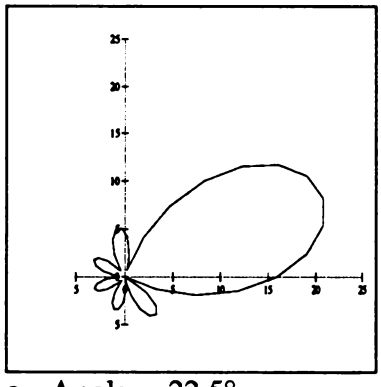

c. Angle = 22.5°

Figure A4.5. Hypothetical source strength distributions for plane waves that approach from different angles; 8 circularly distributed local nodes with k = 1.0

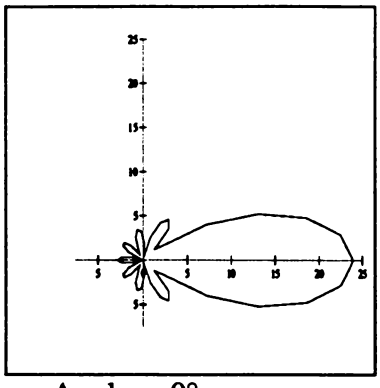

a. Angle = 0°

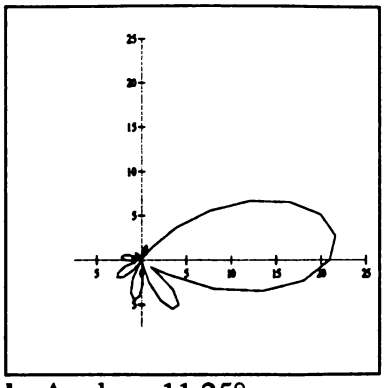

b. Angle = 11.25°

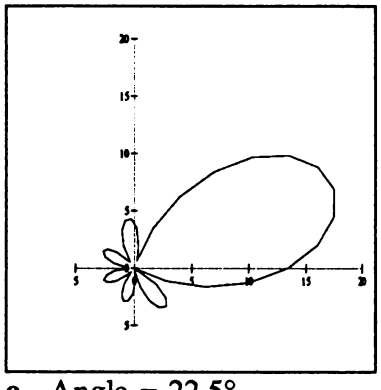

c. Angle = 22.5°

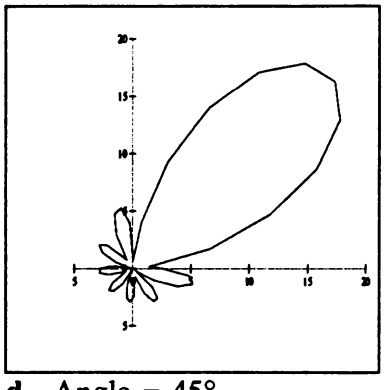

d. Angle = 45°

Figure A4.6. Hypothetical source strength distributions for plane waves that approach from different angles; 8 local nodes distributed in a box with k = 1.0

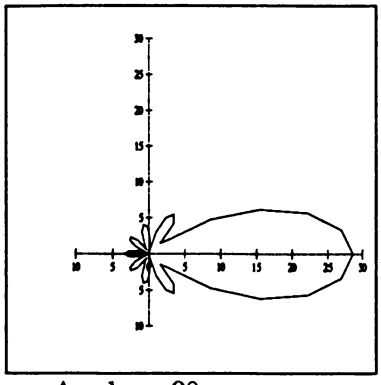

a. Angle = 0°

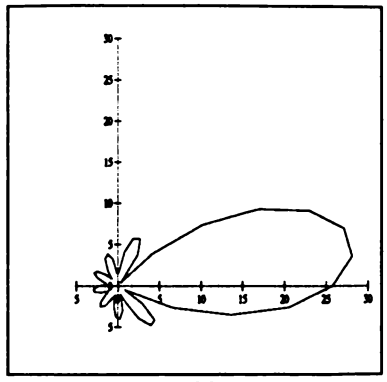

b. Angle = 10°

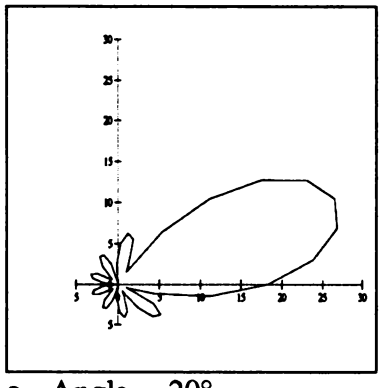

c. Angle = 20°

Figure A4.7. Hypothetical source strength distributions for plane waves that approach from different angles; 9 circularly distributed local nodes with k = 1.0

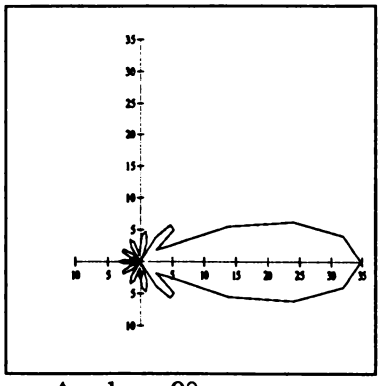

a. Angle = 0°

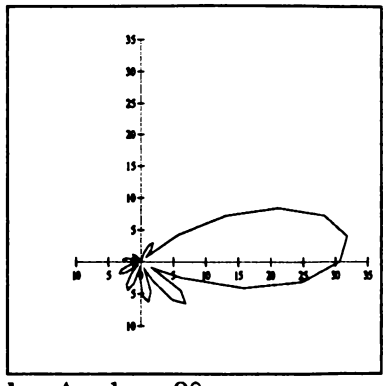

b. Angle = 9°

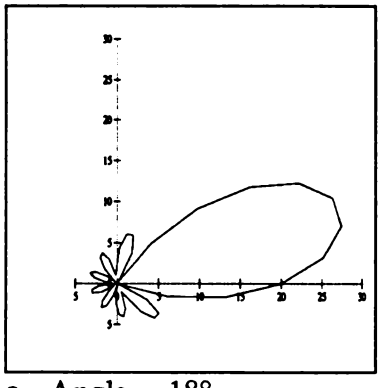

c. Angle = 18°

Figure A4.8. Hypothetical source strength distributions for plane waves that approach from different angles; 10 circularly distributed local nodes with k = 1.0

APPENDIX 5

COMPARISON OF WEIGHTING FACTORS BETWEEN THE HSM AND THE NINE NODE FD SCHEME

In general, discretization schemes weight nearby nodes to determine the value of a particular node. For a Cartesian mesh and a still medium, the 8 local nodes should be symmetrically weighted about the computed node. Taking advantage of this symmetry, there are only two different weights for the eight nodes: one weight for the nodes closest to the computed node, and the other weight for the nodes furthest. The nearer nodes weights will be referred to as side weights, and the furthest node weights will be referred to as diagonal weights.

The HSM yields similar weighting values to nearby nodes as the 9 node FD scheme for low values of reduced frequency (see table A5.1). As k_g approaches 2, however, the weighing values lose their similarity. It is interesting to note that when the difference between the side weights is correlated with the average errors for the large test grid (fig. 3.6.2.1), the difference appears to correspond to the error of the nine point scheme.

Table A5.I. Weights of HSM and 9 Node FD Scheme for Different Values of k_g

	k	Side Weight	Diagonal Weight
HSM	0.25	0.2036754361	0.0510783542
9 Node FD		0.2038216561	0.0509554140
HSM	0.5	0.2153399012	0.0545142773
9 Node FD		0.2162162162	0.0540540541
HSM	0.75	0.2371867106	0.0610002851
9 Node FD		0.2406015038	0.0601503759
HSM	1.0	0.2740500744	0.0720712864
9 Node FD		0.2857142857	0.0714285714
HSM	1.25	0.3364617363	0.0910943716
9fd		0.3764705882	0.0941176471
HSM	1.5	0.4502879400	0.1263965548
9 Node FD		0.6153846154	0.1538461538
HSM	1.75	0.6972899489	0.2044501263
9 Node FD		2.4615384615	0.6153846154
HSM	2.	1.5317466103	0.4728827940
9 Node FD		-1.0000000000	-0.2500000000

VITA

Jonathan Charles French was born in Buffalo, New York on May 22, 1969. He graduated from Windsor High School in Windsor, Connecticut in May, 1987. The following September he entered Worcester Polytechnic Institute and in May, 1991, received the degree of Bachelor of Science in Mechanical Engineering. In September, 1991, he entered The University of Tennessee Space Institute, Tullahoma and in December, 1993, received a Master of Science degree in Mechanical Engineering.

He is presently employed as a Graduate Research Assistant at The University of Tennessee Space Institute, and is pursuing a doctorate in Engineering Science and Mechanics.